Tailoring Plasmon-Enhanced Light-Matter Interaction

Im Fachbereich Physik der
Freien Universität Berlin
eingereichte

Dissertation

zur Erlangung des Grades eines Doktors der
Naturwissenschaften (Dr. rer. nat.)

von

Sven Niclas Tebogo Müller

Berlin, im August 2019

1. Gutachter: Prof. Dr. Stephanie Reich
2. Gutachter: Prof. Dr. Joachim Heberle

Tag der Einreichung: 09. August 2019
Tag der Disputation: 14. Mai 2020

Dedicated to my wife Feiyan and my lovely kids Simon Zhilin and Jonathan Zhishan.

Abstract

Plasmons are the collective oscillation of free electrons in materials. They concentrate light into nanoscale volumes and trigger optical processes in nearby materials. My thesis is devoted to the understanding of optical processes that are mediated by localized surface plasmons. The fundamental excitation of plasmonic modes and the enhancement of optical absorption and Raman scattering in nanoscale materials are studied using experimental and theoretical approaches.

I introduce a novel type of plasmonic excitation in layered films of metallic nanoparticles. Because of field retardation, incident light induces antiparallel dipoles in adjacent layers of metallic nanoparticles exciting a dark interlayer plasmon. It benefits from reduced radiative damping and efficient light absorption as I demonstrate with simulations and experiments. The self-assembled nanoparticle films pave the way for large-area coatings with tunable plasmon resonances. An application is the decay of plasmons into hot charge carriers that trigger photocatalytic reactions in molecules. I propose dark interlayer plasmons as ideal excitation channels for hot electrons because of their small radiative damping.

Using plasmonic nanostructures for photodetection and sensing requires an understanding of the interaction with adjacent materials. I introduce microscopic theories for the enhancement of optical absorption and Raman scattering by localized surface plasmons. The plasmonic near field of nanoparticle arrays induced non-vertical optical transitions in graphene in dependence of the periodicity of the plasmonic lattice. For plasmon-enhanced Raman scattering I developed a general theoretical framework using perturbation theory. It provides analytic expressions for the enhanced Raman cross section. In a molecular dipole coupled to a plasmonic nanoparticle the enhancement is strongly affected by interference between different scattering channels.

Plasmon-enhanced Raman scattering is an ideal tool to study the properties of materials interfaced with plasmonic nanostructures. I analyzed nanoscale strain and doping in graphene on top of a gold nanostructure. I developed a method for separating the contributions from strain and doping in the Raman spectrum of graphene, which is applicable to graphene on arbitrary substrates and in arbitrary strain configurations.

List of publications

1. Bruno G. M. Vieira*, Niclas S. Mueller*, Eduardo Bedê Barros, and Stephanie Reich **Plasmonic Properties of Close-Packed Metallic Nanoparticle Mono- and Bilayers** The Journal of Physical Chemistry C 123, 17951-17960 (2019)

2. Niclas S. Mueller and Stephanie Reich **Modeling Surface-Enhanced Spectroscopy with Perturbation Theory** Frontiers in Chemistry 7, 470 (2019)

3. Sören Wasserroth, Sebastian Heeg, Niclas S. Mueller, Patryk Kusch, Uwe Hübner, Etienne Gaufrès, Nathalie Y.-W. Tang, Richard Martel, Aravind Vijayaraghavan, and Stephanie Reich **Resonant, Plasmonic Raman Enhancement of α-6T Molecules Encapsulated in Carbon Nanotubes** The Journal of Physical Chemistry C 123, 10578-10585 (2019)

4. Niclas S. Mueller, Bruno G. M. Vieira, Dominik Höing, Florian Schulz, Eduardo B. Barros, Holger Lange, and Stephanie Reich **Direct optical excitation of dark plasmons for hot electron generation** Faraday discussions 214, 159-173 (2019)

5. Niclas S. Mueller, Sabrina Juergensen, Katja Höflich, Stephanie Reich, and Patryk Kusch **Excitation-Tunable Tip-Enhanced Raman Spectroscopy** The Journal of Physical Chemistry C 122, 28273-28279 (2018)

6. Niclas S. Mueller*, Bruno G. M. Vieira*, Florian Schulz, Patryk Kusch, Valerio Oddone, Eduardo B. Barros, Holger Lange, and Stephanie Reich **Dark Interlayer Plasmons in Colloidal Gold Nanoparticle Bi- and Few-Layers** ACS Photonics 5, 3962-3969 (2018)

7. Patryk Kusch, Nieves M. Azpiazu, Niclas S. Mueller, Stefan Mastel, Jose Ignacio Pascual, and Rainer Hillenbrand **Combined Tip-Enhanced Raman Spectroscopy and Scattering-Type Scanning Near-Field Optical Microscopy** The Journal of Physical Chemistry C 122, 16274-16280 (2018)

8. Sören Wasserroth, Timo Bisswanger, Niclas S. Mueller, Patryk Kusch, Sebastian Heeg, Nick Clark, Fredrik Schedin, Roman Gorbachev, and Stephanie Reich **Gra-**

phene as a local probe to investigate near-field properties of plasmonic nanostructures Physical Review B 97, 155417 (2018)

9. Niclas S. Mueller and Stephanie Reich **Microscopic theory of optical absorption in graphene enhanced by lattices of plasmonic nanoparticles** Physical Review B 97, 235417 (2018)

10. Niclas S. Mueller, Sebastian Heeg, Miriam Peña Alvarez, Patryk Kusch, Sören Wasserroth, Nick Clark, Fredrik Schedin, John Parthenios, Konstantinos Papagelis, Costas Galiotis, Martin Kalbáč, Aravind Vijayaraghavan, Uwe Huebner, Roman Gorbachev, Otakar Frank, and Stephanie Reich **Evaluating arbitrary strain configurations and doping in graphene with Raman spectroscopy** 2D Materials 5, 015016 (2018)

11. Ado Jorio, Niclas S. Mueller, and Stephanie Reich **Symmetry-derived selection rules for plasmon-enhanced Raman scattering** Physical Review B 95, 155409 (2017)

12. Patryk Kusch, Stefan Mastel, Niclas S. Mueller, Nieves Morquillas Azpiazu, Sebastian Heeg, Roman Gorbachev, Fredrik Schedin, Uwe Hübner, Jose I. Pascual, Stephanie Reich, and Rainer Hillenbrand **Dual-scattering near-field microscope for correlative nanoimaging of SERS and electromagnetic hotspots** Nano Letters 17, 2667-2673 (2017)

13. Niclas S. Mueller*, Sebastian Heeg*, Patryk Kusch, Etienne Gaufrès, Nathalie Y-W Tang, Uwe Hübner, Richard Martel, Aravind Vijayaraghavan, and Stephanie Reich **Plasmonic enhancement of SERS measured on molecules in carbon nanotubes** Faraday discussions 205, 85-103 (2017)

14. Niclas S. Mueller, Sebastian Heeg, and Stephanie Reich **Surface-enhanced Raman scattering as a higher-order Raman process** Physical Review A 94, 023813 (2016)

Authors marked with * contributed equally to this work.

Contents

1 | Motivation

The ability to manipulate light on length scales smaller than the diffraction limit is at the heart of nano-optics.[1,2] The devices we use in our daily lives, such as computers and smartphones, are operated by circuits that switch electric currents. The architecture of integrated circuits is about to approach the limit of miniaturization, which results from a trade off between heat dissipation, switching speed and quantum size effects.[3] Nanophotonic circuits are a promising alternative as photons move data much faster than electrons.[2] The realization of all-optical computers will depend critically on finding nanophotonic components that switch and store light on the nanoscale. Transitioning to this technology requires opto-electronic components that turn light into electrical currents and vice versa.[4] The implementation on computer chips requires an efficient interfacing of nanophotonic components with other materials, such as nanoscale electric conductors.

A promising route to tackle these challenges are localized surface plasmons, which are a collective oscillation of electrons in metallic nanostructures.[5] Plasmonic nanoparticles are efficient light extractors, having optical absorption and scattering cross sections that are a multiple of their cross-sectional area.[6] This offers a route to store electromagnetic energy on the nanoscale.[7] A second key property of plasmons is the ability to concentrate light into nanoscale volumes.[8,9] The collective oscillation of charges leads to intense electromagnetic fields close to the metal surface.[6,10] Metallic nanoparticles that are arranged into chains and lattices interact via these optical near fields which enables nanoscale waveguiding.[10,11] The electric field intensity in the nanoscale gaps between plasmonic nanoparticles can be five orders of magnitude larger than that of the incident light.[6] Such electromagnetic field hot spots are ideal for driving optical processes in nearby nanomaterials and molecules, paving the way for optoelectronic components and sensors on the nanoscale.[6,8,12]

A bottleneck for many applications is that plasmons are extremely lossy excitations.[5,13] On a time scale of a few femto seconds, plasmons convert into photons via radiative decay, and into uncorrelated electron-hole pairs in the metal via internal losses.[14] It is thus

highly desirable to find ways to tailor these decay channels. A promising candidate are dark plasmons that have a vanishing net dipole moment, which leads to a suppression of radiative losses.[15–17] Being dipole inactive implies on the other hand an inefficient coupling to far field radiation. Excitation schemes are needed to use dark plasmons for applications like waveguiding and energy storage on the nanoscale.[11,18,19] This thesis introduces a new type of dark plasmon that can be directly excited by a plane electromagnetic wave, making use of field retardation (see Publication P1 of my thesis).

Another challenge is to understand the interaction of plasmonic nanostructures with other materials, which occurs in various ways. The decay of plasmons via internal losses results in highly excited electrons or holes at the metal surface, called hot charge carriers.[20] These charges transfer into materials and molecules that are in direct contact with the metal surface, which leads to doping or even chemical reactions.[21,22] The ability to trigger photocatalytic reactions via hot electrons has attracted a lot of attention in the plasmonics community because it is a direct application of plasmonic losses, which are detrimental in most other cases.[23] In this thesis I suggested dark plasmons as an ideal excitation channel of hot electrons (see Publication P2 of my thesis).

A second coupling mechanism is the excitation of electron-hole pairs in a nearby material via the electromagnetic near field of the plasmon.[7] In a simple picture, the plasmonic nanostructure serves as an optical antenna that strongly increases the local light intensity.[1,6] This is ideal for enhancing the photocurrent in nanoscale optoelectronic devices, such as photodetectors.[8,12,24] Theoretical modeling of this process is challenging because of the interplay of various absorption pathways, as well as additional contributions to the photocurrent from charge transfer and thermoelectric effects.[25–28] We interfaced the two-dimensional carbon allotrope graphene with plasmonic nanostructures to study these effects[29] (see Publications P3 and P5 of my thesis). While the local charge doping by a plasmonic nanostructure was assessed experimentally via the Raman spectrum of graphene (see Publication P5 of my thesis), I studied the excitation of electron-hole pairs via the plasmonic near field with a microscopic theory (see Publication P3 of my thesis).

A major application of plasmons is the enhancement of Raman scattering in nearby molecules and nanomaterials, which is known as surface-enhaced Raman scattering (SERS).[6,30,31] Compared to plasmon-enhanced optical absorption, both the incoming- and the Raman-scattered light are enhanced by the localized surface plasmon.[6,32] This leads to an enhancement that scales with the fourth power of the local electric field amplitude. The SERS enhancement factors can reach ten orders of magnitude, which enables the detection of single molecules.[33,34] A major challenge is the design of SERS substrates that

provide reproducible enhancement and can be used for quantitative measurements.[6,35,36] This requires a detailed understanding of the underlying enhancement mechanisms. This thesis introduces a microscopic theory for the plasmonic enhancement mechanism of SERS that provides insight into the different scattering channels (see Publication P4 of my thesis). As the Raman spectrum gives direct information about the properties of a material, SERS is an ideal tool for studying the interface of nanoscale materials with plasmonic nanostructures.[31,37] I used SERS to analyze the nanoscale strain and doping in graphene on top of gold nanodimers (see Publication P5 of my thesis).

2 | Introduction

2.1. Plasmonics

Plasmonics is a vibrant field of nanooptics that is concerned with the interaction of light and the motion of charges in nanoscale materials.[5] The term "plasmon" refers to a collective oscillation of charges that can be excited in metallic nanostructures,[10] at metal surfaces,[38] in semiconductor nanoparticles,[39] in two-dimensional materials like graphene[40,41] and even in molecules.[42,43] In this thesis, I worked with localized surface plasmons in gold nanostructures. This type of plasmon may be directly and efficiently excited by light and offers the possibility to focus light into nanoscale volumes.[8,9] The local electric field intensity in nanometer gaps between plasmonic nanoparticles is up to 10^5 times higher than the incident light field and drives optical processes in nearby materials.[6] This gives rise to numerous applications in fields like analytical chemistry,[6,44,45] sensing,[46] waveguiding,[47] nanolasing,[48] solar energy conversion[7] and photochemistry.[22] In the following I will introduce the basic concepts underlying plasmonic excitations in metallic nanostructures.

2.1.1. Localized surface plasmon

A localized surface plasmon (LSP) is a collective oscillation of charges in a conductive nanostructure that has dimensions much smaller than the wavelength of light.[5,49] The basic concepts are introduced by considering the optical properties of a single metallic nanoparticle (Fig. 2.1). When the nanoparticle is illuminated with light, the electric field induces a collective oscillation of the conduction electrons inside the nanoparticle (Fig. 2.1a). Because of its small lateral dimension, the charges pile up at the boundaries of the nanoparticle leading to an intense electric field around the nanoparticle. The internal electric field leads to a restoring force acting on the driven charges and a resonance may occur, which is known as a localized surface plasmon resonance (LSPR). The plasmon

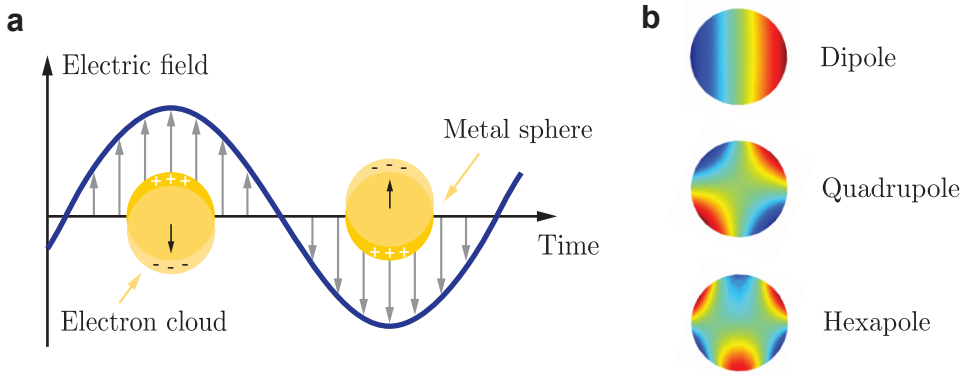

Figure 2.1. Localized surface plasmon resonance (LSPR). (a) Scheme of the excitation of an LSPR in a gold nanoparticle. An external light field drives the free electrons inside the nanoparticle into a collective oscillation. (b) Plasmonic eigenmodes of a nanosphere, which are of dipolar, quadrupolar or higher-order character. The figure shows the surface charges (red - positive, blue - negative) simulated with the eigenmode solver of the boundary-elements software package MNPBEM.[52]

resonances of a nanoparticle are understood as its electromagnetic eigenmodes, which are of dipolar, quadrupolar or higher-order character (Fig. 2.3b).[50,51]

When a plasmon mode has a finite net dipole moment it can be directly excited by light. This makes LSPs fundamentally different from propagating surface plasmons at metal surfaces or in two-dimensional materials where phase matching is needed for optical excitation.[38,40,41] The excitation of an LSPR leads to a resonant enhancement of light absorption and scattering by the nanoparticle (Fig. 2.2a).[53] The bright color of plasmonic nanoparticles in reflection and transmission has been used for hundreds of years for staining church windows and medieval handcraft.[5] Figure 2.2b shows simulated absorption coefficients, i.e., the ratio of the optical absorption cross section and the cross-sectional area, for gold and silver nanoparticles. The absorption coefficients can easily exceed an order of magnitude which demonstrates the strong interaction of light with LSPRs.[6]

The energy of the plasmon resonances depends on several parameters which enables a tunability across the entire visible spectrum. First of all, the frequency dependent dielectric function of the metal determines the spectral range in which an LSPR occurs.[5,6] For Au, Ag, Al and Cu nanoparticles the plasmonic resonances are excited with visible light.[6,54] The plasmon resonance of the Au nanosphere in Fig. 2.2b is redshifted from that of Ag because of interband transitions.[5] These lead in the case of Au to a step-like increase of the absorption coefficient for excitation energies larger than 2 eV and a damping of the plasmon resonance.[55] A second parameter that controls the LSPR is the nanoparticle

geometry.[56] The plasmon resonance shifts when changing the shape of the nanoparticle, as can be seen from a comparison of the LSPRs of an Au nanorod and an Au nanosphere in Fig. 2.2b. The shift is explained by a depolarization effect inside the nanoparticle that depends on its shape.[13,56] The nanoparticle size has only a minor effect on the energy of the plasmon resonance. Finally, the scattering and absorption peaks of a plasmonic nanoparticle are sensitive to the local environment and shift upon a change in the refractive index of the surrounding medium.[5,6] This offers a route to detect molecular interactions close to the nanoparticle surface and is the basis for plasmonic sensors.[46,57]

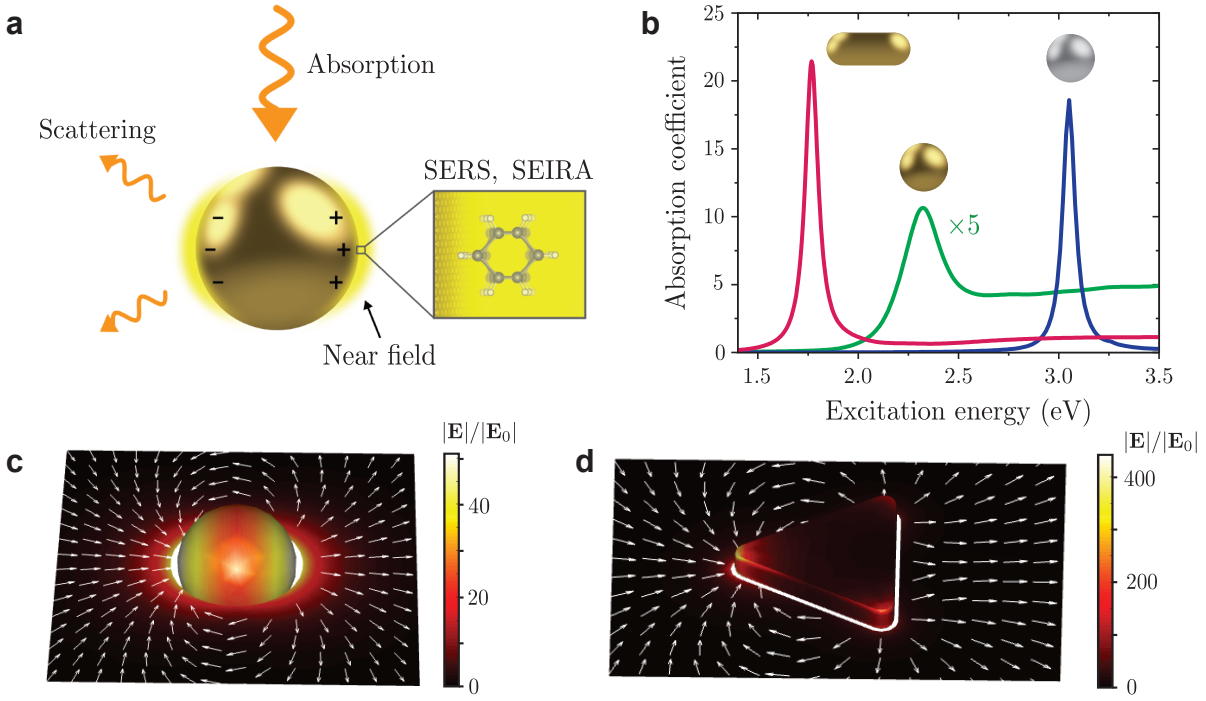

Figure 2.2. Properties of a localized surface plasmon resonance. (a) Sketch of the basic properties of an LSPR in a gold nanoparticle, including the resonant enhancement of light absorption and scattering and an intense near field close to the particle surface. The near field can drive optical processes in nearby materials, which is the bases for applications like SERS or SEIRA. (Figure inspired from Ref. 58). (b) Simulated absorption coefficient, which is the ratio of the absorption cross section and the cross sectional area of the nanoparticle, for three different nanoparticles. An Ag and an Au sphere with diameters of 20 nm and an Au nanorod with a long axis of 40 nm and a short axis of 10 nm. The particles are embedded in a medium with $\epsilon_m = 2.25$. (c) Simulated near field amplitude enhancement on the surface and around a 20 nm Au nanosphere at $\lambda = 406$ nm. (d) Simulated near field enhancement by an Ag bowtie nanoparticle with an edge length of 30 nm and a height of 5 nm at $\lambda = 700$ nm. All simulations were conducted with the boundary-elements software package MNPBEM.[52]

A localized surface plasmon is a polaritonic excitation, i.e., a mixture of photon and charge oscillation in the metal.[6] Its energy is therefore divided into that of the charges inside the metal and an electromagnetic field around the nanoparticle.[59] The electromagnetic field can be understood as that of a radiating dipole for a small spherical nanoparticle (see Fig. 2.2c).[1] It consists of an electric near field and an intermediate field that are localized around the nanoparticle and a far field that originates from the radiative decay of the plasmon. The near field is strongly confined to the surface of the nanoparticle and its local field intensity can exceed that of the incident light field by orders of magnitude.[5] This leads to a tremendous enhancement of optical processes in nearby molecules or nanomaterials and is the basis for applications like SERS or surface-enhanced infrared absorption spectroscopy (SEIRAS) (see Section 2.2.3).[6] When the shape of the nanoparticle is not spherical the electric near field differs from that of a dipole, which is illustrated for an Au nano-triangle in Fig. 2.2d. Its sharp edges lead to a field-line crowding and a further increase in the near field enhancement.[1] More generally, the local field enhancement increases at corners, sharp edges and tips, which is known as the lightning rod effect. Plasmonic nanoparticles were synthesized in the shape of rods, cubes and stars to achieve maximum field enhancement.[60–62]

2.1.2. Plasmon decay

Plasmons are extremely lossy excitations with a life time τ_{pl} that is typically below 10 fs.[14] This implies a broad spectral line width $\Gamma_{\mathrm{pl}} = 2\hbar/\tau_{\mathrm{pl}}$ of plasmonic resonances, which is useful for broad-band applications like light harvesting[63] but a drawback for applications that require selectivity, like sensing.[46] Different decay channels contribute to the LSP line width

$$\Gamma_{\mathrm{pl}} = \Gamma_{\mathrm{rad}} + \Gamma_{\mathrm{b}} + \Gamma_{\mathrm{surf}}, \tag{2.1}$$

where Γ_{rad} refers to radiative damping, Γ_{b} to losses that occur in the bulk metal and Γ_{surf} to losses at the nanoparticle surface[20] (Fig. 2.3a). Radiative decay occurs because of the direct emission of light by the oscillating charges. It scales with the square of the plasmon dipole moment and is proportional to the nanoparticle volume squared.[6] While the dissipated power by radiative losses Γ_{rad} is proportional to the scattering cross section σ_{sca}, the dissipated power by internal losses $\Gamma_{\mathrm{int}} = \Gamma_{\mathrm{b}} + \Gamma_{\mathrm{surf}}$ scales with the absorption cross section σ_{abs}.[64] The ratio of radiative and internal plasmon linewidth can be obtained

from the optical cross sections

$$\frac{\Gamma_{\mathrm{rad}}}{\Gamma_{\mathrm{int}}} = \frac{\sigma_{\mathrm{sca}}}{\sigma_{\mathrm{abs}}}. \tag{2.2}$$

The contribution from radiative damping to the total plasmon linewidth is plotted for the dipolar plasmon modes of Au and Ag nanospheres in Fig. 2.3b as a function of nanosphere radius. In the case of Au, plasmon decay occurs primarily via internal losses for spheres with diameters smaller than 80 nm because of interband transitions (red line). For Ag, in contrast, radiative damping dominates over internal losses already for particle diameters larger than 40 nm (blue line).

Internal losses in the bulk metal Γ_{b} include the decay into electron-hole pairs and phonons.[13,14] These type of losses are usually assumed to be the same as in the bulk metal and described by the complex dielectric function of the metal $\epsilon(\omega)$. For single plasmonic nanoparticles Γ_{b} is directly obtained from the dielectric function as[59]

$$\Gamma_{\mathrm{b}} = \frac{2\mathrm{Im}[\epsilon(\omega)]}{\frac{\partial}{\partial\omega}\mathrm{Re}[\epsilon(\omega)]}. \tag{2.3}$$

The plasmon line width Γ_{b} is plotted for Au and Ag as a function of excitation energy in Fig. 2.3c. For Au the bulk damping is almost constant in the near infrared with $\Gamma_{\mathrm{b}} \approx 80$ meV but increases dramatically for energies larger than 2 eV because of interband transitions from the d band to the conduction band edge[55] (red line). In the case of Ag the linewidth from bulk damping is almost constant over the visible energy range and with $\Gamma_{\mathrm{b}} \approx 40$ meV smaller than for Au because interband transitions set in at 3.9 eV[66] (blue line). A widely used figure of merit for the strength and spectral width of a plasmon resonance is the quality factor $Q = \omega_{\mathrm{pl}}/\Gamma_{\mathrm{pl}}$.[6,59] The bulk damping in the metal sets an upper limit for the quality factor of a plasmon resonance, which is plotted for single Au and Ag nanoparticles in Fig. 2.3d. The Q factor for a silver nanoparticle (blue line) can reach values of 50 which is twice as large as for gold (red line). Even though Ag clearly outperforms Au in terms of plasmonic properties, Au is the most popular material for experimentalists, because of its resistance against oxidation and chemical reactions with its environment.[5,6]

When the lateral dimension of the nanoparticle approaches the electron mean free path, which is on the order of 20-50 nm for Au and Ag, surface damping Γ_{surf} becomes a sizable contribution to the plasmon linewidth Γ_{pl}.[5,14,53] It refers to the elastic scattering of electrons at the nanoparticle surface, which breaks the linear electron momentum. Surface scattering is an excitation pathway for high-energy electrons or holes at the surface of

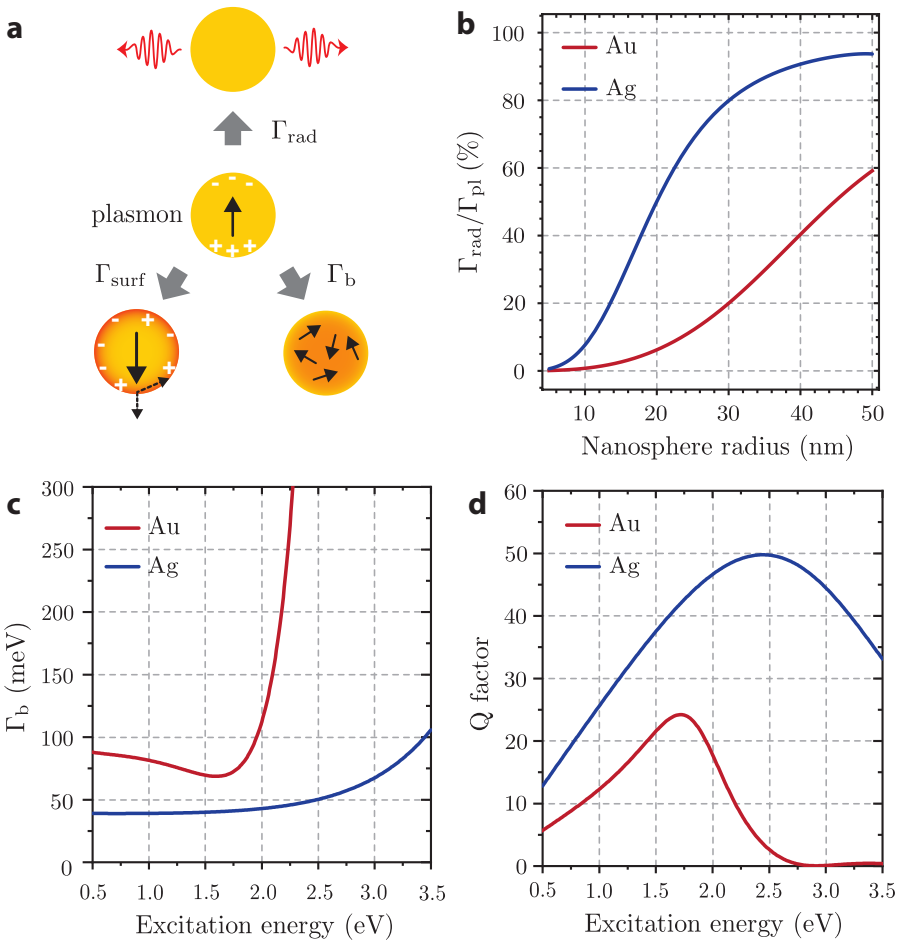

Figure 2.3. Plasmon decay. (a) Sketch of the losses of a localized surface plasmon, i.e., radiative damping Γ_{rad}, bulk damping Γ_{b} and surface damping Γ_{surf}. (b) Contribution of radiative damping Γ_{rad} to the total plasmon linewidth Γ_{pl} of a dipolar plasmon mode in a gold (red) and a silver (blue) nanosphere. The ratios were calculated using Mie theory as $\Gamma_{\mathrm{rad}}/\Gamma_{\mathrm{pl}} = \sigma_{\mathrm{sca}}/\sigma_{\mathrm{ext}}$ with $\sigma_{\mathrm{ext}} = \sigma_{\mathrm{sca}} + \sigma_{\mathrm{abs}}$. σ_{ext}, σ_{sca} and σ_{abs} are the extinction, scattering and absorption cross sections respectively. A surface broadening term $\gamma_{\mathrm{surf}} = v_F/a$ was included in the metal dielectric function, where v_F is the Fermi velocity of the metal and a the nanosphere radius.[53] The dielectric function of the background medium was set to $\epsilon_m = 1.77$. (c) Minimum plasmon line width Γ_{b} and (d) maximum quality factor $Q = \omega_{\mathrm{pl}}/\Gamma_{\mathrm{b}}$ for gold (red) and silver (blue) nanoparticles, as imposed by the bulk damping Γ_b of the metal. The values were calculated from fits of the dielectric functions from Ref. 65 for Au and Ref. 66 for Ag using Eq. (2.3).

the nanoparticle.[20] These "hot" carriers can be used for photocatalysis.[21,22] Recently it was suggested that strongly nonuniform near fields at the particle surface increase Γ_{surf}.[67] Surface damping therefore also occurs in larger nanoparticles with sharp edges and in

nanoparticle assemblies with electromagnetic hot spots.[68,69]

2.1.3. Plasmonic oligomers and dark plasmon modes

When two or more metallic nanoparticles are brought close together their plasmonic excitations interact via the electromagnetic near field.[5,10] The interaction between plasmonic nanoparticles is intuitively described by the language of molecular orbital theory.[15,70] Oligomers, i.e., the assembly of metallic nanoparticles, can be thought as "plasmonic molecules" which support plasmon modes that arise from an hybridization of the individual nanoparticle excitations. This is illustrated for an Au nanodisk dimer in Fig. 2.4a. The dipolar excitations of the two nanodisks hybridize into four plasmon modes, of which two are binding (plasmon energy lowered) and two are anti-binding (plasmon energy increased).[15] The hybridization model is a powerful tool to understand the plasmonic modes of complex metallic nanostructures and their energetic order. It can be even applied to nanostructures with voids and core-shell nanoparticles.[10,15] On the other hand, the model provides no information about which modes are optically active and can be excited by light.

The plasmonic modes of a metallic nanostructure are classified based on their net dipole moment.[15,16] Modes with a net dipole moment couple efficiently to far field radiation and are termed "bright". Modes with a vanishing net dipole moment are termed "dark" as they are in most cases optically inactive. These can be higher-order modes in single nanoparticles or anti-symmetric combinations of dipoles in oligomers.[15,17] According to this classification, the two modes (2) and (4) in Fig. 2.4a are identified as bright because they arise from the symmetric hybridization of the single nanoparticle dipoles. The modes (1) and (3) are comprised of anti-symmetric dipole combinations and are dark. Dark plasmons benefit from suppressed radiative losses that lead to a narrower spectral line width and a longer life time. They are ideal excitations for optical energy storage on the nanoscale, sensing applications, and waveguiding.[11,18]

The hybridization diagram in Fig. 2.4a was obtained from the simulated absorption cross sections in Fig. 2.4b. The bright modes are directly excited by illuminating the dimer from the top with linearly polarized light, along (4, red), and perpendicular (2, green) to the dimer axis. Even though the vanishing dipole moment implies an inactivity of dark plasmons, this is only strictly true if the size of the nanostructure is much smaller than the light wavelength. Plasmonic oligomers have dimensions on the order of 50 - 300 nm[10] which opens a route for the optical excitation of dark plasmons with special illumination

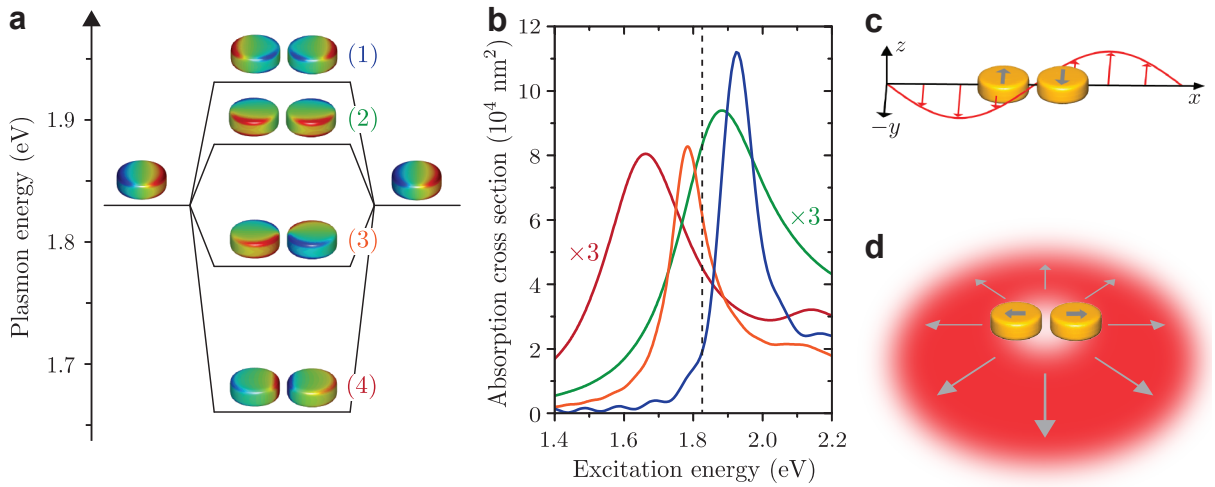

Figure 2.4. Plasmon hybridization and dark plasmons. (a) Hybridization diagram of an Au nanodisk dimer. The surface charges (red - positive, blue - negative) were calculated with the boundary elements method[52] and the energies obtained from the absorption cross sections in (b). (b) Simulated absorption cross sections of a gold nanodisk dimer with 100 nm disk diameter, 20 nm height and 20 nm gap embedded in a medium with $n_{\mathrm{med}} = 1.33$. The plasmon modes illustrated in (a) were selectively excited by (1, blue) illumination with radially polarized light as shown in (d), (2, green) illumination from top with linear polarization perpendicular to the dimer axis, (3, orange) illumination with linear polarization from the side as shown in (c) and (4, red) illumination from the top with linear polarization along the dimer axis. The dashed line shows the dipole plasmon energy of a single nanodisk. Simulations were carried out with the software package Lumerical FDTD solutions. Panels (b) and (c) were adapted from Publication P1 of my thesis.

techniques; see below. Mode (3) of the nanodisk dimer, for example, may be excited by the retarded electric field component of linearly polarized light that impinges on the dimer from the side (Fig. 2.4c). This illumination scheme was suggested by us in Publication P1 of this thesis and recently realized experimentally by Jiang et al. [71] The absorption cross section of (3) is larger than for the bright modes and the peak narrower by a factor of two, which demonstrates the reduced radiative damping (Fig. 2.4b, orange). Mode (1), as a second example, can be optically excited by generating a polarization pattern of the incoming light that matches the plasmonic dipole configuration in the two nanodisks (Fig. 2.4d).[19,72] The spectral line width is again much narrower than for the bright modes (Fig. 2.4b, blue).

The approaches for the optical excitation of dark plasmons can be categorized into specific illumination techniques and specific nanostructure designs. Generally, all dark plasmon modes can be excited and mapped by an electron beam because of its strong spatial

localization.[17,51] This concept was also implemented optically by using the evanescent fields of localized emitters or waveguides as an excitation channel.[16,73] Several approaches have been suggested and demonstrated for the excitation of dark plasmons with far field radiation. These include spatial polarization patterns (see Fig. 2.4d),[19,72] orbital angular momentum beams,[74] field retardation (see Fig. 2.4c)[75,76] and coupling to the magnetic field component.[77,78] Coming to nanostructure designs, dark plasmons were partially turned bright by making nanostructures asymmetric.[79–81] The interaction of originally dark modes with bright modes of the same nanostructure leads to Fano dips in the scattering spectra that are ideal for refractive index sensing.[18,82]

One of the most important properties of plasmonic oligomers for applications are electromagnetic field hot spots in the tiny gaps between the nanoparticles.[6,10] Fig. 2.5a shows the enhancement of the electric field amplitude around a gold nanodisk dimer. The enhancement is largest in the gap because of a field line crowding between the two nanodisks that arises from the optical excitation of the bonding plasmon mode (4) in Fig. 2.4a. When the nanodisks are moved closer together, the field enhancement increases dramatically up to $|E|^2/|E_0|^2 = 2 \cdot 10^4$. For gap sizes below 1 nm the enhancement would decrease again because of the tunneling of electrons between the two nanodisks.[83] The excitation energy for which the maximum enhancement occurs is red shifted when decreasing the gap size because of a stronger coupling between the two nanodisks (Fig. 2.5b).[15] The large concentration of electromagnetic energy in the nanometre gaps between metallic nanoparticles is used to enhance optical processes in nearby materials and is the basis for surface-enhanced Raman scattering (see Section 2.2.3).

With the advance of nanotechnology in the last decades several fabrication techniques have been established for the synthesis of plasmonic oligomers.[10] The most prominent top-down approach is electron-beam lithography.[58,84,85] It is used to fabricate assemblies of nanodisks with large control over their geometry and arrangement on a substrate (Fig. 2.6a). The plasmonic nanostructures used in Project P5 of this thesis were fabricated with this technique. One of the biggest challenges of electron beam lithography is the control over the interparticle gap sizes, especially for gaps below 10 nm.[84] To tackle this challenge, bottom-up approaches are more promising.[86–88] Gold and silver nanoparticles can be grown from metal seeds in solution[87,88] (Fig. 2.6b). By a functionalization with ligand molecules, the nanoparticles can arrange into two- and three-dimensional clusters via a self-assembly process (Figs. 2.6c and d).[86,88] As the interparticle gaps are determined by the length of the ligand molecules, small (2-5 nm) and reproducible gaps are obtained. The controlled arrangement on a substrate is however a challenge. One promising route

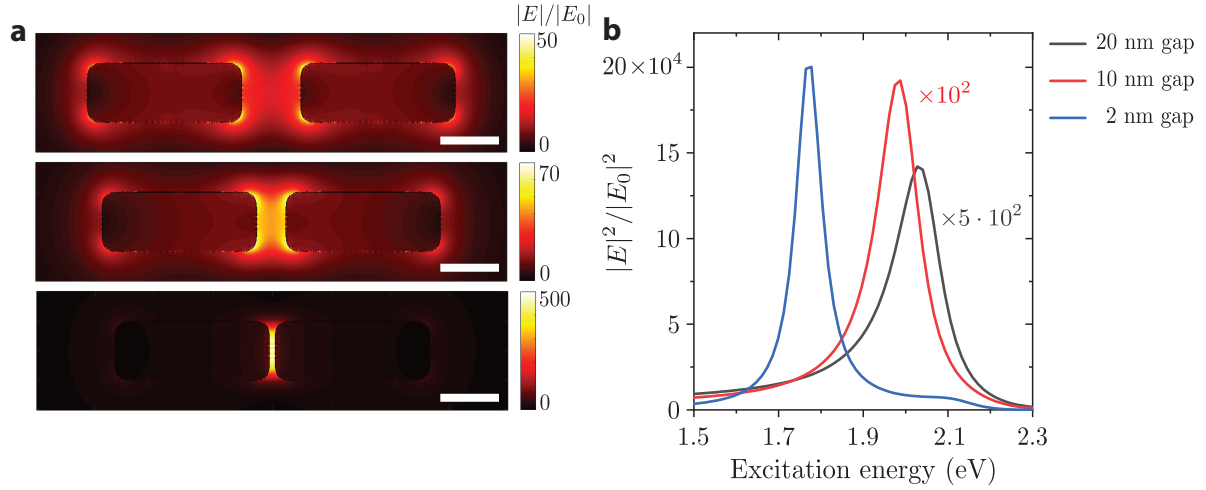

Figure 2.5. Formation of an electromagnetic hot spot in the gap of a gold nanodisk dimer. (a) Simulated enhancement of the electric field amplitude around the nanodimer for different gap sizes of 20 nm, 10 nm and 2 nm, from top to bottom. The scale bars are 20 nm. (b) Excitation energy dependence of the near field intensity enhancement in the center of the interparticle gap. The near field distribution in (a) is shown for the excitation energies that lead to the largest field enhancement. The simulations were carried out with the boundary elements method.[52]

towards large structural order over multiple length scales is the periodic arrangement of nanoparticles into close-packed lattices via a self-assembly process at a liquid-liquid interface (Fig. 2.6e).[89] Such nanoparticle films were used in Projects P1 and P2 of this thesis.

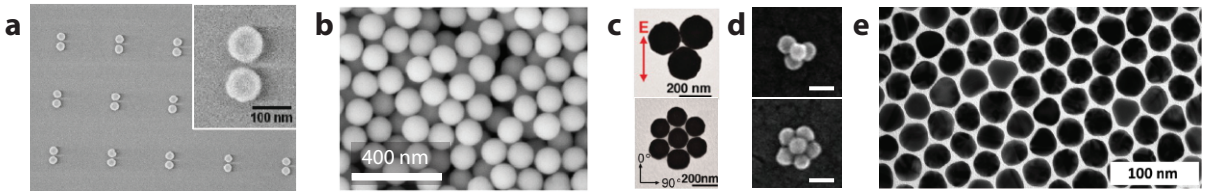

Figure 2.6. Plasmonic gold nanostructures fabricated with different approaches. (a) Nanodisk dimers produced by electron beam lithography on a substrate surface.[58] (b) Spherical nanoparticles grown from metal seeds in solution.[90] (c) Self-assembled two dimensional[86] and (d) three dimensional nanoclusters of chemically synthesized nanoparticles.[91] Scale bars in (d) are 50 nm. (e) Hexagonal lattice of chemically synthesized nanoparticles obtained by a self-assembly at a liquid-liquid interface.[89]

2.1.4. Analytical and numerical modeling of localized surface plasmons

One key advantage of plasmonic nanostructures is that their optical properties can be modeled by classical electrodynamics.[92,93] The analytic and numeric approaches are based on a solution of Maxwell's equations in the presence of nanoscale dielectric media. Such problems can be tackled analytically for specific nanostructure geometries[6,93] or numerically for almost any nanostructure.[92,94] In the following, I will describe and compare different analytical and numerical approaches that are frequently used for the interpretation of experiments and the systematic design of plasmonic nanostructures.

A simple analytical model

The main ingredients needed to model the optical response of a metallic nanoparticle are its dielectric function, the nanoparticle geometry and the type of light source.[93] I consider a (spherical) nanoparticle illuminated by an electromagnetic plane wave. Full analytic solutions are provided for this scattering geometry by Mie theory.[6,95] I will discuss analytic expressions obtained with the quasi-static approximation because these are most insightful. This approximation applies to nanoparticles much smaller than the wavelength of the incident light.

The optical properties of metals are modeled with a dielectric function

$$\epsilon(\omega) = \epsilon_b(\omega) - \frac{\omega_\mathrm{p}^2}{\omega^2 + \mathrm{i}\omega\Gamma_\mathrm{b}/2} \tag{2.4}$$

that consists of two terms:[1,6] The second term describes the motion of the conduction electrons that move freely within the bulk, where $\omega_\mathrm{p}^2 = \mathcal{N}e^2/(\epsilon_0 m_e)$ is the bulk plasma frequency that depends on the density of free electrons $\mathcal{N}$. Γ_b is the bulk damping discussed in Section 2.1.2. e and m_e are the electron charge and mass and ϵ_0 is the vacuum dielectric constant. The first term $\epsilon_b(\omega)$ describes the contribution from the bound electrons. In the Drude model it is approximated as a constant $\epsilon_b(\omega) = \epsilon_\infty$ that describes the screening of the free electron response by the bound electrons far away from optical transitions.[55,56,66] Figure 2.7 shows the measured refractive index $n(\omega) = \sqrt{\epsilon(\omega)}$ of (a) gold and (b) silver (black dots) and a fit with Eq. (2.4) (orange curves). The Drude model nicely describes the experimental data for silver in the visible spectral range.[66] In the case of gold it only describes the optical response for energies smaller than 2 eV. For larger energies,

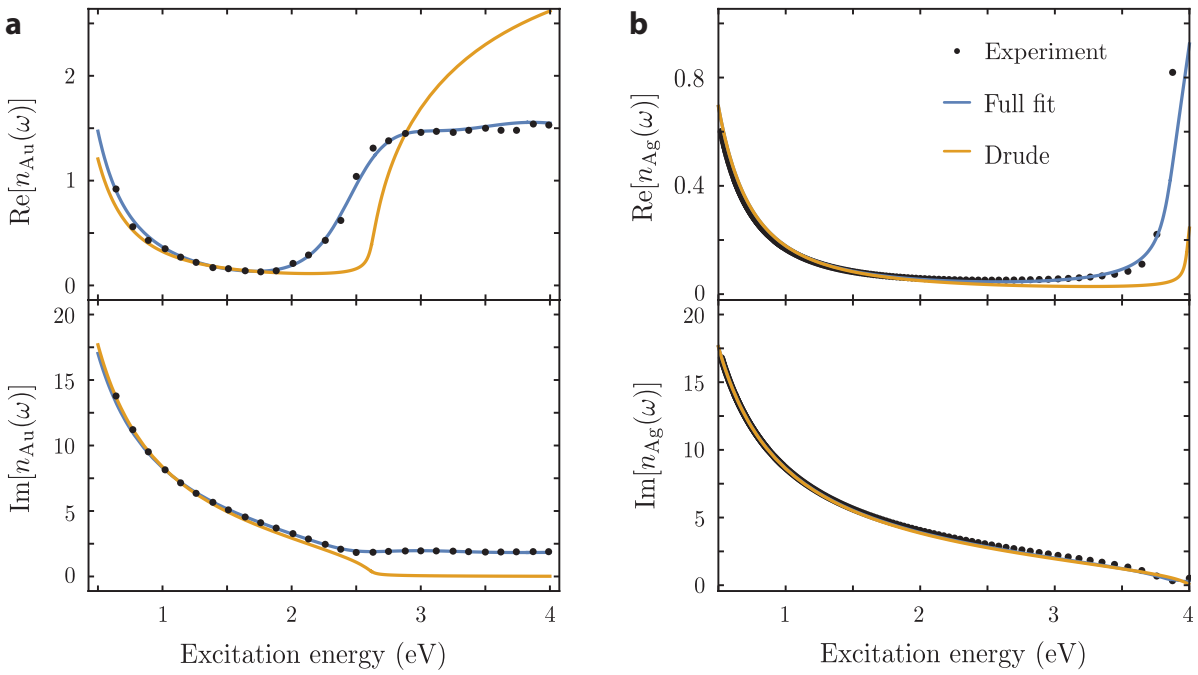

Figure 2.7. Refractive index of (a) Au and (b) Ag. The black dots show experimental data measured by Johnson and Christy for Au[65] and Yang et al. for Ag.[66] The orange lines are a fit with the Drude model in Eq. (2.4) using $\epsilon_b(\omega) = 12$, $\omega_p = 9.071$ eV and $\Gamma_b = 132$ meV for Au and $\epsilon_b(\omega) = 5$, $\omega_p = 8.9$ eV and $\Gamma_b = 78$ meV for Ag. The blue lines are a full fit including resonant terms in $\epsilon_b(\omega)$; see e.g. Ref. 96 for Au.

the dielectric response is dominated by interband transitions from the 5d band to the conduction band edge.[55] This can be modeled by including resonant terms in $\epsilon_b(\omega)$ (blue curves).[96]

In the following, I will consider a single metallic nanoparticle which is small enough that the phase of the incident light field can be approximated constant over its diameter. When still considering the time dependence $e^{i\omega t}$ of the incident light field this is known as the quasi-static approximation. In response to the external electric field $\mathbf{E}_0 e^{i\omega t}$, the conduction electrons are driven periodically to one of the nanoparticle boundaries generating a depolarization field inside the nanoparticle.[56] This leads to the formation of a dipole moment $\mathbf{p} = \alpha \mathbf{E}_0$, with the polarizability[6]

$$\alpha(\omega) = 3\epsilon_0 \epsilon_m V_{NP} \beta(\omega) \tag{2.5}$$

of the nanoparticle. V_{NP} is the nanoparticle volume and ϵ_m is the dielectric function of

the surrounding medium. The frequency dependence of the optical response is given by[6]

$$\beta(\omega) = \frac{1}{3L}\frac{\epsilon(\omega) - \epsilon_m}{\epsilon(\omega) + \epsilon_m(1/L - 1)}, \tag{2.6}$$

and depends on the dielectric functions of the metal and the surrounding medium. L is a geometry dependent factor that must be included because the internal depolarization field depends sensitively on the nanoparticle shape and polarization direction of the incident light field; $L < 1$ for any nanoparticle and $1/3$ for a nanosphere.[56] As can be seen from Eq. (2.6), a resonance occurs when $\mathrm{Re}[\epsilon(\omega)] + \epsilon_m(1/L - 1) \approx 0$, which is often referred to as Fröhlich condition.[5,6] For metals this condition can be matched because $\mathrm{Re}[\epsilon(\omega)] < 0$ below the plasma frequency ω_p, which leads to pronounced localized surface plasmon resonances in the visible spectral range. Within the Drude model the LSP frequency is given by

$$\omega_\mathrm{pl} = \frac{\omega_\mathrm{p}}{\sqrt{\epsilon_\infty + \epsilon_m(1/L - 1)}}. \tag{2.7}$$

It depends on the type of metal via ω_p and ϵ_∞, the dielectric environment ϵ_m, and the shape of the nanoparticle L. It was suggested recently to use $\beta(\omega)$ as a plasmonicity index to classify whether an optical excitation of a nanoparticle is plasmonic or non-plasmonic (e.g. photonic).[49]

The optical cross sections are obtained by dividing the power that is dissipated P_abs or scattered P_sca by the plasmonic dipole of the nanoparticle by the power density S_inc of the incident light.[1,6] This leads to the simple expressions

$$\sigma_\mathrm{abs}(\omega) = \frac{P_\mathrm{abs}}{S_\mathrm{inc}} = \frac{k_m}{6\epsilon_0\epsilon_m}\mathrm{Im}[\alpha(\omega)] \tag{2.8}$$

for the absorption cross section and

$$\sigma_\mathrm{sca}(\omega) = \frac{P_\mathrm{sca}}{S_\mathrm{inc}} = \frac{k_m^4}{6\pi\epsilon_0^2\epsilon_m^2}|\alpha(\omega)|^2 \tag{2.9}$$

for the scattering cross section. $k_m = \sqrt{\epsilon_m}\omega/c$ is the wavenumber of the incident light. As $\alpha(\omega) \propto V_\mathrm{NP}$, the absorption cross section scales with V_NP and the scattering cross section with V_NP^2. Optical absorption therefore dominates for small nanoparticles while scattering is most important for large nanostructures. This is the reason why internal losses dominate over radiative losses for small nanoparticles and the reversed is true for large nanoparticles; see Eq. (2.2) and Fig. 2.3b.

Finally, the electric field amplitude around a small plasmonic nanoparticle can be approximated as that of a radiating dipole[1]

$$\mathbf{E}_{\mathrm{pl}}(r\mathbf{n}) = \frac{\mathrm{e}^{-\mathrm{i}\omega t}}{4\pi\epsilon_0}\left[k_m^2(\mathbf{n}\times\mathbf{p})\times\mathbf{n}\frac{\mathrm{e}^{\mathrm{i}k_m r}}{r} + [3\mathbf{n}(\mathbf{n}\cdot\mathbf{p})-\mathbf{p}]\left(\frac{1}{r^3}-\frac{\mathrm{i}k_m}{r^2}\right)\mathrm{e}^{\mathrm{i}k_m r}\right], \qquad (2.10)$$

when neglecting the lightning rod effect; i.e. considering a nanosphere. It consists of a transverse far field that is radiated perpendicular to the dipole and drops with the distance r to the nanoparticle center [left term in Eq. (2.10)]. The right term contains longitudinal and transverse field components. It consists of a near field that drops with $1/r^3$ and therefore gives a considerable contribution close the nanoparticle surface. Second, it consists of an intermediate field $\propto 1/r^2$ that is most important for a distance to the nanoparticle center on the order of the light wavelength.[1] The interaction between plasmonic nanoparticles in oligomers, as discussed in Sec. 2.1.3, is mediated by the electric near field.[10] It is also the near field that is responsible for the large field enhancement close to the nanoparticle surface and the formation of hot spots in interparticle gaps.[6] When nanoparticles are periodically arranged into a lattice with distances on the order of the light wavelength an interaction via the intermediate field leads to the formation of lattice resonances that can have very large quality factors.[97]

Numerical approaches

All numerical methods for modeling the optical response of nanostructures rely on a process of discretization and an algorithm that solves a set of analytic equations on finite or infinite domains.[92] They are categorized into differential or integral approaches depending on whether Maxwell's equations are solved in their differential or integral form.[98] Fig. 2.8 shows the discretization used by the four most widely employed methods based on the example of a gold nanorod on top of a substrate.[92] In the finite-difference time-domain (FDTD) method the entire 3D space and time are discretized into cubic cells and Maxwell's equations are solved iteratively in space and time (Fig. 2.8a).[99,100] This is a powerful approach for the simulation of complex nanostructures and is applied to a wide range of problems including the propagation of light in nanoscale materials. Another differential approach is the finite element (FE) method where space is discretized into tetrahedral elements which is of advantage for simulating curved surfaces (Fig. 2.8b).[101] The wave equation of the electric field is solved in the frequency domain which permits obtaining the electromagnetic eigenmodes of a nanostructure.

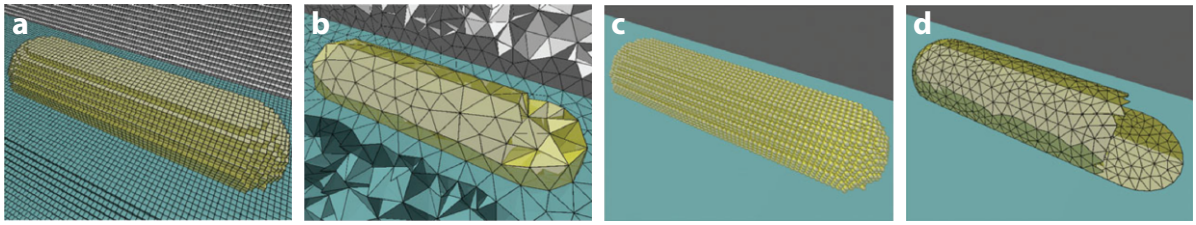

Figure 2.8. Discretization of space used in different numerical methods for the simulation of plasmonic nanostructures, illustrated for a gold nanorod placed on top of a substrate. Figure adapted from Ref. 92. (a) Finite-difference time-domain (FDTD) method where the entire 3D space is discretized into cubes. (b) Finite element (FE) method with a discretization of the entire 3D space into tetrahedral elements. (c) Volume-integral equation (VIE) approaches such as the discrete dipole approximation (DDA) where only the nanoparticle volume is discretized. (d) Surface-integral equation (SIE) methods such as the boundary elements method (BEM) where only the nanoparticle surface is discretized. In the last two approaches the electric field in the surrounding is calculated with Green functions.

Integral approaches also operate in the frequency domain and rely on a discretization of only the nanoparticle volume (Fig. 2.8c) or its surface (Fig. 2.8d), but not the surrounding space.[1,102–104] The electric field around the nanoparticle is calculated with dyadic Green functions which makes these methods powerful for calculating the scattering of light by nanostructures. Several hybrid approaches were developed to combine the advantages of the aforementioned methods.[94,105] In the following, I will discuss the FDTD method and a surface-integral approach called boundary elements method (BEM) in greater detail, as these were used in the projects associated with this thesis.

The finite-difference time-domain method is based on an algorithm that solves Maxwell's equations on a discrete mesh in space and time.[92,99,100] The most popular algorithm was developed by Yee in 1966.[106] It is based on a rectangular grid where the electric and magnetic field components are spatially displaced in order to calculate the curl operators that occur in Maxwell's equations (see Fig. 2.9a). By discretizing the differential Maxwell's equations, the electric field at time t is calculated from the electric and magnetic field components at previous time steps in a leapfrog manner.[92,98,100] The same applies to the magnetic field. This algorithm only requires storing the electric and magnetic field components of the previous time step which greatly reduces the required memory. A criterion for the stability of the algorithm is the Courant condition[99,107]

$$c\Delta t <= \frac{1}{\sqrt{\Delta x^{-2} + \Delta y^{-2} + \Delta z^{-2}}}, \tag{2.11}$$

where Δt is the discretization in time and Δx, Δy and Δz the discretization in space. The rectangular mesh makes the modeling of curved interfaces a challenge. A very small discretization is necessary to avoid staircasing effects like glowing pixels in the electric field distribution at a nanoparticle surface (see Fig. 2.9b). Special meshing technologies, such as non-uniform meshing[108] and conformal meshing algorithms,[99,109] have been developed to circumvent this problem and reduce the required computation time and memory.

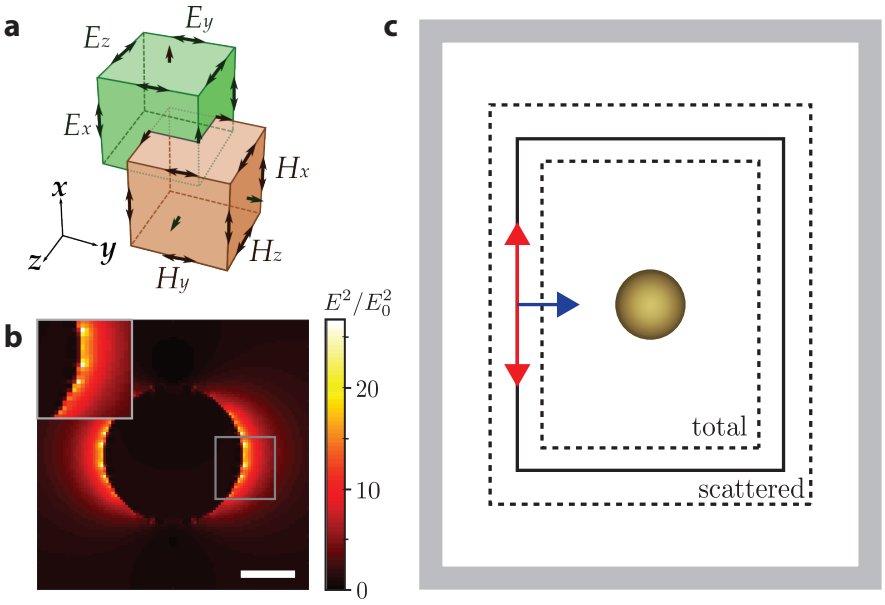

Figure 2.9. The finite-difference time-domain (FDTD) method. (a) Sketch of the Yee grid that is used for an iterative solution of Maxwell's equations in space and time. The electric and magnetic field components are spatially displaced to calculate the numerical curls. Figure from Ref. 110. (b) Simulated electric field enhancement around a gold nanosphere with 50 nm diameter at $\lambda = 530$ nm. A 1 nm mesh is used and conformal meshing algorithms are disabled to illustrate staircasing effects that lead to glowing pixels at the nanoparticle surface. (c) Sketch of the computational cell that is used for a simulation of the optical cross sections of a gold nanoparticle. A total-field scattered-field source (box by black solid lines) separates the computational domain into a region that contains the incident and scattered light and into a region of only the scattered light (red arrows - polarization, blue arrow - wavevector). The power flux is recorded by monitors (dashed lines) in the total and scattered field regions to calculate the absorption and scattering cross sections. The computational domain is limited by perfectly matched layers that absorb light without backreflections (gray box).

The peculiarities of FDTD are best understood from the layout and workflow of a simulation. As an example, Fig. 2.9c shows the computational domain for simulating the scattering and absorption cross section of a gold nanoparticle. A special light source called

total-field scattered-field (TFSF) is used for this purpose (box of black solid lines in Fig. 2.9c).[111,112] It splits the computational domain into a region that contains the total field (incident and scattered field) and a region that only contains the field scattered by the nanoparticle. A light pulse is injected by the source and the time dependent power flux is recorded by monitors in the total and scattered field regions to obtain the absorption and scattering cross sections respectively (dashed boxes in Fig. 2.9c). The simulation is stopped when the electric field drops below a threshold. The frequency response of the nanoparticle is then obtained from a Fourier transformation of the time signal measured by the monitors.[92,99] This way it is possible to obtain the absorption and scattering cross sections across the entire visible spectral range from a single simulation.

The numerical solution of Maxwell's equations in the time domain leads to several challenges. The discretization of the entire 3D space requires a finite size of the computational domain to maintain a tractable memory effort. Special absorbing boundaries, called perfectly matched layers (PML), have been developed to avoid backreflections that would hinder a convergence of the simulation (grey box in Fig. 2.9c).[113,114] Another option are periodic boundary conditions in one or two directions. These require, however, that light is injected at normal incidence to the periodic nanostructure; otherwise the field propagation would have to be calculated forward and backward in time.[92,99] The materials are modeled based on their dielectric functions measured in experiments. As outlined above the dielectric function of a metal is frequency dependent and the dispersion is of central importance for the plasmon resonance frequency. The frequency-dependent data must be turned into a time dependent susceptibility, which is not straight forward.[92] Several methods have been developed to tackle this problem and avoid the storage of field values at all times.[115,116]

Another numerical tool that was used in this thesis is the boundary elements method (BEM) which was developed by G. J. Garcia de Abajo and A. Howie[104,117] and implemented as an open source software package MNPBEM by U. Hohenester and coworkers.[50,52,118] The boundary elements method relies on a discretization of a nanoparticle surface into small elements. The surface charges and surface currents are calculated at the centroids of each surface element (collocation method) by a solution of the Helmholtz equation for the scalar and vector potential and Maxwell's boundary conditions (Fig. 2.10a).[50] The interaction of the point-like surface charges and currents with those of other elements are calculated with Green functions which are the work horse of the boundary elements method.[119] There are two approaches for the solution of the Helmholtz equation: In the direct method, the scalar and vector potentials in 3D space are computed only from the potentials and

their derivatives at the particle boundary using Green's second theorem.[50] The indirect method is based on equations for the potentials that satisfy the Helmholtz equation by construction, everywhere except at the particle boundary.[104,117] It therefore relies on artificial surface charges and currents. While the indirect method is computationally less expensive, the direct method benefits from a physical meaning of the calculated surface charges and currents.[50] The equations used in the direct method can also be rewritten as an eigenvalue problem which allows to calculate the plasmonic eigenmodes and plasmon energies of metallic nanostructures (Fig. 2.10b).[50]

One key advantage of BEM compared to FDTD is that only the nanoparticle surface needs to be discretized, which greatly reduces the computational effort.[92] The electric fields around the plasmonic nanostructure are calculated directly with Green functions, which makes the calculation of the far field cross sections (extinction, scattering and absorption)

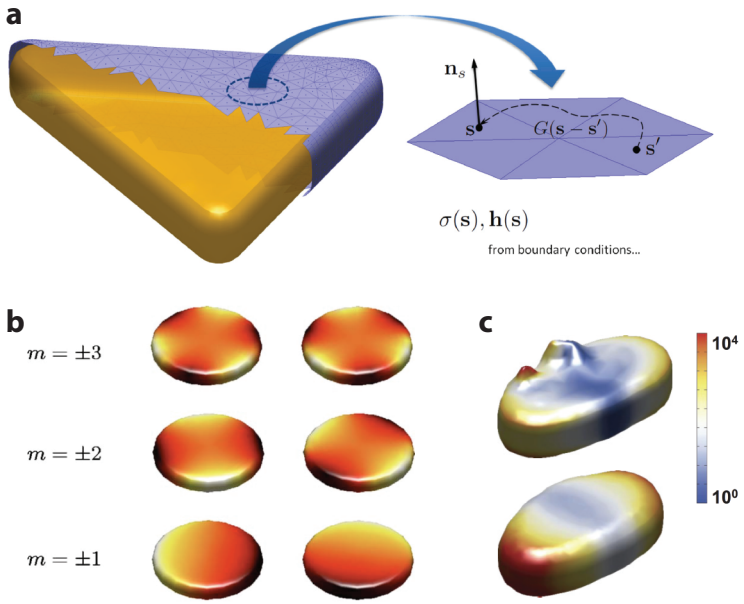

Figure 2.10. Boundary elements method (BEM). (a) Discretization of a nanoparticle surface by triangular elements. The surface changes $\sigma(\mathbf{s})$ and surface currents $\mathbf{h}(\mathbf{s})$ are calculated numerically at the center $\mathbf{s}$ of each element. The interaction of charges and currents at different elements is calculated with Green functions $G(\mathbf{s}-\mathbf{s}')$. Figure from Ref. 119. (b) Plasmon modes of a nanodisk calculated with an eigenmode expansion using the boundary elements method. The plot shows the surface charges $\sigma(\mathbf{r})$ (red - positive and yellow - negative) of dipole ($m = \pm 1$), quadrupole ($m = \pm 2$), and hexapole ($m = \pm 3$) modes. Figure from Ref. 50. (c) Simulated SERS enhancement at the surface of a gold nanoparticle with surface roughness (top) and without (bottom) displayed with a logarithmic scale. Figure from Ref. 120.

straightforward.[92,119] Furthermore, BEM allows to model rough metal surfaces and calculate the electric near fields close to the surface of metallic nanoparticles having realistic geometries (Fig. 2.10c).[120,121] While surface distortions and nanoscopic roughness have only a minor effect on the far field response, their effect on the electric field enhancement can be dramatic, which makes accurate modeling important for applications like SERS or nonlinear optics.[120,122,123] Besides these advantages, BEM also has several drawbacks compared to FDTD: BEM is limited to the modeling of piecewise homogeneous nanoobjects, i.e. having a constant dielectric function within the volume of the nanoparticle.[50,92,117] Furthermore, the computation of electric fields around a plasmonic nanostructure in the presence of a substrate is not trivial as all information about the environment must be included in the Green functions.[92,118] As a frequency-domain method, BEM does not permit to calculate the propagation of electromagnetic waves in the presence of nanoscale media,[92] and finally, an implementation of the boundary elements method for periodic nanostructures remains missing.

2.2. Raman scattering

Raman spectroscopy is a non-destructive technique for the optical characterization of materials.[124,125] It refers to the inelastic scattering of light by the excitation (Stokes scattering) or annihilation (Anti-Stokes scattering) of vibrations in solid-state materials and molecules (Fig. 2.11a and b). The technique probes the vibrational properties of materials with visible light even though the vibrational frequencies are in the infrared. It is, therefore, complementary to infrared absorption spectroscopy[126] (Fig. 2.11c). Raman spectroscopy is a powerful tool to probe materials properties, such as electronic states, strain, doping, defects and temperature.[124,127] The Raman spectrum is often regarded as a fingerprint for the structure of a molecule. A bottleneck for applications is that Raman scattering is an inherently weak effect; the Raman efficiency of a molecule is typically ten orders of magnitude lower than its florescence yield.[128,129] It is therefore experimentally challenging to separate the Raman spectrum from the Rayleigh scattered light (Fig. 2.11d) and often also from a much stronger fluorescence background.[130] A popular technique to

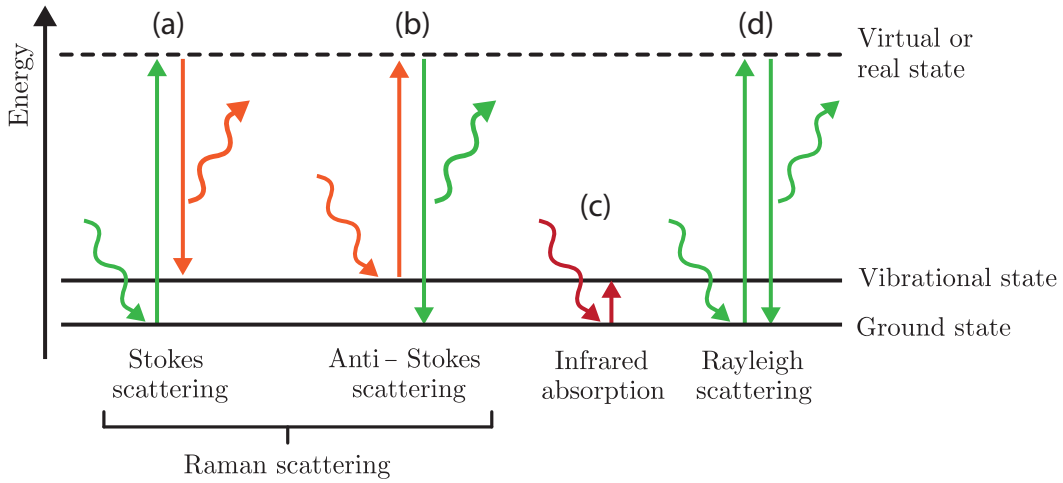

Figure 2.11. Sketch of Raman scattering- and related optical processes. (a) Stokes Raman scattering where a vibration is excited and the Raman-scattered light (orange arrow) has less energy than the incoming light (green arrow). The scattering process involves an intermediate state which can be real or virtual. The process is termed resonant Raman scattering if the intermediate state is a real state. (b) Anti-Stokes Raman scattering process where a vibration is annihilated and the Raman-scattered light has more energy than the incoming light. (c) Infrared absorption where a vibrational transition is directly excited by the incoming light. This process cannot involve a virtual state. (d) Rayleigh (elastic) scattering where incoming and scattered light have the same energy.

increase the Raman scattering efficiency is surface-enhanced Raman scattering (SERS) which uses the intense electric fields of plasmonic hotspots to enhance the Raman scattering rate of molecules and nanomaterials.[6] In the following I will discuss the theoretical and experimental basics of Raman scattering and introduce surface-enhanced Raman scattering as a direct application of plasmonics.

2.2.1. Theoretical description of Raman scattering

Theoretical modeling of Raman scattering can be best understood from a phenomenological equation for the Raman polarizability.[6,125] I consider a spontaneous Stokes Raman process which is depicted for a molecule in Fig. 2.12a and for a solid-state material in Fig. 2.12b. The electric field $\mathbf{E}_{\mathrm{inc}}(\omega_{\mathrm{L}})$ of the incident laser light induces a Raman dipole moment in the material

$$\mathbf{p}_{\mathrm{R}}(\omega_{\mathrm{S}}) = \overleftrightarrow{\alpha}_{\mathrm{R}}(\omega_{\mathrm{L}}, \omega_{\mathrm{S}})\mathbf{E}_{\mathrm{inc}}(\omega_{\mathrm{L}}), \tag{2.12}$$

where ω_{L} is the frequency of the incoming laser light, $\omega_{\mathrm{S}} = \omega_{\mathrm{L}} - \omega_{\mathrm{vib}}$ the frequency of the Raman-scattered light, and ω_{vib} the frequency of the vibration that is excited. All information about the Raman process is contained in the Raman polarizability tensor $\overleftrightarrow{\alpha}_{\mathrm{R}}(\omega_{\mathrm{L}}, \omega_{\mathrm{S}})$, which is in general a second rank tensor with components $\alpha_{ij} = \alpha^*_{ji}$.[6,124] The Raman tensor components are measured in an experiment by choosing a specific polarization $\mathbf{e}_{\mathrm{inc}}$ for the incoming light and placing an analyzer along $\mathbf{e}_{\mathrm{scat}}$ in front of the spectrometer (see Section 2.2.2). The intensity of the Raman-scattered light is in this case[6,124]

$$I_{\mathrm{R}} \propto |\mathbf{e}_{\mathrm{scat}} \cdot \overleftrightarrow{\alpha}_{\mathrm{R}} \cdot \mathbf{e}_{\mathrm{inc}}|^2, \tag{2.13}$$

and vanishes for certain combinations of $\mathbf{e}_{\mathrm{inc}}$ and $\mathbf{e}_{\mathrm{scat}}$, which is known as Raman selection rules. The symmetry of the Raman tensor may be obtained with group theory, which analyzes the symmetry of the vibrations and optical transitions in a material.[131]

The theoretical approaches to calculate the Raman tensor of a given material are classified as macroscopic or microscopic.[124] The macroscopic theories are based on a Taylor expansion of the material susceptibility with respect to the atomic displacements.[6,124,125] This leads to an intuitive picture of Raman scattering with classical equations. The microscopic theories describe Raman scattering with time-depend perturbation theory and give insight into the intermediate steps of a Raman scattering process.[124,125,132–134] In the following I will introduce the general theoretical framework of the latter approach for molecules and solid-state materials.

The explicit steps of a first-order Stokes Raman process are illustrated for a molecule in Fig. 2.12a. The optical transitions are typically drawn in an energy level diagram of vibronic states, which are coupled vibrational and electronic eigenstates of the molecule [125] (Fig. 2.12a). The incoming laser light ω_L excites an optical transition from the ground state g to an intermediate state i. In a second step, the Raman-scattered light $\omega_\mathrm{S} = \omega_\mathrm{L} - \omega_\mathrm{vib}$ is emitted by a transition from the intermediate state to a final vibronic state f. While the initial and final states must be real vibronic states of the molecule, the intermediate state can be virtual. If the intermediate state is a real vibronic state one speaks of resonant Raman scattering.

A slightly different picture of Raman scattering has been established for solid-state materials (Fig. 2.12b). [124,133,134] In a solid, the vibrational and electronic states are typically assumed to be decoupled, which is known as the Born-Oppenheimer approximation. A first-order Raman scattering process therefore involves three steps, which are drawn in an exemplary electronic band structure in Fig. 2.12b. First, the incoming laser light ω_L excites a transition from the valence band $\epsilon_\mathrm{v}(k)$ to the conduction band $\epsilon_\mathrm{c}(k)$ or a virtual electronic state. Second, a vibration/phonon ω_pn is excited, which involves a transition to a second intermediate electronic state (may be virtual). Third, the Raman-scattered light $\omega_\mathrm{S} = \omega_\mathrm{L} - \omega_\mathrm{pn}$ is emitted by a transition to the initial electronic state in the valence band, as energy and momentum need to be conserved. This picture nicely shows that Raman scattering is mediated by electronic transitions even though the electronic states remain unchanged after the scattering process. [124]

The scattering processes in Figs. 2.12a and b are illustrated in a more compact way by Feynman diagrams (Figs. 2.12c and d). [124,125] In these diagrams excitations are drawn as lines and interactions as vertices. The advantage of illustrating a Raman process this way is that the Feynman diagrams can be directly translated into Raman-scattering amplitudes using perturbation theory (see Refs. 124 and 134 for details). The Raman tensor element for the process depicted in Fig. 2.12c is given by the scattering amplitude [125]

$$\alpha_{kl} = \sum_i \frac{\langle f|\mathcal{H}^k_{\mathrm{pt-vib}}|i\rangle\langle i|\mathcal{H}^l_{\mathrm{vib-pt}}|g\rangle}{\hbar\omega_\mathrm{L} - (\epsilon_i - \epsilon_g) - \mathrm{i}\gamma_i}, \tag{2.14}$$

which corresponds to second-order perturbation theory. Each vertex of the Feynman diagram corresponds to one of the matrix elements $\langle f|\mathcal{H}^k_{\mathrm{pt-vib}}|i\rangle$ and $\langle i|\mathcal{H}^l_{\mathrm{vib-pt}}|g\rangle$ that describe the interaction strength between the vibronic transitions of the molecule and light. The energy denominator accounts for the excitation-energy dependence when the incident

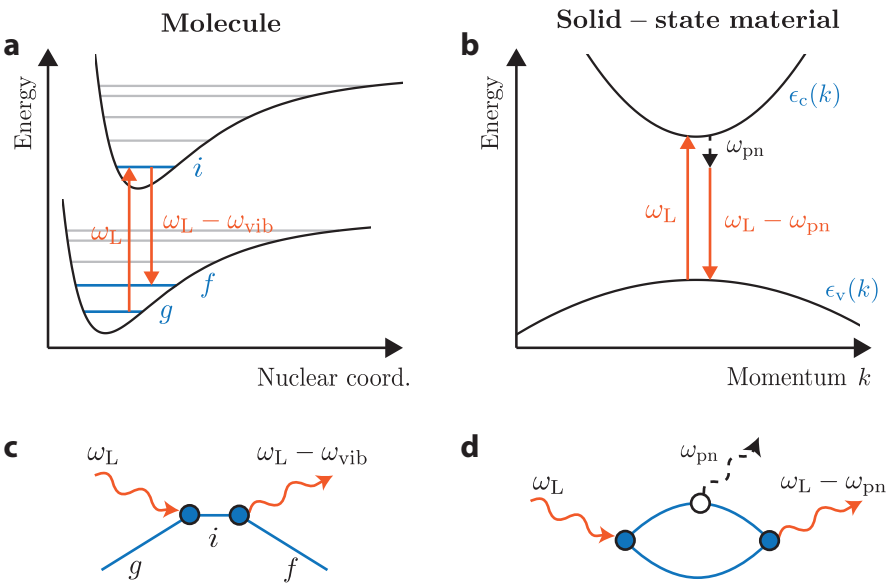

Figure 2.12. Microscopic description of Raman scattering in molecules and solids. (a) First-order resonant Stokes Raman process depicted in the vibronic energy levels of a molecule. The incoming laser light ω_L induces a transition from the ground state g to an intermediate state i. The Raman-scattered light $\omega_L - \omega_{vib}$ is emitted by a transition $i \to f$ to the final state f. (b) First-order resonant Stokes Raman process depicted in the electronic band structure of a solid-state material. The incoming light excites a transition from the valence band $\epsilon_v(k)$ to the conduction band $\epsilon_c(k)$. A photon (lattice vibration) ω_{pn} is excited by a transition to a second intermediate state. Finally, the Raman-scattered light is emitted by a transition to the initial electronic state. (c) and (d) depict the Raman processes in (a) and (b) as Feynman diagrams.

light ω_L is detuned from the molecular transition $\epsilon_i - \epsilon_g$. An energy broadening term γ_i is included to account for the finite lifetime $\tau_i = \hbar/\gamma_i$ of the intermediate vibronic state. The excitation of a virtual intermediate state is described as the off-resonant excitation of a real state. It is important to note that the Raman scattering process is instantaneous and the two steps cannot take place individually.[6]

Similarly, the Feynman diagram for Raman scattering in a solid-state material can be translated into the scattering amplitude[124,134]

$$\alpha_{kl} = \sum_{n,n'} \frac{\langle f|\mathcal{H}^k_{\text{pt-el}}|n'\rangle\langle n'|\mathcal{H}_{\text{el-pn}}|n\rangle\langle n|\mathcal{H}^l_{\text{el-pt}}|g\rangle}{[\hbar\omega_L - \hbar\omega_{pn} - (\epsilon_{n'} - \epsilon_g) - i\gamma_{n'}]\,[\hbar\omega_L - (\epsilon_n - \epsilon_g) - i\gamma_n]}, \tag{2.15}$$

which corresponds to third-order perturbation theory. The scattering amplitude differs from Eq. (2.14) for the molecule in that it contains one additional matrix element and energy

dominator. The interaction Hamiltonians $\mathcal{H}_{\mathrm{pt-el}}$, $\mathcal{H}_{\mathrm{el-pn}}$ and $\mathcal{H}_{\mathrm{el-pt}}$ account explicitly for the photon-electron and electron-phonon coupling in the three steps of the Raman process (Fig. 2.12b and d). The energy denominators vanish when the incoming laser light ω_{L} matches an electronic transition $\epsilon_n - \epsilon_g$ and when the Raman-scattered light $\omega_{\mathrm{S}} = \omega_{\mathrm{L}} - \omega_{\mathrm{pn}}$ matches an electronic transition $\epsilon_{n'} - \epsilon_g$. This leads to incoming- and outgoing Raman resonances, which can be observed experimentally by measuring the intensity of a Raman mode as a function of excitation energy.[124,134]

The different descriptions for Raman scattering in molecules and solids arise from the Born-Oppenheimer approximation that decouples the vibrational and electronic states. In fact, this approximation also applies well to the vibronic states of molecules and is often used when calculating the matrix elements in Eq. (2.14).[125] The connection of the two descriptions was discussed in detail in Refs. 134,135.

2.2.2. Experimental methods

A typical set up for polarized micro-Raman spectroscopy, as it was used in this thesis, is shown in Fig. 2.13.[124,127,136] The monochromatic light of a laser is guided through a beam splitter (BS) into an optical microscope and focused on the sample. The Raman- and Rayleigh-scattered light is collected and collimated by the same microscope objective (backscattering configuration). A notch filter (NF) rejects the Rayleigh-scattered light such that only the Raman-scattered light passes into a spectrometer. The Raman spectrum is finally recorded with a CCD detector.[137]

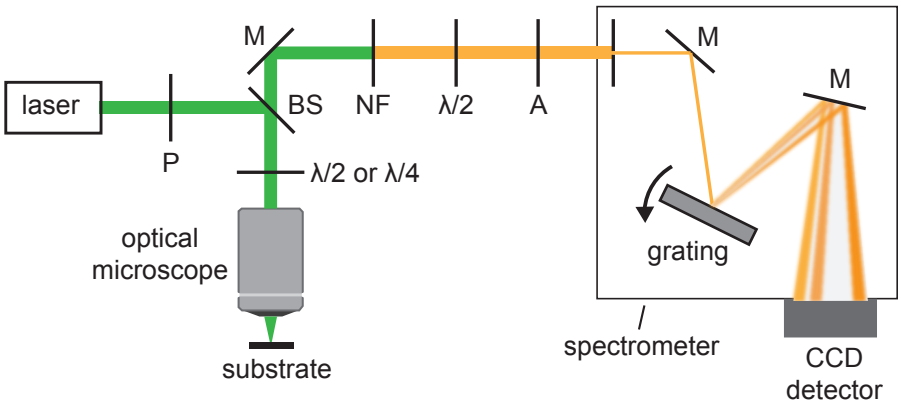

Figure 2.13. Typical set up of a micro-Raman spectrometer, which consists of a laser, an optical microscope, a spectrometer with CCD detector and the optical elements: polarizer - P, half-wave plate $\lambda/2$, quarter-wave plate $\lambda/4$, beam splitter BS, mirror M, notch filter NF and analyzer A.

The experimental challenge of Raman spectroscopy is to efficiently collect the weak Raman signal and separate it from other light sources, such as the Rayleigh-scattered light and stray light.[124] This requires optimized optical components, an efficient collection and isolation of the Raman-scattered light and a set up that rejects stray light. A continuous-wave (CW) laser is most suitable as light source for spontaneous Raman scattering because of its narrow spectral line width. Advanced Raman set ups often contain continuously tunable lasers, based on Ti-doped sapphire (700 nm - 1000 nm),[138] dye molecules (250 nm - 1000 nm from overlapping and frequency doubled ranges for different dye molecules)[139] and most recently optical parametric oscillators (450 nm - 650 nm and 900 nm - 1300 nm).[140] The detection of the Raman-scattered light with tunable lasers is more challenging than for fixed excitation wavelength. The suppression of elastically-scattered light is accomplished with edge filters or triple-grating spectrometers.[124]

Figure 2.13 also shows the optical components that are needed for a full polarization control.[127] I first discuss the set up for linear light polarization, in which a half-wave plate ($\lambda/2$) is placed in front of the microscope objective. The incoming laser light is linearly polarized by a polarizer (P) and rotated by the $\lambda/2$ plate to any polarization direction on the sample. The Raman-scattered light passes back through the $\lambda/2$ plate and is rotated back by the same angle as the incoming light (but opposite direction). The polarization component of the detected Raman-scattered light is chosen with a combination of a $\lambda/2$ plate and an analyzer (A) in front of the spectrometer. The analyzer is fixed to one polarization direction because the spectrometer typically has a polarization-dependent sensitivity. This set up allows for parallel and crossed polarization of the incoming- and Raman-scattered light with any polarization angle on the sample. By placing a quarter-wave plate ($\lambda/4$) in front of the microscope objective in stead of the $\lambda/2$ plate, the sample is characterized with circularly polarized light. If the incident- and Raman-scattered light have the same handedness one speaks of circular-corotating polarization and for opposite handedness of circular-contrarotating polarization. The two polarization configurations are chosen by the orientation of the $\lambda/2$ plate in front of the spectrometer.

2.2.3. Surface-enhanced Raman scattering

As described in the previous section, a Raman scattering process corresponds to second- or third-order perturbation theory and is therefore an intrinsically weak effect. Surface-enhanced Raman scattering (SERS) is a popular technique for increasing the sensitivity of Raman spectroscopy.[6,30,31] It is based on the giant increase in the Raman polarisability

of a molecule close to a rough metal surface or a metallic nanostructure.[6,30,32,141] The major underlying enhancement mechanism is the excitation of localized surface plasmon resonances, which generate intense electromagnetic near fields driving the Raman process (Section 2.1.3).[6,32] Furthermore, the SERS intensity is affected by interactions of the molecule with the metal surface which is often referred to as chemical enhancement.[142,143] The enhancement can be strong enough to detect the Raman spectrum of a single molecule, making SERS an important tool for analytical chemistry.[31,33,34] In the following, I will briefly introduce the different enhancement mechanisms and discuss some experimental and theoretical challenges.

When placing a molecule or nanomaterial inside a plasmonic hotspot at position $\mathbf{r}_0$, the Raman dipole

$$\mathbf{p}_\mathrm{R}(\mathbf{r}_0,\omega_\mathrm{S}) = \overleftrightarrow{\alpha}_\mathrm{R}(\omega_\mathrm{L},\omega_\mathrm{S})\left[\mathbf{E}_\mathrm{inc}(\mathbf{r}_0,\omega_\mathrm{L}) + \mathbf{E}_\mathrm{pl}(\mathbf{r}_0,\omega_\mathrm{L})\right] \tag{2.16}$$

is not only induced by the incident light field $\mathbf{E}_\mathrm{inc}$, but also by the plasmonic near field $\mathbf{E}_\mathrm{pl}$.[1,6,32] The plasmonic near field enhances the Raman dipole by a factor $f_\mathrm{in} = 1 + E_\mathrm{pl}(\mathbf{r}_0,\omega_\mathrm{L})/E_\mathrm{inc}(\mathbf{r}_0,\omega_\mathrm{L})$, under the assumption that the plasmonic near field and the incident field are parallel. The field that is radiated by the Raman dipole to a detector at position $\mathbf{r}_\infty$

$$\mathbf{E}(\mathbf{r}_\infty,\omega_\mathrm{S}) = \frac{\omega_\mathrm{S}^2}{\epsilon_0 c^2}\overleftrightarrow{G}(\mathbf{r}_\infty,\mathbf{r}_0)\mathbf{p}_\mathrm{R}(\mathbf{r}_0,\omega_\mathrm{S}) \tag{2.17}$$

is calculated with the Green function of the overall system $\overleftrightarrow{G}(\mathbf{r}_\infty,\mathbf{r}_0)$.[1] The Green function can be split into a part that describes the direct radiation of Raman-scattered light into free space $\overleftrightarrow{G}_0(\mathbf{r}_\infty,\mathbf{r}_0)$ and a second part that describes the emission of the Raman-scattered light via the plasmonic nanostructure $\overleftrightarrow{G}_\mathrm{pl}(\mathbf{r}_\infty,\mathbf{r}_0) \approx E_\mathrm{pl}(\mathbf{r}_0,\omega_\mathrm{S})/E_\mathrm{inc}(\mathbf{r}_0,\omega_\mathrm{S})\overleftrightarrow{G}_0(\mathbf{r}_\infty,\mathbf{r}_0)$. By combining Eqs. (2.17) and (2.16), the intensity of the Raman-scattered light is[1]

$$I_\mathrm{SERS} = \frac{\omega_\mathrm{S}^4}{\epsilon_0^2 c^4}\left|\left(1+\frac{E_\mathrm{pl}(\mathbf{r}_0,\omega_\mathrm{S})}{E_\mathrm{inc}(\mathbf{r}_0,\omega_\mathrm{S})}\right)\overleftrightarrow{G}_0(\mathbf{r}_\infty,\mathbf{r}_0)\overleftrightarrow{\alpha}_\mathrm{R}(\omega_\mathrm{L},\omega_\mathrm{S})\mathbf{E}_\mathrm{inc}(\mathbf{r}_0,\omega_\mathrm{L})\left(1+\frac{E_\mathrm{pl}(\mathbf{r}_0,\omega_\mathrm{L})}{E_\mathrm{inc}(\mathbf{r}_0,\omega_\mathrm{L})}\right)\right|^2. \tag{2.18}$$

It differs from the Raman intensity without a plasmonic nanostructure by the two factors $f_\mathrm{in} = 1 + E_\mathrm{pl}(\mathbf{r}_0,\omega_\mathrm{L})/E_\mathrm{inc}(\mathbf{r}_0,\omega_\mathrm{L})$ and $f_\mathrm{out} = 1 + E_\mathrm{pl}(\mathbf{r}_0,\omega_\mathrm{S})/E_\mathrm{inc}(\mathbf{r}_0,\omega_\mathrm{S})$ that constitute the electromagnetic enhancement factor

$$\mathrm{EF}_\mathrm{em} = \left|\left(1+\frac{E_\mathrm{pl}(\mathbf{r}_0,\omega_\mathrm{L})}{E_\mathrm{inc}(\mathbf{r}_0,\omega_\mathrm{L})}\right)\left(1+\frac{E_\mathrm{pl}(\mathbf{r}_0,\omega_\mathrm{S})}{E_\mathrm{inc}(\mathbf{r}_0,\omega_\mathrm{S})}\right)\right|^2 \tag{2.19}$$

of the SERS intensity.[1,6,32] When neglecting the Raman shift, the SERS intensity scales

with $(E_{\mathrm{pl}}/E_{\mathrm{inc}})^4$ which is known as the E^4-enhancement approximation. The local field enhancement $E_{\mathrm{pl}}(\mathbf{r},\omega)/E_{\mathrm{inc}}(\mathbf{r},\omega)$ can be calculated analytically or numerically for almost any plasmonic nanostructure (see Section 2.1.4) making the electromagnetic enhancement theory a powerful tool for the design of SERS substrates with large enhancement.[32] The electromagnetic enhancement can exceed ten orders of magnitude in the hotspot of a plasmonic nanostructure;[6] see e.g. the field enhancement from the gold nanoparticle dimer with 2 nm gap in Fig. 2.5a. A drawback of the electromagnetic enhancement factor in Eq. (2.19) is that it does not provide insight into the intermediate steps of a SERS process, which is key for studying the dependence of the SERS signal on excitation energy. This was a key reason why I developed the description of SERS within the microscopic theory of Raman scattering in my thesis.

Chemical enhancement encompasses a number of effects that concern the interaction of a molecule with a metal surface and molecule-molecule interactions.[142] Metal and molecule may form hybridized- or charge-transfer states that induce new SERS resonances.[142,144–146] The interaction of a molecule with the metal surface may shift its absorption which leads to an increase or decrease of the SERS intensity dependent on the excitation energy.[6,147] Furthermore, the Raman polarizability changes when molecules form aggregates which affects the experimental SERS enhancement factor when the molecules in the reference measurement are in a different state.[129] Except for special cases, chemical enhancement provides less enhancement $(10-10^3)$ than the plasmonic enhancement mechanism.[143,148] Its modeling is a challenge as it typically requires an atomistic description of the metal surface and the molecule with density functional theory (DFT).[142,143] Hybrid electromagnetic-DFT approaches were developed to calculate the plasmonic and chemical enhancement of specific molecules on the surface of a plasmonic nanoparticle.[149] The calculated enhancement factors, however, depend on a large number of parameters which are typically unknown in an experiment.

The major experimental challenge of SERS is to make the effect quantitative.[6,35,36] Even though SERS was discovered more than 40 years ago it is still quite demanding to predict the outcome of a SERS experiment, such as the SERS enhancement and its dependence on excitation energy. The reason is the large number of effects that simultaneously affect the SERS signal; see discussion in the previous paragraphs. Recent experimental work aimed at designing SERS substrates with well defined plasmonic hot spots and molecule positioning, which allows a direct comparison to theory (Fig. 2.14).[29,36,83,151–154] By encapsulating molecules in the nanometer gap between a gold nanoparticle and a flat gold substrate it was demonstrated that mobile atomic scale protrusions of the gold

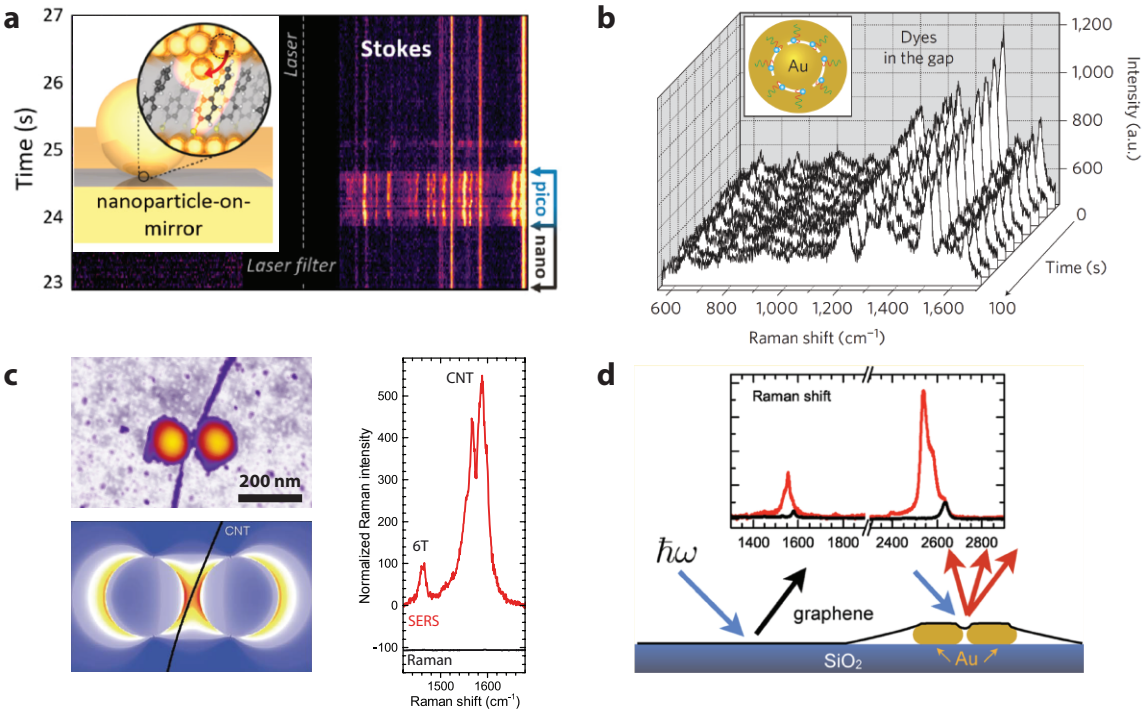

Figure 2.14. Selection of recent SERS experiments with well-defined plasmonic hotspots and positioning of molecules. (a) Molecules inside a nanoparticle-on-mirror cavity. The SERS intensity is affected by the formation of sub-nm cavities which lead to temporal fluctuations of the SERS signal. Figure adapted from Ref. 150. (b) Uniform and reproducible SERS spectra of dye molecules encapsulated inside the nanogaps of special gold nanoparticles using DNA (see inset). Figure adapted from Ref. 36. (c) Isolating the plasmonic enhancement of SERS by encapsulating molecules inside carbon nanotubes. The encapsulated molecules were placed into the hotspot of a gold nanoparticle dimer (left, top) and the SERS enhancement (right) was compared to FDTD simulations (left, bottom). Figure adapted from Ref. 151. (d) Using graphene to read out the plasmonic near field enhancement of a gold nanoparticle dimer. Figure from Ref. 29.

surface strongly affect the SERS signal and lead to time-dependent intensity fluctuations (Fig. 2.14a).[150,153] These intensity fluctuations could be avoided by placing dye molecules at well defined positions inside gold nanobridged nanogap substrates using DNA (Fig. 2.14b).[36] Special SERS substrates were also designed in the Reich group that allowed studying SERS. By placing carbon nanotubes with encapsulated dye molecules into the gap of a gold nanoparticle dimer it was possible to isolate the plasmonic enhancement and draw a direct comparison to theory (Fig. 2.14c).[151,154,155] Furthermore, graphene was used to study the excitation-energy dependence of the SERS enhancement because of its wavelength-independent Raman polarizability (Fig. 2.14d).[29,156] The latter system was

used in this thesis to analyze the nanoscale strain and doping in graphene induced by a gold nanostructure (see Publication P5 of my thesis).

2.3. Graphene

Graphene is a two-dimensional sheet of carbon atoms that are arranged in a honeycomb lattice.[157,158] Discovered in 2004 among the first two-dimensional materials, graphene is a true wonder material in terms of electronic, optical and mechanical properties.[157,159] The charge carriers in graphene mimic the properties of massless relativistic particles, which leads to a record high mobility and ballistic transport over micrometers.[160–163] Even though graphene is atomically thin, it possesses an exceptionally large optical absorption of $\pi\alpha \approx 2.3\%$, where α is the fine-structure constant.[164,165] The lattice is stabilized by sp^2 bonds which make graphene resistant against breaking and leads to the highest stiffness and strength ever recorded.[166,167] The exceptional properties make graphene a promising material for applications such as flexible electronics, optoelectronics, high-frequency transistors, biosensors and energy storage devices.[159] In this thesis I interfaced graphene with plasmonic nanostructures to enhance its optical absorption and to read out nanoscale strain and doping with surface-enhanced Raman scattering (see Publications P3 and P5 of my thesis). In the following, I will introduce the electronic, optical, and vibrational properties of graphene.

2.3.1. Electronic and optical properties

The electronic properties of graphene are best understood by taking a look at its fundamental building block – carbon.[127,158] The hybridization of one 2s orbital with two 2p orbitals into three sp^2 orbitals leads to the arrangement of carbon atoms into a two-dimensional honeycomb lattice, called graphene (see Fig. 2.15a).[158] The lattice is stabilized by covalent σ bonds that arise from the spatial overlap of sp^2 orbitals from neighboring carbon atoms. This makes graphene one of the strongest materials on earth, having a breaking strength of 42 N/m and an in-plane stiffness of up to 300 N/m.[166,168] In addition to the sp^2 orbitals, one p orbital remains per carbon atom and points perpendicular to the graphene lattice. The overlap with neighboring p orbitals leads to the formation of bonding π and antibonding π^* orbitals that constitute the valence and conduction band of graphene (Fig. 2.15b, c).[127,158,169]

The electronic band structure of graphene is described exceptionally well with a tight-binding model.[169,171] Figure 2.15b shows a comparison of graphene's band structure from ab-initio calculations (black solid lines) and a tight-binding model (red dashed lines).[170,171] Interactions up to third-nearest neighbors must be included in order to reproduce the

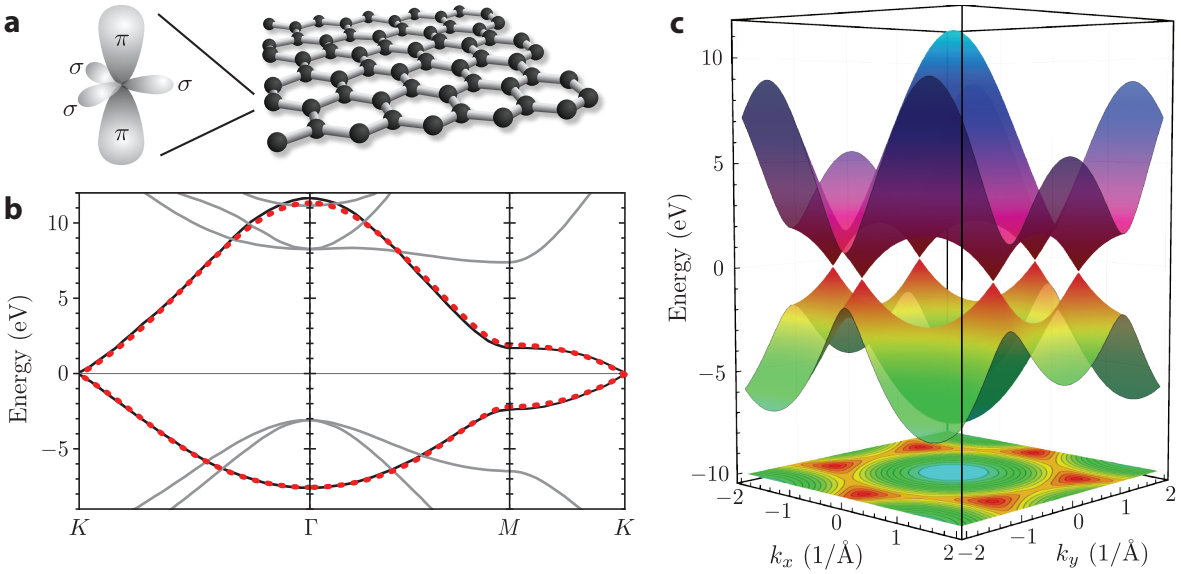

Figure 2.15. Electronic properties of graphene. (a) Graphene lattice (right) and carbon valence orbitals (left). The σ orbitals form strong covalent bonds between the carbon atoms; the π orbitals are delocalized over the graphene lattice and are responsible for graphene's electronic and optical properties. (b) Electronic band structure of graphene from ab-initio calculations of Lherbier et al.[170] (black solid lines for valence and conduction band; gray solid lines for bands from σ orbitals). The red dotted lines are a fit with a tight-binding model from Reich et al.[171] including up to third-nearest neighbors. (c) Valence and conduction band of graphene calculated with the same tight-binding model as in (b). The two bands touch at the six K points in the shape of cones. A contour plot of the valence band is shown below the three-dimensional band structure.

ab-initio band structure.[171] Details on the implementation of the band structure and electronic wave functions with the tight-binding model are provided in Publication 3 of my thesis. The electronic and optical properties of graphene are determined by the valence and conduction band, touching in the shape of cones at the six K points of the Brillouin zone (Fig. 2.15 c). Graphene is therefore a semimetal, with the Fermi level at the crossing points of the bands for zero doping. A saddle point close to the M point gives rise to excitonic properties of graphene in the UV.[172] The σ bands are strongly separated in energy ($\sim$12 eV at the Γ point) and their contribution to the electronic and optical properties are negligible.

Most of graphene's fascinating properties arise from its unusual band structure close to

the K points.[160,173] The electronic dispersion

$$E(\mathbf{k}) \approx \pm\hbar v_{\mathrm{F}}|\mathbf{k}| \tag{2.20}$$

is approximated as a linear function of wave vector $\mathbf{k}$; where $\mathbf{k}$ is the vector to the K point in phase space. The slope is given by the electronic group velocity $v_{\mathrm{F}} \approx 8.5 \cdot 10^5$ m/s, called Fermi velocity.[158] Within the linear-band approximation, the charge carriers in graphene are described by the Hamiltonian[158,174]

$$\mathcal{H} = v_{\mathrm{F}}\boldsymbol{\sigma} \cdot \mathbf{p} \tag{2.21}$$

where $\boldsymbol{\sigma} = (\sigma_x \quad \sigma_y)$ is a vector that contains the Pauli matrices

$$\sigma_x = \begin{pmatrix} 0 & 1 \\ 1 & 0 \end{pmatrix}, \quad \sigma_y = \begin{pmatrix} 0 & -\mathrm{i} \\ \mathrm{i} & 0 \end{pmatrix}, \tag{2.22}$$

and $\mathbf{p} = -\mathrm{i}\hbar\nabla$ is the momentum operator. The Hamiltonian is formally equivalent with the Dirac-Weyl Hamiltonian for particles with zero rest mass, such as neutrinos.[158,174] The charge carriers in graphene are therefore regarded as *massless Dirac fermions* moving at the speed $v_{\mathrm{F}} \approx c/300$, where c is the velocity of light in vacuum.[160,173] This explains graphene's record-high carrier mobility of $200,000$ $\mathrm{cm^2V^{-1}s^{-1}}$ which enables ballistic transport over several micrometers.[161–163] As the unit cell of the graphene lattice consists of two atoms, the Brillouin zone contains two inequivalent K points. The Pauli matrices in Eq. (2.21) do not act on the electron spin, but on the electrons in the two sublattices, which is called *valley pseudospin*.[175,176]

One striking consequence of graphene's linear band structure is a constant optical absorption of $P_{\mathrm{abs}} = \pi\alpha \approx 2.3\%$ across the entire infrared and visible spectral range (Fig. 2.16a), where $\alpha = e^2/(4\pi\epsilon_0 c\hbar)$ is the fine structure constant.[164,165] The optical absorption increases slightly when approaching the UV spectral range because of deviations from the linear energy dispersion, called trigonal warping, and the excitation of a saddle-point exciton at 4.5 eV.[172] The absorption increases step-wise by 2.3% with additional graphene layers such that the opacity of a graphene sheet may be used to count the number of layers (Fig. 2.16a).[164] The constant optical absorption of $\pi\alpha$ is derived from the tight-binding description of graphene's electronic states.[164,177,178] I will outline the basic steps in the following paragraph.

The time-averaged energy of an incident light field with frequency ω that is absorbed

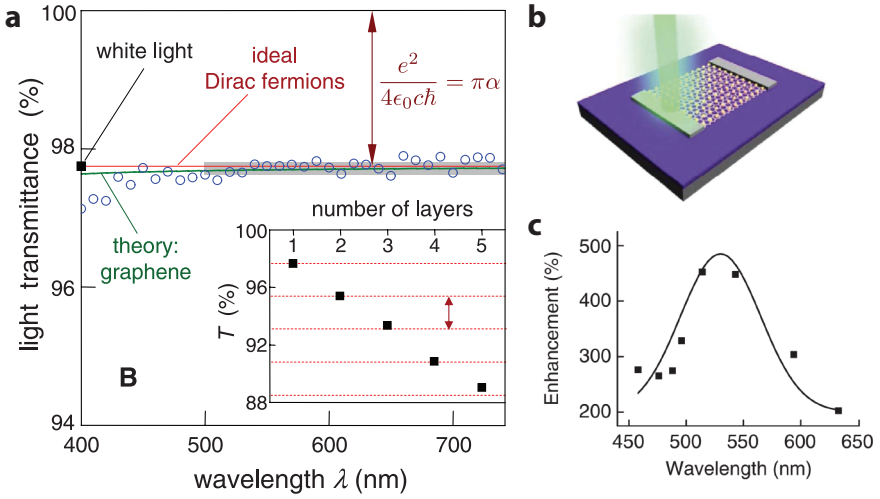

Figure 2.16. Optical absorption of graphene and its enhancement by plasmonic nanostructures. (a) Light transmittance through a monolayer of graphene. Blue circles show measured data, the red line the calculated transmittance from an absorbance of $\pi\alpha = 2.3\%$ and zero reflectance, and the green line the calculated transmittance from a full tight-binding calculation. The inset shows the transmittance of white light for up to five layers. Figure adapted from Ref. 164. (b) Sketch of a graphene-based photodetector in which the photocurrent is enhanced by a lattice of plasmonic nanoparticles, and (c) photocurrent enhancement as a function of excitation wavelength. Figures (b) and (c) from Ref. 179.

by graphene is $W_{\text{abs}} = \langle\eta\rangle\hbar\omega$. It contains the averaged transition rate

$$\langle\eta\rangle = g_{\text{v}} g_{\text{s}} \int \frac{d^2\mathbf{k}}{(2\pi)^2}\eta(\mathbf{k}) \tag{2.23}$$

that is calculated with the Fermi Golden rule

$$\eta(\mathbf{k}) = \frac{2\pi}{\hbar}|\mathcal{M}_{\text{el-pt}}(\mathbf{k})|^2\delta(2\hbar v_{\text{F}}|\mathbf{k}| - \hbar\omega) \tag{2.24}$$

by integration over all wave vectors $\mathbf{k}$ around the K point. $g_{\text{v}} = 2$ is the valley degeneracy and $g_{\text{s}} = 2$ the spin degeneracy. The matrix element $\mathcal{M}_{\text{el-pt}}(\mathbf{k}) = \langle\mathbf{k}\pi^*|\mathcal{H}_{\text{el-pt}}|\mathbf{k}\pi\rangle$ is calculated with the interaction Hamiltonian $\mathcal{H}_{\text{el-pt}} = \mathrm{i}ev_{\text{F}}/(2\omega)\boldsymbol{\sigma}\cdot\mathbf{E}_{\text{pt}}$ that is obtained from Eq. (2.21) with the Peierl's substitution $\mathbf{p} \to \mathbf{p} + \mathrm{i}e/(2\omega)\mathbf{E}_{\text{pt}}$. $\mathbf{E}_{\text{pt}}$ is the electric field amplitude of the incident light field. Using the tight-binding wave functions (see

Publication P3 of my thesis for details)

$$|\mathbf{k}\pi\rangle = \frac{1}{\sqrt{2}} \begin{pmatrix} 1 \\ -\frac{k_x+\mathrm{i}k_y}{|\mathbf{k}|} \end{pmatrix}, \quad |\mathbf{k}\pi^*\rangle = \frac{1}{\sqrt{2}} \begin{pmatrix} 1 \\ \frac{k_x+\mathrm{i}k_y}{|\mathbf{k}|} \end{pmatrix} \tag{2.25}$$

the averaged transition rate is $\langle\eta\rangle = e^2 E_{\mathrm{pt}}^2/(8\hbar^2\omega)$. The optical absorption of graphene is obtained by dividing W_{abs} by the time-averaged energy flux of the incident light field $W_{\mathrm{inc}} = \epsilon_0 c E_{\mathrm{pt}}^2/2$, which results in

$$P_{\mathrm{abs}} = \frac{W_{\mathrm{abs}}}{W_{\mathrm{inc}}} = \frac{e^2}{4\epsilon_0 c\hbar} = \pi\alpha. \tag{2.26}$$

An optical absorption of 2.3% appears large for a monolayer of atoms, but is too small for efficient photodetection. A promising route to enhance the photocurrent in graphene-based optoelectronic devices is the combination with plasmonic nanostructures.[24] Several layouts of hybrid photodetectors have been proposed in which graphene was interfaced with lattices of plasmonic nanoparticles (Fig. 2.16b).[179–181] The photocurrent was enhanced by the localized surface plasmon of the metallic nanoparticles (Fig. 2.16c) and exceeded an order of magnitude for specific designs. A detailed understanding of the photocurrent generation remained, however, missing because of the various underlying enhancement mechanisms.[25–28] This motivated me to develop a microscopic theory for the enhancement of graphene's optical absorption by the optical near field of a plasmonic nanoparticle lattice (see Publication P3 of my thesis).

2.3.2. Vibrational properties

Raman spectroscopy is a powerful tool for characterizing the properties of graphene, such as strain, doping, defects, and the number of layers.[182,183] This is possible because graphene's Raman peaks arise from an exceptionally strong interplay of the electronic and vibrational states. As the unit cell consists of two atoms, the phonon band structure contains three transverse (T) and three longitudinal (L) branches, of which four are in-plane vibrations (i) and two are out-of-plane vibrations (o) (Fig. 2.17a).[127,182,184] The phonons are further categorized as optic (O) when the two atoms of the unit cell vibrate against each other and otherwise as acoustic (A). As the momentum of a photon is small compared to the extension of the Brillouin zone, Raman scattering typically probes optical phonons close to the Γ point.[124]

The Raman spectrum of graphene is shown in Figure 2.17b. It contains two prominent

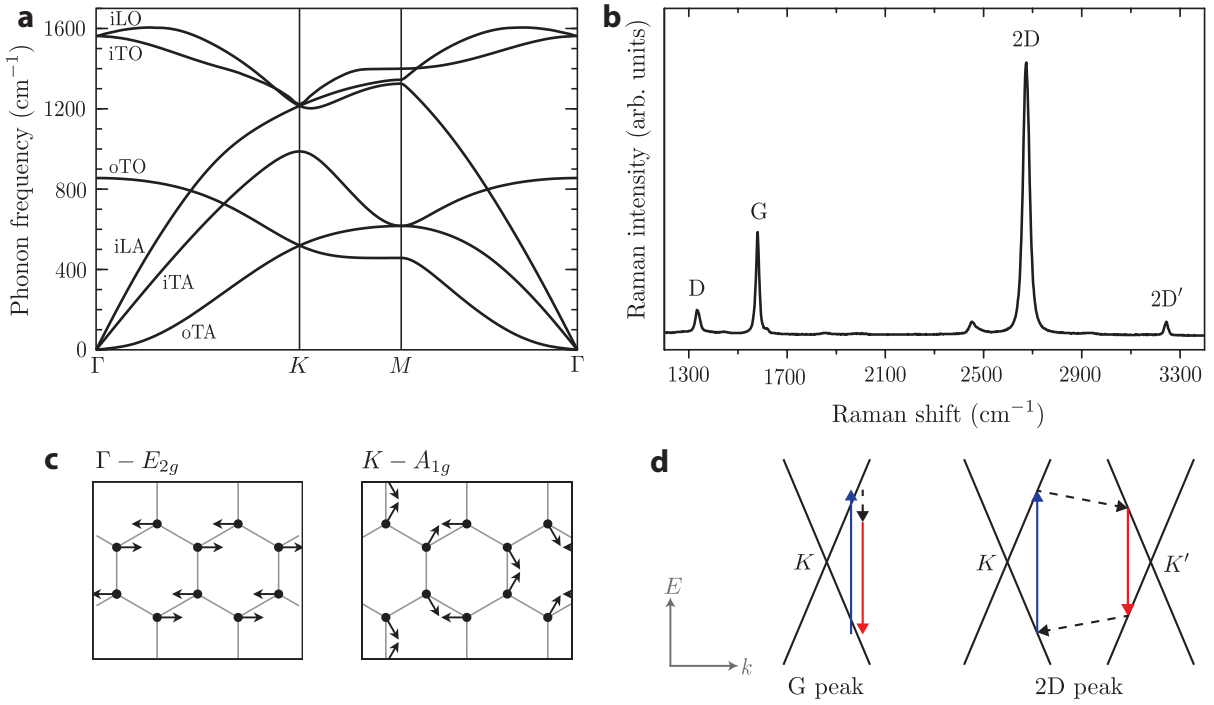

Figure 2.17. Vibrational properties of graphene. (a) Phonon band structure of graphene from DFT calculations with *GW* correction, containing three acoustic (A) and three optical (O) branches. The branches furthermore belong to transverse (T) or longitudinal (L) phonons that are either in-plane (i) or out-of-plane (o). Figure adapted from Ref. 185 with terminology from Ref. 182. (b) Experimental Raman spectrum of graphene adapted from Ref. 186. (c) Lattice vibrations associated with the G mode ($\Gamma - E_{2g}$) and the 2D mode ($\Gamma - A_{1g}$). Figure adapted from Ref. 184. (d) Intermediate steps of the Raman scattering processes of the G mode (left) and the 2D mode (right) depicted in the linear energy dispersion of graphene close to the K points. The Raman processes involve two electronic transitions (blue and red arrows) and the excitation of phonons (black dashed arrows).

Raman modes called G and 2D.[187] The G peak is the only Raman mode of graphene that arises from a first-order Raman process. It probes the degenerate iLO and iTO phonons close to the Γ point, Fig. 2.17a, that correspond to a lattice vibration with E_{2g} symmetry (Fig. 2.17c).[182,184,188] The intermediate steps of the Raman process are shown in Fig. 2.17d, left. Besides the depicted resonant Raman process, off-resonant Raman processes across the entire Brillouin zone contribute equally to the G mode intensity.[189,190] The reason is destructive interference of Raman processes with opposite wave vector, which leads to a complete disappearance of the calculated G mode when using the linear band approximation.

The 2D mode stems from a second-order Raman process that involves two iTO phonons close to the K point with $A_{1g} \oplus E_{2g}$ symmetry (Fig. 2.17a).[182,185,191] The A_{1g} vibrations at the K point are shown in Fig. 2.17c, right.[184] The large intensity of the 2D mode is explained by a double resonant Raman process that is depicted in the band structure of graphene in Fig. 2.17d, right.[191,192] It involves resonant scattering processes between two valleys by two phonons with same magnitude but opposite wave vector (dashed arrows). As different phonons are required when changing the excitation energy the 2D mode is dispersive, shifting with ≈ 100 cm^{-1}/eV.[191] The Raman spectrum of graphene contains additional peaks from second-order Raman processes. The D mode arises from a similar Raman process as the 2D mode, involving the scattering by one defect and one phonon instead of two phonons.[185,191] It is thus used to measure the amount of defects in graphene.[193,194] The 2D' mode probes iLO phonons close to the Γ point based on a similar scattering processes as the 2D mode.[185,195]

The Raman modes of graphene are sensitive to charge doping.[196,199] The G mode shifts significantly ($\approx 15\,\mathrm{cm}^{-1}$ per $10^{13}\,\mathrm{cm}^{-2}$ electron concentration) to larger wavenumbers upon electron, and hole doping (Fig. 2.18a).[196,199] The reason is a Kohn anomaly (kink with linear dispersion) of the optical phonons at the Γ and K points in the phonon band structure (see Fig. 2.17a).[200] This anomaly disappears upon doping because of a break down of the adiabatic Born-Oppenheimer approximation.[201,202] The G mode furthermode narrows spectrally because of a suppression of electron-phonon relaxation by Pauli blocking.[201] The 2D mode also shifts to larger wavenumbers for hole doping, but remains constant for electron doping below $\approx 2 \cdot 10^{13}\,\mathrm{cm}^{-2}$ followed by a nonlinear down shift for larger doping levels.[196,199] This occurs because of a combination of adiabatic and non-adiabatic effects.[196]

Besides doping, the vibrational frequencies are shifted and split by strain and the Raman intensities depend on the polarization of the incoming and detected light.[197,198,203] Any in-plane strain configuration can be decomposed into a hydrostatic and a shear component.[198,204] Hydrostatic strain leads to a downshift for tensile strain and upshift for compressive strain by 28 cm^{-1}/% for the G mode, which was measured in an experiment with graphene bubbles (Fig. 2.18b).[197] Similarly the 2D mode is shifted by ≈ 65 cm^{-1}/%.[197,205] Shear strain leads to a splitting of the Raman modes by 20 cm^{-1}/% for the G mode, whereas reliable values for the 2D mode remain a matter of debate (Fig. 2.18c).[198,203,206,207] A more detailed introduction to the effect of strain on graphene's Raman spectrum is provided in Publication P4 of my thesis.

As strain and doping occur simultaneously in an experiment and are typically unknown,

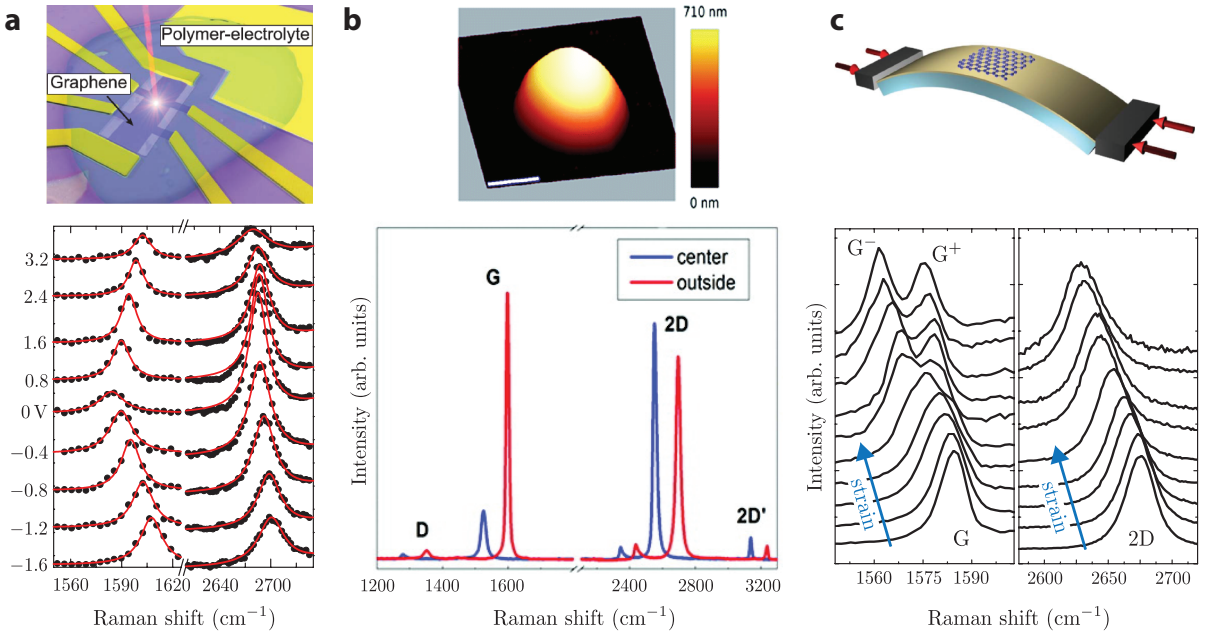

Figure 2.18. Raman spectrum of graphene in the presence of strain and doping. (a) Effect of charge doping on the Raman spectrum of graphene (bottom) using a polymer-electrolyte top gate (top). The applied gate voltage is given next to the Raman spectra; positive voltages correspond to electron doping and negative voltages to hole doping. Figure adapted from Ref. 196. (b) Raman spectrum measured in the center (bottom, blue) and outside (bottom, red) of a pressurized graphene bubble which is shown by an AFM image (top). The graphene bubble induces tensile hydrostatic strain in the graphene lattice. Figure adapted from Ref. 197. (c) Effect of uniaxial strain on the Raman G mode (bottom, left) and 2D mode (bottom, right) induced by bending a PMMA beam as flexible substrate (top). A splitting of the 2D mode is not visible as the Raman spectra were recorded with linearly polarized light. Figure adapted from Ref. 198.

it is a challenge to separate their contributions to the measured peak positions. Lee et al. suggested a correlation analysis of the G and 2D mode frequencies to separate the peak shifts by strain and doping.[208] The analysis, however, required prior knowledge of the strain configuration. This motivated me to develop a methodology for the evaluation of strain and doping in graphene that does not require any assumption on the type of strain as input parameter; see Publication P4 of my thesis.

3 | Papers forming this thesis

P1. **Dark Interlayer Plasmons in Colloidal Gold Nanoparticle Bi- and Few-Layers**,
Niclas S. Mueller*, Bruno G. M. Vieira*, Florian Schulz, Patryk Kusch, Valerio Oddone, Eduardo B. Barros, Holger Lange, and Stephanie Reich,
ACS Photonics 5, 3962-3969 (2018)
(Shared first authorship with Bruno G. M. Vieira)
I performed all optical measurements and the simulations for the nanoparticle dimer, interpreted the data and wrote the manuscript. B. G. M. Vieira performed all simulations for the layered nanostructure with support from me. F. Schulz and H. Lange prepared the nanostructures. F. Schulz performed the TEM measurements together with me. P. Kusch and V. Oddone helped me to set up the optical spectrometer for micro-absorbance measurements. E. B. Barros gave intellectual input and partly supervised B. G. M. Vieira. The project was conceived by S. Reich and me. All coauthors discussed the data and commented on the manuscript.

P2. **Direct optical excitation of dark plasmons for hot electron generation**,
Niclas S. Mueller, Bruno G. M. Vieira, Dominik Höing, Florian Schulz, Eduardo B. Barros, Holger Lange, and Stephanie Reich,
Faraday Discussions 214, 159 (2019)
I recorded all micro-reflectance and absorbance spectra and evaluated the data. The FDTD simulations were conducted by me with input from B. G. M. Vieira. Time-resolved transient-absorption measurements were conducted by D. Höing under the supervision of H. Lange. F. Schulz prepared the nanostructures and characterized them with TEM. S. Reich derived the optical selection rules for dark interlayer modes. E. B. Barros gave intellectual input and partly supervised B. G. M. Vieira. S. Reich and I conceived the project and wrote the manuscript. All coauthors discussed the data and commented on the manuscript.

P3. **Microscopic theory of optical absorption in graphene enhanced by lattices of plasmonic nanoparticles**,
Niclas S. Mueller and Stephanie Reich,
Physical Review B 97, 235417 (2018)
I performed all analytical derivations and calculations and wrote the manuscript. S. Reich helped developing the theory, commented on the manuscript and supervised the project.

P4. **Surface-enhanced Raman scattering as a higher-order Raman process**,
Niclas S. Mueller, Sebastian Heeg, and Stephanie Reich,
Physical Review A 94, 023813 (2016)
I performed all analytical derivations and calculations and wrote the manuscript. The general framework of the theory was conceived by S. Reich, S. Heeg and me. All authors discussed the derived expressions and calculations and commented on the manuscript.

P5. **Evaluating arbitrary strain configurations and doping in graphene with Raman spectroscopy**,
Niclas S. Mueller, Sebastian Heeg, Miriam Peña Alvarez, Patryk Kusch, Sören Wasserroth, Nick Clark, Fredrik Schedin, John Parthenios, Konstantinos Papagelis, Costas Galiotis, Martin Kalbáč, Aravind Vijayaraghavan, Uwe Huebner, Roman Gorbachev, Otakar Frank, and Stephanie Reich,
2D Materials 5, 015016 (2018)
I performed all Raman and AFM measurements, interpreted the data and wrote the manuscript. The samples for uniaxially strained graphene were prepared by M. P. Alvarez, M. Kalbáč and O. Frank. The samples consisting of graphene deposited on gold nanostructures were prepared by S. Heeg, N. Clark, F. Schedin, A. Vijayaraghavan, U. Huebner and R. Gorbachev. S. Wasserroth, P. Kusch and S. Heeg performed a pre-characterization of these samples. O. Frank, J. Parthenios, K. Papagelis and C. Galiotis gave intellectual input on the interpretation of Raman spectra recorded with circularly polarized light. The project was conceived by S. Reich and me. All authors discussed the data and commented on the manuscript.

4 | Connection of the papers

The publications forming this thesis improved the understanding of optical processes that are mediated by localized surface plasmons; see Fig. 4.1. The considered optical processes include the optical absorption by the plasmon (P1) and its decay into hot electrons for photocatalytic applications (P2). Moreover, the two fundamental processes of plasmon-enhanced optical absorption (P3) and Raman scattering (P4-P5) in nearby materials are investigated. I approached these topics from an experimental and a theory side, with experiments (P1, P2 and P5), simulations (P1 and P2) and analytical theory (P3 and P4). In the following I will describe the scientific projects associated with the publications forming this thesis and their connection.

As outlined in the introduction of this thesis, plasmonic excitations are categorized into *bright* and *dark* depending on their net dipole moment.[15,16] While bright plasmons are excited by light, dark plasmons are usually inaccessible to far field radiation. Dark plasmons are of great interest for energy and sensing applications as the suppressed radiative damping increases the plasmon lifetime and narrows plasmon resonances.[11,18] In the last decade various approaches have been proposed for the optical excitation of dark plasmons.[16–19,51,72–82] As discussed in the introduction of P1, existing approaches require either specific light sources for excitation or the fabrication of complex nanostructures with lithographic techniques. This is a great challenge for large-scale catalytic and photovoltaic applications.

In P1 we proposed a new approach for dark plasmon excitation that is easy to implement and scalable. Based on earlier work with gold nanodimers in the Reich group,[29,151,154,209] we suggested to excite a dark plasmon by illuminating a nanodimer from the side, i.e., along the dimer axis (see Fig. 4.2a). Because of field retardation of the incident light, a dark plasmon with antiparallel dipoles should be directly excited in this configuration. I confirmed this idea by simulating the optical response of a gold nanodimer with the finite-difference time-domain method. A new absorption peak appeared in the optical

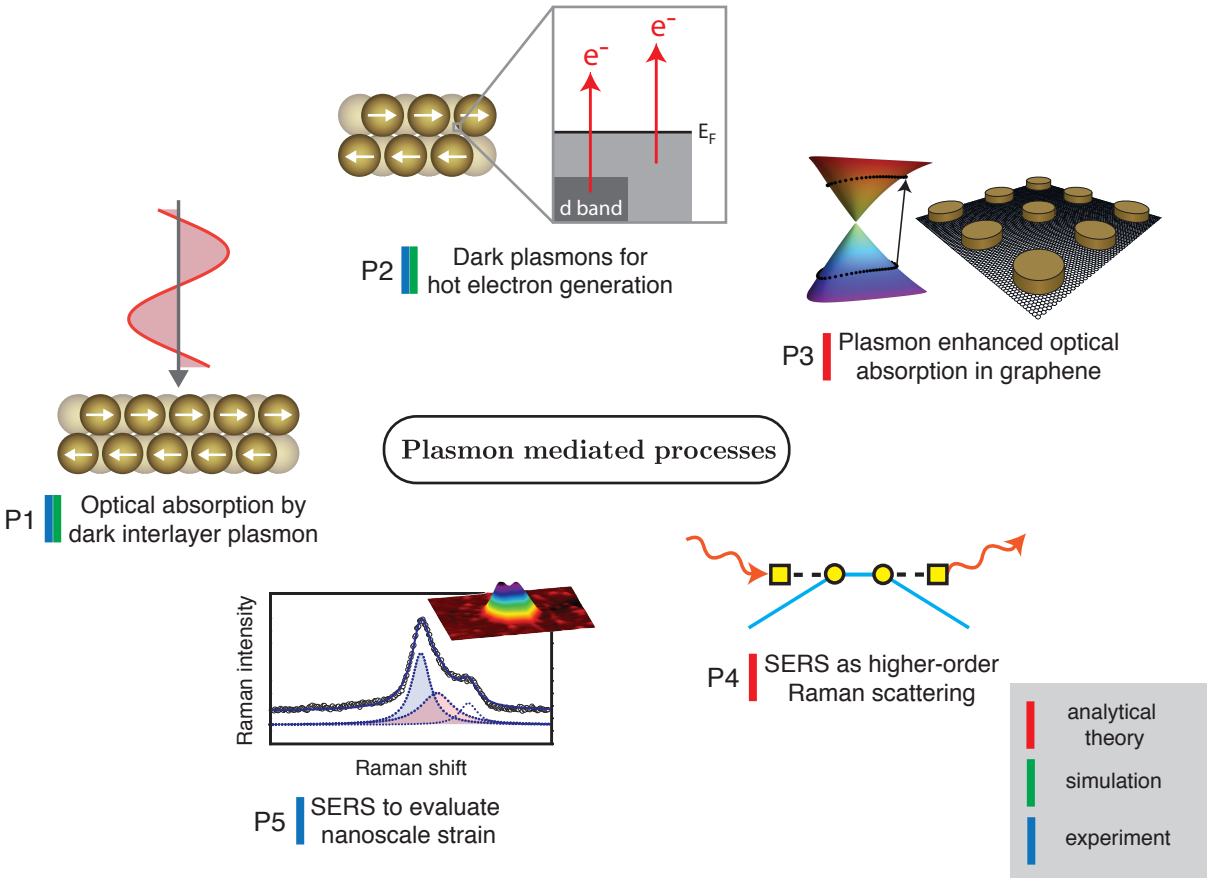

Figure 4.1. Connection of the publications forming this thesis (P1-P5). They study plasmon-mediated optical processes and contain experiments (blue), simulations (green), and analytical theory (red). Figures adapted from Publications P1-P5 of this thesis.

spectrum when illuminating the dimer along its axis which was clearly assigned to the dark plasmon from its energetic position and spectral width. An experimental realization of this geometry, on the other hand, appeared to be challenging because it required incident light along a substrate surface or stacking two nanoparticles on top of each other. This brought us to the idea to use bilayers of close-packed gold nanoparticles instead of individual dimers (Fig. 4.2b). For this nanostructure we expected a direct excitation of the dark plasmon by illumination from the top; an experimental realization of dark plasmon excitation was within reach.

The fabrication of close-packed gold nanoparticle layers is the focus of several chemistry groups that have the aim to develop scalable synthesis protocols for metamaterials and surface-enhanced spectroscopy substrates.[89,210–212] Our idea to excite dark plasmons in such nanostructures required particle diameters that were sufficiently large for the retardation

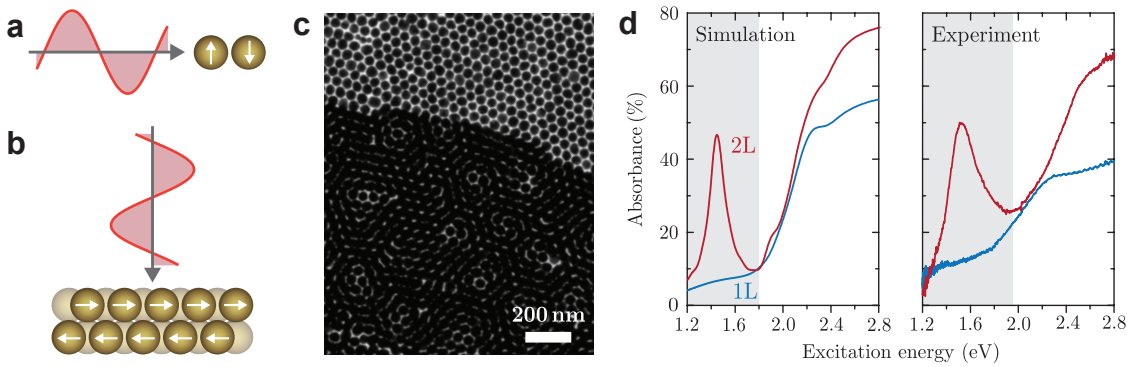

Figure 4.2. Summary of P1 - Dark interlayer plasmons in colloidal gold nanoparticle bi- and few-layers. (a) Idea to excite a dark plasmon (white arrows) in a gold nanoparticle dimer by illumination (red) along the dimer axis. The dark plasmon is excited because of the field retardation of the incident light. (b) Concept for experimental realization of the dark mode excitation by stacking two close-packed gold nanoparticle layers on top of each other and illumation from the top. (c) TEM image of self-assembled monolayer (top) and bilayer (bottom) of 46 nm gold nanoparticles. (d) Finite-difference time-domain simulation (left) and measurement (right) of the absorbance spectra of a monolayer (blue) and bilayer (red) of 46 nm gold nanoparticles with 2 nm gaps. The excitation of the dark plasmon is visible as a pronounced absorbance peak at 1.5 eV in the spectra of the bilayer (2L, red) and absent for a monolayer (1L, blue). Figures adapted from Publication P1 of this thesis.

of the incident light field to become important. Florian Schulz, from the Lange group at the University of Hamburg, recently developed synthesis protocols for particle diameters up to 50 nm.[89] He supplied self-assembled layered nanostructures for this project (Fig. 4.2c). The nanoparticle layers were deposited on TEM grids for structural characterization. To excite and detect dark plasmons at selected areas of the samples, I constructed a micro-absorbance spectrometer with a measurement spot size below 1 μm^2. This set up enabled me to measure optical spectra on selected areas and correlate them with the detailed structural information from TEM.

The optical absorbance spectrum of a gold nanoparticle bilayer contained a pronounced peak at $\sim$ 1.5 eV that was absent for a monolayer (Fig. 4.2d, right). For the interpretation of these spectra we used the nanoparticle arrangement, diameter and gap sizes obtained from TEM as input for FDTD simulations. The simulated spectra were in excellent agreement with experiment (Fig. 4.2d, left). The absorbance peak of the nanoparticle bilayer was assigned to the dark plasmon in Fig. 4.2b by the simulated electric fields inside the gold nanoparticles. From the simulations we obtained a plasmon lifetime of 7 fs, which was three times longer than the lifetime of a bright plasmon in the same nanostructure.

The strong red shift of 0.8 eV of the dark mode compared to the plasmon resonance of a single gold nanosphere (2.3 eV) pointed towards a strong coupling between the plasmonic dipoles in the two layers. From simulations we found that a change in interparticle gap sizes of 0.5 nm already shifted the absorbance peak by 70 meV. We therefore explained the increased spectral linewidth of the dark plasmon peak in the experiments by an inhomogeneous broadening from variations in the gap sizes on a length scale smaller than the laser spot.

After the concept of dark plasmon excitation by field retardation turned out to be successful for a nanoparticle bilayer, we investigated the optical properties of nanoparticle films with more layers. From experiments and simulations we found that with each additional layer a new dark plasmon with vanishing net dipole was activated. The additional dark plasmon in a trilayer had a simulated plasmon life time of 16 fs, which is close to the limit imposed by the internal losses in gold. A spectral narrowing compared to the dark plasmon of a bilayer was clearly visible in the experimental spectra. Based on simulations we predicted the excitation of $n-1$ dark plasmons in a film of n nanoparticle layers. Some of these modes adopted photonic character with increasing layer number and transmitted almost perfectly the light through the nanoparticle film.

Overall we succeeded in exciting dark plasmons in self-assembled layers of gold nanoparticles. The advantages of this new approach become apparent when comparing with other methods for dark plasmon excitation. Our approach exploits the retardation of the incident light field; the dark plasmon is directly excited by linearly-polarized light at normal incidence. This is a huge advantage compared to other approaches that require complex polarization patterns of the incident light or coupling to local emitters.[16,19,72] Furthermore, the nanoparticle layers can be synthesized by wet chemistry, which is a low-cost and scalable production method. There is no need for lithographic techniques, which are required for many nanostructure designs that were suggested to activate dark plasmons. The resonance energy of the dark plasmons can be tuned by changing the interparticle gaps or the layer number. This offers a route for the large-scale exploitation of dark plasmons with tailored properties for spectroscopy and energy applications. The concept and proof of principle results were published in the first paper forming this thesis, Mueller et al., *Dark Interlayer Plasmons in Colloidal Gold Nanoparticle Bi- and Few-Layers*, ACS Photonics 5, 3962-3969 (2018).

The increased lifetime and narrow spectral width make dark plasmons interesting for a number of applications, such as refractive index sensing and nanoscale waveguiding.[11,18]

Because of the inhibition of radiative losses, dark plasmons store energy on the nanoscale more efficiently than bright plasmons.[72] This energy can be exploited in the form of electromagnetic hotspots to enhance light absorption and scattering in nearby materials[24,31] (see P3-P5) or transform into excited uncorrelated electron-hole pairs.[20] Such hot carriers may be used to induce photocatalytic reactions on the surface of the nanoparticles or for photothermal heat generation.[21,22] While hot electrons received a lot of attention in the last few years, only bright plasmons were considered as their excitation channel. In P2 we proposed to use the suppressed radiative damping of dark plasmons to increase the yield of hot electrons. The gold nanoparticle layers, which were introduced in P1, are demonstrated to be an excellent material for the generation of hot electrons via the optical excitation of dark plasmons.

Using plasmons as a source for hot electrons requires a careful engineering of the loss channels, which are illustrated in Fig. 4.3a. Plasmons decay radiatively into photons Γ_{rad}, via internal damping inside the metal Γ_{b} (dephasing, intra- and interband transitions and electron-phonon scattering), and by scattering at the surface of the metal Γ_{surf}.[14] The latter process Γ_{surf} is the one responsible for hot carriers with high energy and should be maximized.[20] One approach is to reduce the size of the nanoparticles below the mean free path of the electrons, i.e. $<$10 nm, which will also reduce Γ_{rad}.[213,214] A drawback is that the small particle size hinders an efficient optical excitation of the plasmon as the optical absorption cross section scales with the particle volume.[53] A second approach is to increase Γ_{surf} by electromagnetic hotspots between the nanoparticles making use of the intense and strongly non-uniform electric field at the particle surface which breaks the conservation of electron momentum.[67–69] As dark plasmons possess intense electromagnetic hot spots while at the same time having a suppressed radiative damping Γ_{R} they are, once excited, ideal excitations for efficient hot electron generation.

In P2 we proposed the self-assembled nanoparticle layers (introduced in P1) as a material for hot electron generation. The dark interlayer plasmons benefit from suppressed radiative damping and at the same time absorb 50% of the incident light. The assembly into a hexagonal lattice with interparticle gaps of 2-3 nm leads to a large density of intense electromagnetic hot spots.[211] To access the electron dynamics and measure the hot electron population, the nanoparticle layers were characterized with time-resolved transient absorption (TTA) spectroscopy in the Lange group.[215] As Publication P2 only includes preliminary TTA data, the outcome of these measurements will be addressed in the outlook of this thesis.

To maximize the expected hot electron yield we proposed two ways for optimizing the

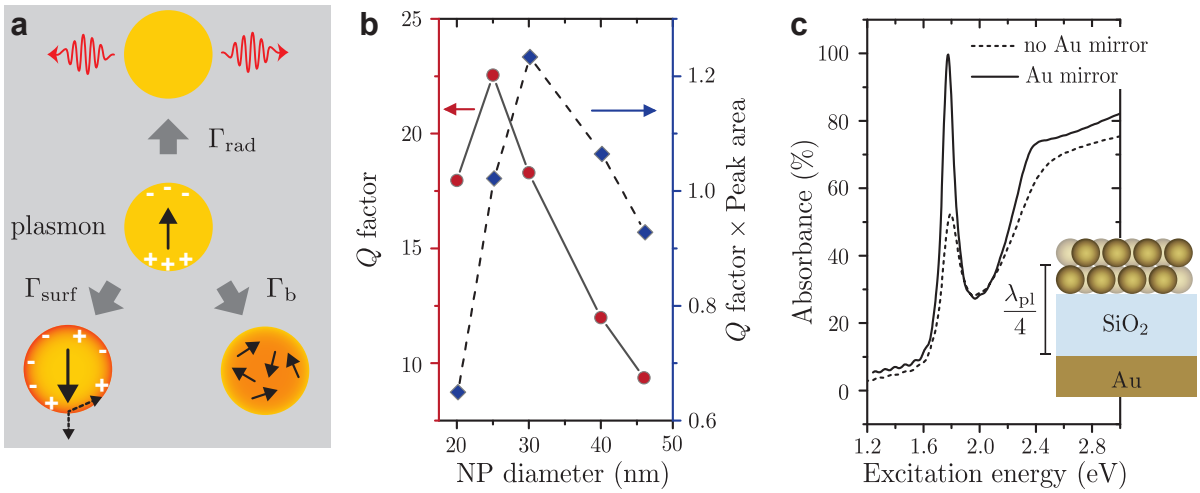

Figure 4.3. Summary of P2 - Direct optical excitation of dark plasmons for hot electron generation. (a) Loss channels of a plasmonic excitation, i.e., radiative decay Γ_{rad}, scattering of electrons at the nanoparticle surface Γ_{surf} and internal damping in the bulk metal Γ_b. Γ_{surf} generates hot electrons. (b) Optimization of the nanostructure design of a gold nanoparticle bilayer for hot electron generation. Quality factor $Q = \omega_{pl}/\Gamma_{pl}$ and its product with the area of the dark plasmon absorbance peak as a function of the nanoparticle diameter. (c) Simulated absorbance spectrum of a gold nanoparticle bilayer placed on top of a gold mirror with an SiO_2 spacer layer (solid line) and without substrate (dashed line). The optical absorbance increased to 100% at the wavelength λ_{pl} of the dark interlayer plasmon. Figures adapted form Publication P2 of this thesis.

nanostructure design. As Γ_{surf} scales inversely with the particle size we investigated how the properties of the dark bilayer plasmon evolve with decreasing particle size (Fig. 4.3b). The quality factor of the plasmon resonance that is associated with the field enhancement in the hot spots turned out to be largest for 25 nm particle diameters. The value of $Q = 22.5$ approaches the limit that is imposed by Γ_b for gold nanostructures and implies that Γ_{rad} is almost zero.[59] To also account for the optical absorption efficiency of the dark plasmon, we introduced the product of the quality factor with the area of the absorbance peak as a figure of merit for hot electron generation and identified 30 nm as the ideal particle diameter. This turned out to be much smaller than the 46 nm particle diameters used in P1.

Finally, we found that the optical absorbance of the dark bilayer plasmon is increased to 100% when placing the nanoparticle film on top of a gold mirror with an SiO_2 spacer (Fig. 4.3c). If the centre of the nanoparticle bilayer is placed at a quarter of the plasmon wavelength above the gold mirror the optical absorbance is strongly enhanced by an optical interference effect of the substrate.[216,217] In this case all of the light will be channeled into

the dark plasmon and $\Gamma_{\mathrm{rad}} = 0$, which increases the hot electron yield by a factor of two.

In summary, we demonstrated in P2 that the dark interlayer plasmons in gold nanoparticle layers are an ideal channel for hot electron generation. The concept as well as proof-of-principle experiments and simulations were published in the second paper forming this thesis, Mueller et al. *Direct optical excitation of dark plasmons for hot electron generation*, Faraday Discuss. 214, 159-173 (2019).

The focus of projects P1 and P2 was to engineer the properties of a plasmonic excitation itself, i.e., its optical absorption spectrum and loss channels. One main application of plasmonics is the enhancement of optical processes in nearby materials, which will be the focus for the remainder of this thesis. The extreme confinement of light in nanoscale gaps between plasmonic nanoparticles increases the local electric field intensity by orders of magnitude.[6,10] When bringing molecules or a nanoscale material into these electromagnetic hot spots, optical processes such as absorption, fluorescence, Raman scattering, and second-harmonic generation are strongly enhanced.[1,5,6] Project P3 focuses on the process of plasmon-enhanced optical absorption at visible light frequencies. Enhanced absorption is relevant, e.g., for increasing the photocurrent in optoelectronic or photovoltaic devices.[7,12,24]

At the time when I set out on this thesis, the family of two-dimensional materials emerged as a new building block for optoelectronic devices.[218–220] All types of materials, from semimetal, direct and indirect band-gap semiconductor to insulator, are available and can be combined by stacking.[221] Due to their two-dimensionality these materials strongly interact with their environment and their optical properties can be efficiently tuned by doping and chemical functionalization.[222,223] Being atomically thin, on the other hand, implies a low net quantum yield for photodetection which is a bottleneck for efficient photonic devices.[24] In order to increase the overall photoresponse, a number of hybrid optoelectronic devices were proposed that consisted of two dimensional materials as optical read outs and plasmonic nanostructures as enhancing agents.[179–181,224] In many works, an order of magnitude plasmonic enhancement of the quantum yield was achieved.

In Project P3 we investigated plasmon-enhanced optical absorption in the two dimensional carbon allotrope graphene. Graphene is particularly interesting for photodetection as it possesses a constant optical absorption of 2.3% over a broad spectral range and an exceptionally large carrier mobility.[24,222] It was demonstrated experimentally that a lattice of plasmonic nanoparticles deposited on top or below graphene could enhance the photocurrent in hybrid devices by an order of magnitude (Fig. 4.4a).[179–181] The exact mechanism of photocurrent generation, however, remained a matter of debate.[25–28] Several processes, i.e.,

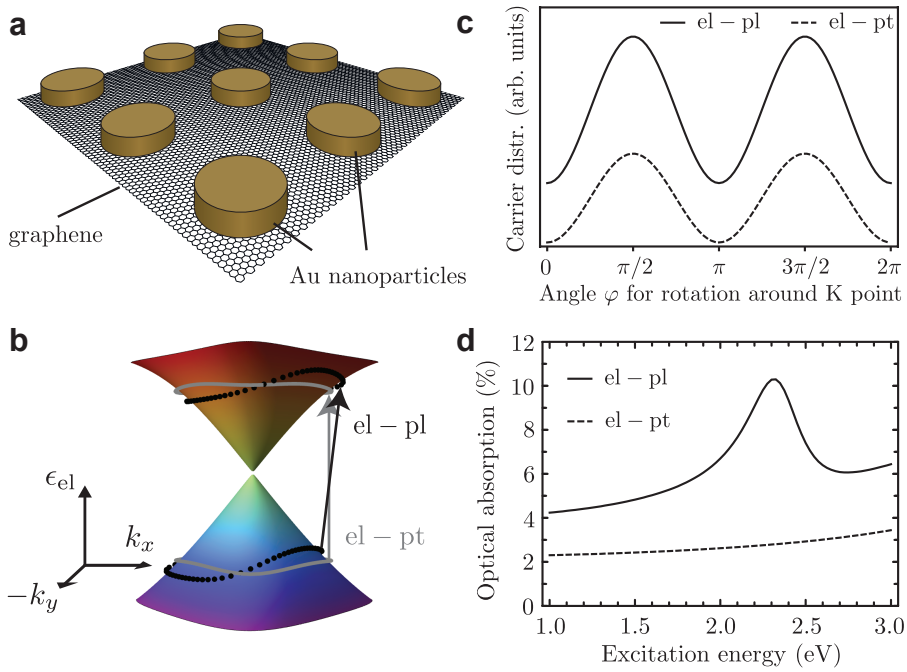

Figure 4.4. Summary of P3 - Microscopic theory of optical absorption in graphene enhanced by lattices of plasmonic nanoparticles. (a) Sketch of the experimental system considered. (b) Sketch of a non-vertical optical transition in the bandstructure of graphene due to a momentum transfer from the plasmonic lattice along k_x (black arrow). The dotted lines show all initial and final states in the valence and conduction band. The case of direct optical absorption without plasmonic enhancement is illustrated by the gray lines and arrow. (c) Photocarrier distribution around the K point calculated in the linear-band approximation. (d) Optical absorption of graphene as a function of excitation energy with a full tight-binding model. The cases of plasmonic enhancement (solid lines) and without enhancement (dashed lines) are compared. Figures adapted from Publication P3 of this thesis.

the electromagnetic field enhancement, thermoelectric effects and hot electron injection (see P2), were proposed to contribute to the photocurrent. A deterministic device layout therefore relies critically on theories that describe these microscopic processes.

To obtain a better understanding of how optical transitions in graphene are mediated by the plasmonic near field, we developed a microscopic model based on perturbation theory and on a tight-binding approximation for the electronic states of graphene. Following previous experiments,[179,180] we considered a square lattice of gold nanoparticles on top of graphene as the plasmonic nanostructure (Fig. 4.4a). The benefit of a periodic assembly of plasmonic nanoparticles was that we were able to derive an analytic expression for the coupling matrix element using Fourier optics. In that way, we got insight into the

distribution of photoexcited carriers in phase space and derived selection rules for the plasmon-mediated optical interband transitions in graphene.

The plasmonic nanostructure induced non-vertical optical interband transitions in the band structure of graphene around the K point (Fig. 4.4b, black arrow). In contrast, only vertical optical transitions are allowed for direct optical absorption, i.e., without the plasmonic nanostructure (Fig. 4.4b, gray arrow). To understand this effect I express the electric field of the plasmonic lattice in the graphene plane as a Fourier sum

$$\mathbf{E}_{\mathrm{pl},xy}(\mathbf{r}) = \sum_{\Delta\mathbf{q}\neq 0} \tilde{\mathbf{f}}(\Delta\mathbf{q}) \mathrm{e}^{\mathrm{i}\Delta\mathbf{q}\cdot\mathbf{r}}, \tag{4.1}$$

where $\tilde{\mathbf{f}}$ is the Fourier amplitude and $\mathbf{r}$ the position in the graphene lattice. Each of the Fourier components oscillate with a spatial frequency $\Delta\mathbf{q}$ which has units of momentum and takes discrete values determined by the lattice periodicity. When calculating the plasmon-electron matrix element we obtained the selection rule that a plasmon-mediated interband transition is allowed if the plasmonic lattice transfers a momentum $\Delta\mathbf{q}$ to the charge carriers in graphene. This momentum transfer is inversely proportional to the lattice constant. More generally, the optical selection rules can be obtained for any periodic plasmonic nanostructure by a Fourier analysis of the plasmonic near field in the graphene plane.

The microscopic theory gives insight into the distribution of photoexcited carriers in phase space.[178] In the absence of plasmonic enhancement and for illumination with linearly polarized light, the distribution is anisotropic around the K point and vanishes for two angles φ (Fig. 4.4c, dashed line).[225,226] This anisotropy is a manifestation of the sublattice pseudospin and was measured in polarization resolved pump-probe experiments.[227,228] We found that in the presence of plasmonic enhancement the carrier distribution is finite for all angles φ and cannot be calculated by straight-forward multiplication with an enhancement factor (Fig. 4.4c, solid line). This was attributed to the complex polarization pattern of the plasmonic near field $\mathbf{E}_{\mathrm{pl},xy}(\mathbf{r})$ in the xy plane. On the other hand we confirmed that the total optical absorption, which is obtained by integration over all optical transitions in phase space, is given by the product of the intrinsic absorption with a purely electromagnetic enhancement factor. While the intrinsic optical absorption of graphene ($\approx 2.3\%$) is almost constant as a function of excitation energy (Fig. 4.4d, dashed line), the gold nanoparticle lattice induces a plasmonic resonance at 2.3 eV which increases the absorption to 10% (Fig. 4.4d, solid line).

4. Connection of the papers

In summary, we developed a microscopic theory for the optical absorption in graphene enhanced by a lattice of plasmonic nanoparticles. This allowed me to derive selection rules for the plasmon-mediated optical interband transitions and to get insight into the photocarrier distribution in phase space. The theory can be used in future works to study the carrier dynamics in hybrid graphene-metallic nanostructure optoelectronic devices. This work was published in the third paper forming this thesis, Mueller et al., *Microscopic theory of optical absorption in graphene enhanced by lattices of plasmonic nanoparticles*, Phys. Rev. B 97, 235417 (2018).

Plasmon-enhanced optical absorption is one of the most fundamental plasmon-mediated optical processes. Such processes are not only used to enhance the quantum efficiency of optoelectronic devices, but also to detect and characterize molecules.[6,126,229] The latter is the aim of surface-enhanced infrared absorption spectroscopy that uses excitation energies in the meV range that match the vibrational transition energies of the molecules.[126] A complementary and related technique is surface-enhanced Raman scattering (SERS) in which molecular transitions are excited via the inelastic scattering of light.[6] The benefit of Raman scattering is that the vibrational molecular transitions are accessible with excitation energies in the visible where the resonances of localized surface plasmons occur.[6,124,125] Projects P4 and P5 focus on SERS from the theoretical and experimental side.

The phenomenon of surface-enhanced Raman scattering was discovered more than 40 years ago, but many aspects remain poorly understood.[141,230] Due to the multitude of contributing processes, it is a challenge to predict the result of a SERS experiment, such as the magnitude of the enhancement and its excitation energy dependence. There is a general agreement that the plasmonic enhancement mechanism is the dominant contribution to SERS.[6,32] Other processes such as the chemical interaction of the Raman probe with the metal surface, termed chemical enhancement, are expected to change the SERS intensity and activate new Raman modes.[142,143] To explain the experimental observations researchers have focused for many years on developing microscopic theories for chemical enhancement.[142–146] Only recently there has been a renewed interest in revisiting plasmonic enhancement and developing theories that go beyond the classical electromagnetic enhancement formalism.[231–234]

In Project P4 we developed a microscopic theory for the plasmon-enhanced Raman processes that occur in SERS. The theoretical framework is based, similarly to Project P3, on perturbation theory, which is known as the Kramers-Heisenberg-Dirac formalism for molecules or as the microscopic theory of Raman scattering for solid-state materials

as Raman scatterers,[124,125] see Section 2.2.1. These theories provide explicit expressions for the vibronic or electronic resonances and are therefore standard approaches to explain the excitation-energy dependence of the Raman cross section. Project P4 aimed at a theory that considers the plasmonic resonances of SERS as part of the Raman process, i.e., the plasmonic excitations are included in the Raman cross section in the same way as the molecular resonances. This gives rise to a description of plasmon-enhanced Raman scattering as a higher-order Raman process (HORa), which is illustrated by a Feynman diagram in Fig. 4.5a. The four vertices of the diagram describe the basic steps of the Raman process, i.e., photon-plasmon and plasmon-molecule interactions. The Raman process considered by the standard electromagnetic enhancement (EM) theory is illustrated for comparison in Fig. 4.5b. It consists only of two steps, i.e., photon-molecule interactions, and the plasmonic enhancement, which is modeled as an increase in intensity of the incoming and the Raman-scattered light.

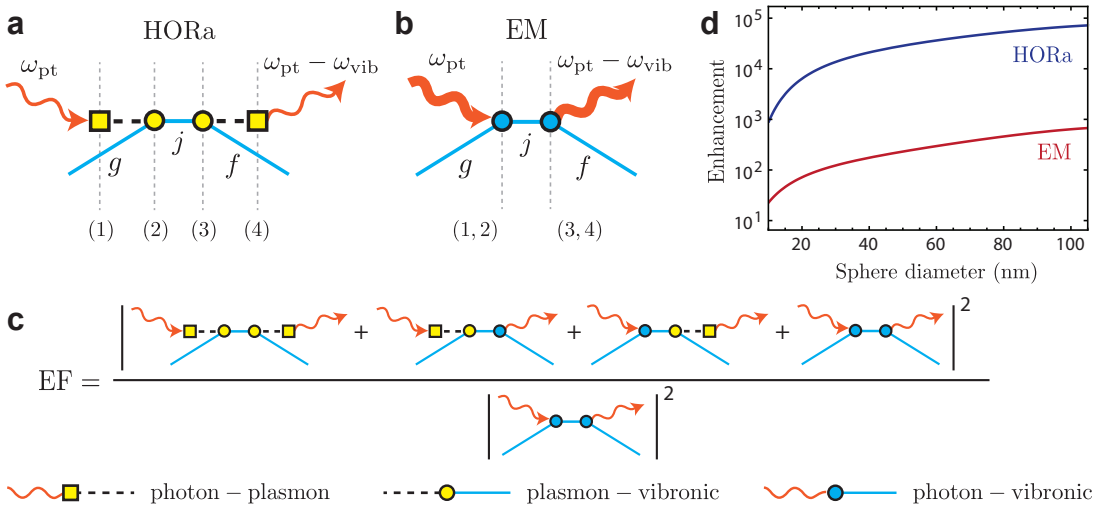

Figure 4.5. Summary of P4 - Surface-enhanced Raman scattering as a higher-order Raman process. (a) Feynman diagram for a plasmon-enhanced Raman process which corresponds to fourth-order perturbation theory. The Raman process consists of four steps (1)-(4) where a photon ω_{pt} couples via the plasmon to the vibronic ground g, intermediate j, and final states f of a molecule, and finally the Raman-scattered light $\omega_{pt} - \omega_{vib}$ is emitted. (b) Feynman diagram of the same Raman process as it is implicitly described by the EM-enhancement theory. Thick arrows illustrate an enhancement of the incoming and Raman-scattered light intensities. (c) Sketch that illustrates how the plasmonic enhancement is calculated. Each Feynman diagram corresponds to a Raman scattering amplitude. (d) Calculated plasmonic enhancement of the Raman cross section for a molecule close to a gold nanosphere. Figures adapted from Publication P4 of this thesis.

4. Connection of the papers

The Feynman diagram in Fig. 4.5a corresponds to a Raman scattering amplitude, which we calculated with perturbation theory. The plasmonic enhancement of the Raman cross section was obtained by summing the amplitudes of all relevant Raman processes, calculating the intensity as the absolute square and dividing by the intensity of the Raman process without enhancement (Fig. 4.5c). The scattering amplitudes need to be summed before calculating the absolute square, because the Raman processes have the same initial and final states. This gives rise to interference between the different scattering pathways which can lead to a selective increase or decrease of the enhancement for specific excitation energies. We obtained the following analytic expression for the plasmonic enhancement factor in SERS

$$\mathrm{EF}(\omega_{\mathrm{pt}}) = \left| \frac{\tilde{\mathcal{M}}_1 \tilde{\mathcal{M}}_2}{(\omega_{\mathrm{pt}} - \omega_{\mathrm{pl}} - \omega_{\mathrm{vib}} - \mathrm{i}\gamma_{\mathrm{pl}})(\omega_{\mathrm{pt}} - \omega_{\mathrm{pl}} - \mathrm{i}\gamma_{\mathrm{pl}})} + \frac{\tilde{\mathcal{M}}_1}{\omega_{\mathrm{pt}} - \omega_{\mathrm{pl}} - \mathrm{i}\gamma_{\mathrm{pl}}} + \frac{\tilde{\mathcal{M}}_2}{\omega_{\mathrm{pt}} - \omega_{\mathrm{pl}} - \omega_{\mathrm{vib}} - \mathrm{i}\gamma_{\mathrm{pl}}} + 1 \right|^2, \tag{4.2}$$

where ω_j are the energies of the plasmon "pl", the molecule "vib" and the photon "pt" from the excitation source. γ_{pl} is the spectral width of the plasmonic excitation. $\tilde{\mathcal{M}}_1$ and $\tilde{\mathcal{M}}_2$ are coupling factors that describe the interaction between the plasmonic excitation and the molecular states. In Ref. 156 we used the expression in Eq. (4.2) to analyze the excitation-energy dependence of the enhancement in a SERS experiment. By using $\tilde{\mathcal{M}}_1$, $\tilde{\mathcal{M}}_2$, ω_{pl} and γ_{pl} as fitting parameters, it was possible to extract the properties of the plasmonic excitation from the experimental data.

The coupling factors $\tilde{\mathcal{M}}_1$ and $\tilde{\mathcal{M}}_2$ in Eq. (4.2) contain matrix elements that describe the plasmon-photon, plasmon-molecule and photon-molecule interaction. The matrix elements correspond to the vertices of the Feynman diagrams in Figs. 4.5a and c. The description of SERS as higher-order Raman scattering required us to consider the photon-plasmon and the plasmon-molecule interaction as two subsequent steps. We calculated the corresponding matrix elements by a quantiziation of the plasmon.[235] In Ref. 209 we demonstrated that the matrix elements give rise to selection rules for SERS, which can be used for a rational design of SERS substrates.

We calculated the coupling factors for a molecule coupled to a gold nanosphere and a nanosphere dimer by deriving the eigenvectors of the plasmonic modes. The calculated plasmonic enhancement of the Raman cross section was two to three orders of magnitude larger than given by the electromagnetic enhancement theory (Fig. 4.5d). This appeared to be a promising explanation for a consistently larger measured enhancement in SERS experiments than predicted by the electromagnetic enhancement theory.[36,83,151,152] We

found, however, later that the discrepancy in Fig. 4.5d was attributed to a description that was too simplistic for the losses in gold; the coupling factors derived in P4 were only valid for a Drude metal. In fact only a few works attempted to quantize localized surface plasmons so far, as it is a challenge to incorporate the various losses that occur in noble-metal nanostructures.[235–238] In Project P4, we followed the approach introduced in Ref. 235. In a later work, we calculated the optical absorption cross section of the plasmon with the plasmon-photon matrix element and drew a comparison to experiment. That way we derived a correction factor that accounts for the losses in gold.[239] The publication is attached in Appendix B of this thesis.

Overall we developed a microscopic theory of plasmonic enhancement in SERS that considers SERS as higher-order Raman scattering. We derived coupling matrix elements that give rise to selection rules for SERS substrates and obtained an analytic expression for the plasmonic enhancement factor, which can be used to analyze experimental data.[156,209] The theoretical framework and a derivation of all coupling matrix elements were published in the fourth paper forming this thesis, Mueller et al., *Surface-enhanced Raman scattering as a higher-order Raman process*, Phys. Rev. A 94, 023813 (2016).

While Project P4 dealt with the fundamental processes underlying SERS, Project P5 is an application of SERS. The ability to focus light with plasmonic nanostructures into nanoscale volumes opens the possibility to characterize the properties of materials on length scales much smaller than the diffraction limit.[1,9] Raman scattering is an ideal tool for this task and is frequently used in materials science to measure strain, doping or defect densities.[124] In Project P5, we demonstrated that SERS can be used for the characterization of nanoscale strain and doping in graphene.

The experimental system which was used in Project P5 is illustrated in Fig. 4.6a; it was designed in an earlier work in the Reich group by Sebastian Heeg.[29,240] Exfoliated flakes of graphene were transferred on top of multiple lithographically-fabricated gold nanodisk dimers. The dimers were spaced several micrometers apart such that coupling between different dimers was negligible. For excitation energies that matched the bright plasmon mode of the gold nanodimer, the Raman spectrum of graphene was strongly enhanced by SERS.[29,240] The substrate adhesion pulled the graphene into the gap between the two gold nanoparticles. This induced a nanoscale strain of completely unknown configuration; see AFM image in Fig. 4.6b. Additionally, the gold nanostructure induced locally an n-type doping in graphene. Both, strain and doping affect the plasmon-enhanced Raman G and 2D modes of graphene, that are plotted in Fig. 4.6c. The modes split into three components

of different intensity. The two components with the lowest Raman shift corresponded to the locally enhanced Raman spectrum of graphene in the interparticle gap (red and blue in Fig. 4.6c).[29,240] The peaks were shifted from the intrinsic spectral positions (dashed lines) because of hydrostatic strain and doping; the peak splitting occurred because of shear strain.

Extracting the local properties of graphene in the dimer gap turned out to be a challenge

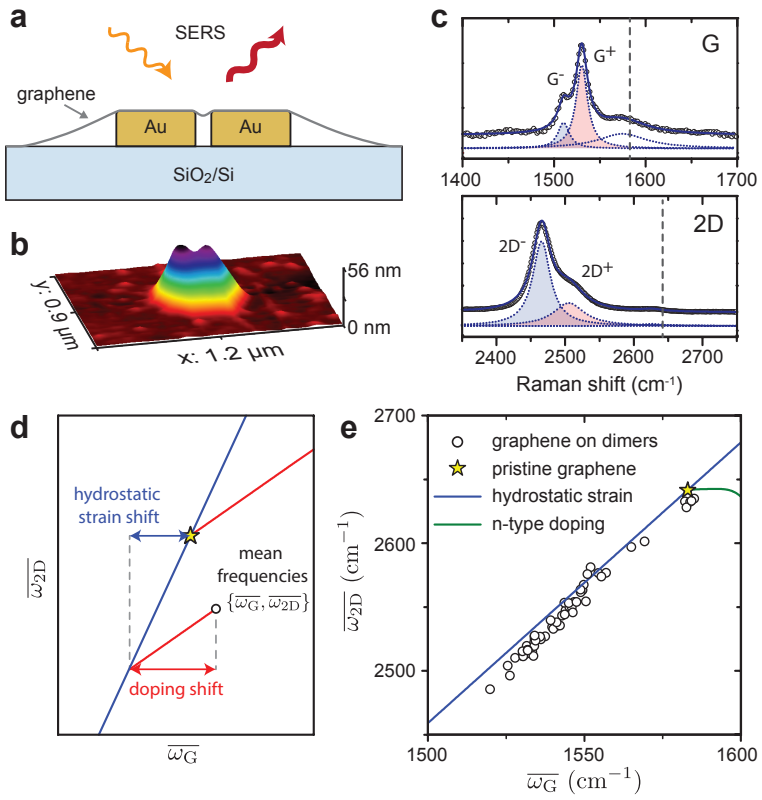

Figure 4.6. Summary of Project P5 - Evaluating arbitrary strain configurations and doping in graphene with Raman spectroscopy. (a) Sketch of the experimental system. Graphene is deposited on a plasmonic gold nanodimer and characterized by SERS. (b) AFM image of graphene covering a nanodimer. (c) Raman spectra of the G and 2D mode measured for graphene on top of a gold nanodimer. The peaks are split into three components and the expected peak positions without strain and doping are indicated by dashed lines. (d) Sketch of a correlation analysis of the mean frequencies $\overline{\omega_{\mathrm{G}}} = (\omega_{\mathrm{G}^-} + \omega_{\mathrm{G}^+})/2$ and $\overline{\omega_{\mathrm{2D}}} = (\omega_{\mathrm{2D}^-} + \omega_{\mathrm{2D}^+})/2$ for separating the frequency shifts from hydrostatic strain and charge doping applied for a data point $\{\overline{\omega_{\mathrm{G}}}, \overline{\omega_{\mathrm{2D}}}\}$. The expected frequencies are illustrated by a yellow star for no strain and doping, a blue line for hydrostatic strain and a red line for p-type doping. (e) Statistical analysis of the mean frequencies from the Raman spectra of graphene-covered gold nanodimers. Figures adapted from Publication P5 of this thesis.

as strain and doping affected the spectral positions of the Raman modes simultaneously. Lee *et al.*[208] suggested in a previous work to use a correlation analysis of the G and 2D peak positions to separate the spectral shifts from strain and doping. This method required, however, knowledge of the strain configuration, which was unknown for the case of graphene on the nanodimers. We developed a general methodology to evaluate arbitrary strain configurations and doping from the Raman spectrum of graphene. For this method one has to eliminate the peak splitting from shear strain by calculating the mean values $\overline{\omega_{\mathrm{G}}} = (\omega_{\mathrm{G}^-} + \omega_{\mathrm{G}^+})/2$ and $\overline{\omega_{\mathrm{2D}}} = (\omega_{\mathrm{2D}^-} + \omega_{\mathrm{2D}^+})/2$ of the spectral peak positions, i.e., of the red and blue peak components in Fig. 4.6c. The benefit is that the mean frequencies $\overline{\omega_{\mathrm{G}}}$ and $\overline{\omega_{\mathrm{2D}}}$ are only affected by doping and the hydrostatic strain component. The associated peak shifts are separated by a correlation analysis which is explained in Fig. 4.6d. Finally the magnitudes of hydrostatic strain and doping are calculated from the peak shifts and the shear strain component from the peak splitting.

We applied this methodology to the Raman spectra of 60 graphene-covered nanodimers. The mean frequencies of the Raman modes are shown in a correlation plot in Fig. 4.6e. The data points followed a linear trend close to the peak positions expected for purely hydrostatic strain. From the spectrum in Fig. 4.6c we extracted a local hydrostatic strain of 2.5%, a shear strain of 1.4% and an n-type doping of 8.5 $\times 10^{12}$ cm^{-2}. These values were incredibly large when comparing with those reported in other works.[25] This was expected because we probed exclusively the local doping and strain in the nanoscale area of graphene at the nanodimer gap. From a statistical analysis we found that the hydrostatic and shear-strain components were uncorrelated, which showed that each dimer induced a different strain configuration. Our methodology for strain evaluation could be only applied to this complicated case because it required no assumption on the strain configuration as an input parameter.

The methodology for strain and doping evaluation in graphene, which we developed in Project P5, is very general. It is also applicable to graphene on substrates without plasmonic enhancement. We demonstrated this for an elastic substrate that induced uniaxial strain in graphene when being deflected in one direction. In this specific case the strain configuration was known and we could extract reference values for the peak shifts from hydrostatic strain, which were in good agreement with other works.[205,206] Furthermore, we demonstrated that the mean frequencies $\overline{\omega_{\mathrm{G}}}$ and $\overline{\omega_{\mathrm{2D}}}$ can be directly measured when using a Raman spectrometer with circularly corotating light polarization. This is especially useful when the peak splitting by shear strain cannot be resolved.

In summary, we used SERS to extract the local charge doping and strain in a nanoscale

area of graphene on top of a gold nanodimer. For this we developed a general methodology for the evaluation of arbitrary strain configurations and doping in graphene by Raman spectroscopy. The experimental data and methodology was published in the last paper forming this thesis, Mueller et al., *Evaluating arbitrary strain configurations and doping in graphene with Raman spectroscopy*, 2D Materials 5, 015016 (2018).

5 | Summary and outlook

In this thesis I realized projects that improved the fundamental understanding of plasmon-mediated optical processes. I introduced dark interlayer plasmons as new optical excitations in ordered films of metallic nanoparticles, which have potential applications in photocatalysis (Projects P1 and P2). I developed microscopic theories for the plasmon-enhanced optical absorption and Raman scattering in nearby materials, such as molecules and graphene (Projects P3 and P4). Finally, I introduced a methodology to evaluate strain and doping from the Raman spectrum of graphene, which I applied to analyze nanoscale strain distributions induced by a plasmonic nanostructure. The publications forming this thesis set a basis for a number of ongoing and future studies, which I will briefly describe in the following.

One key advantage of the dark interlayer plasmon is its tunability by geometrical parameters and layer number. We demonstrated this in Projects P1 and P2 with FDTD simulations. The theoretical predictions motivated us to study the optical properties of nanoparticle films that consisted of different particle diameters. Fig. 5.1a shows TEM images of gold nanoparticle monolayers with particle diameters of 30 nm, 46 nm and 59 nm. The reflectance spectra, measured on bilayers of the three samples, contained pronounced reflectance dips from the direct optical excitation of dark plasmons (Fig. 5.1b). The striking feature of Fig. 5.1b is the different excitation energies of the dark plasmons. These cover a broad spectral range, from 1.23 eV for the 59 nm nanoparticles to 1.75 eV for the 30 nm nanoparticles. This nicely demonstrates the tunability by geometrical parameters.

Another prediction of Project P2 was that the dark plasmon absorption can be increased to 100% when placing the nanoparticle film above a reflective substrate. We realized this experimentally via a collaboration with Katja Höflich at Helmholtz Zentrum Berlin. She deposited an SiO_2 spacer layer on top of a substrate with a continuous gold film. Fig. 5.1c shows the absorbance spectrum of a gold nanoparticle bilayer on top of the substrate (red line). A spectrum of a sample without the reflective substrate is shown for comparison

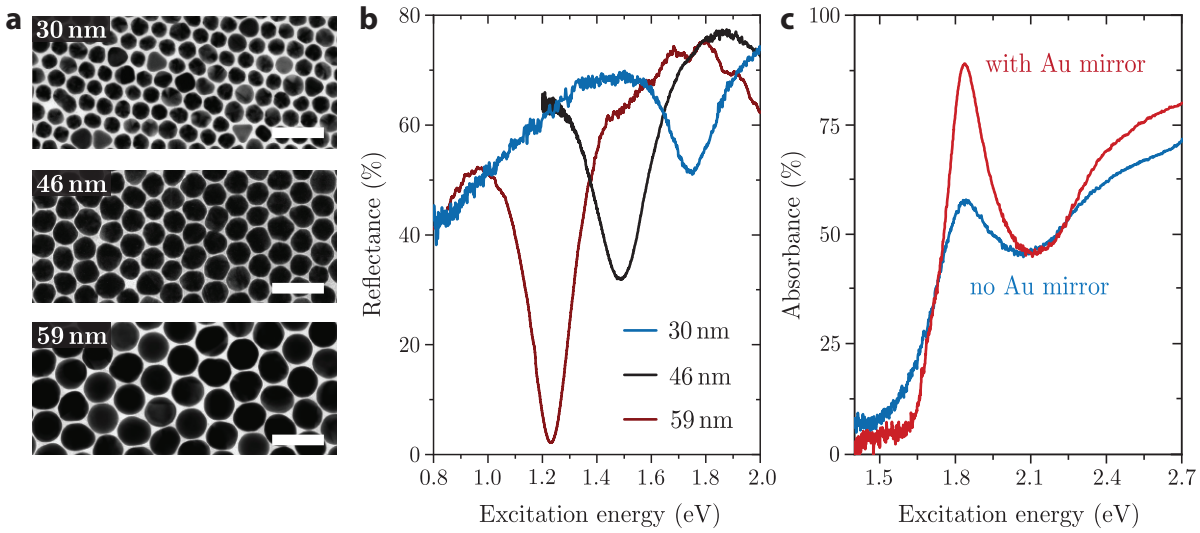

Figure 5.1. Tunability of dark plasmon resonances in gold nanoparticle bilayers. (a) TEM images of close-packed gold nanoparticle monolayers with mean diameters d and interparticle gaps g of $d = 30\,\text{nm}$ and $g = 4\,\text{nm}$, $d = 46$ nm and $g = 2\,\text{nm}$, and $d = 59\,\text{nm}$ and $g = 1\,\text{nm}$, from top to bottom. The scale bars are 100 nm. (b) Reflectance spectra of close-packed bilayers of gold nanoparticles with the same dimensions as in (a). (c) Absorbance spectrum of a gold nanoparticle bilayer placed on top of an Au substrate with a 58 nm SiO_2 spacer layer (red curve). The blue curve is a reference spectrum measured without the reflective substrate. The nanoparticle diameters and interparticle gaps were estimated as $d = 42\,\text{nm}$, and $g = 3\,\text{nm}$ from TEM images.

(blue line). The optical absorbance of the dark plasmon is increased tremendously to 89%. This is remarkable because the interlayer plasmon has a vanishing net dipole moment.

In Project P2 we proposed dark interlayer plasmons as an excitation channel for hot electrons. The hot electron yield was probed with time-resolved transient absorption spectroscopy (TTA) by the Lange group at the University of Hamburg. As mentioned in Section 4, Publication P2 contained only preliminary TTA data. Later, we performed a more detailed analysis by correlating the measurement spots of TTA with optical microscope images and micro-reflectance spectra (Fig. 5.2). Fig. 5.2a shows the electron-phonon (e-ph) coupling time obtained with TTA, which serves as a measure for the hot carrier yield after excitation with a pump pulse.[14,215] Two sample regions were characterized as shown in Fig. 5.2b. Area 1 consisted solely of a monolayer while area 2 also contained bi- and multilayers. The e-ph coupling time was identical for the two sample areas in the spectral range above 2 eV, but differed for lower excitation energies (Fig. 5.2a). The larger e-ph coupling time for the bi- and multilayers is attributed to a higher initial temperature

of the electron gas and hints to a larger hot electron yield.[14,215] This correlates with micro-reflectance measurements on the nanoparticle layers. While the optical response is similar for all layer numbers above 2 eV, it differs significantly for lower energies because of the excitation of dark plasmons in the bi- and multilayers. This nicely demonstrates that dark interlayer plasmons serve as an excitation channel for hot electrons. The hot charge carriers may trigger photocatalytic reactions in nearby molecules.[21,22] Photoelectrochemistry measurements in which the nanoparticle layers are used as an electrode are currently planed in the Lange group.

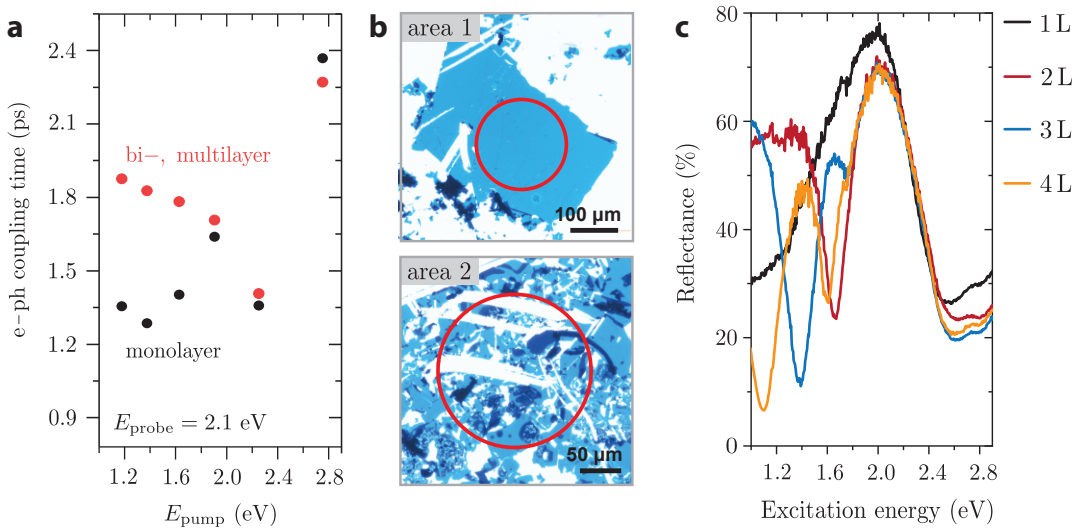

Figure 5.2. Excitation of hot charge carriers via the decay of dark interlayer plasmons. (a) Electron-phonon (e-ph) coupling time measured with time-resolved transient absorption spectroscopy (TTA) on a nanoparticle monolayer (black dots) and on bi- and multilayers (red dots). (b) Optical transmission microscope images of the sample areas probed by TTA. The red circles show the approximate size and position of the pump pulse. Area 1 is a homogeneous monolayer (light blue) and area 2 contains also bi- and multilayers (darker blue). (c) Micro-reflectance spectra of one to four gold nanoparticle layers. The excitation of dark plasmons is visible as reflectance dips for the bi- and multilayers. The nanoparticle layers consisted of gold particles with a mean diameter of 42 nm and an interparticle gap size of 3 nm estimated for TEM images.

Another direct application of the dark interlayer plasmons is SERS. Fig. 5.3a shows the simulated near field enhancement for a gold nanoparticle bilayer when the incoming light matches the energy of the dark plasmon (see Ref. 241 for a detailed analysis). The field amplitude is enhanced by a factor of 50 in the gaps between the nanoparticles and depends strongly on excitation energy (Fig. 5.3b). This leads to a SERS enhancement of $\approx 2 \cdot 10^6$ when choosing an excitation energy of 1.54 eV. The enhancement is smaller than for the

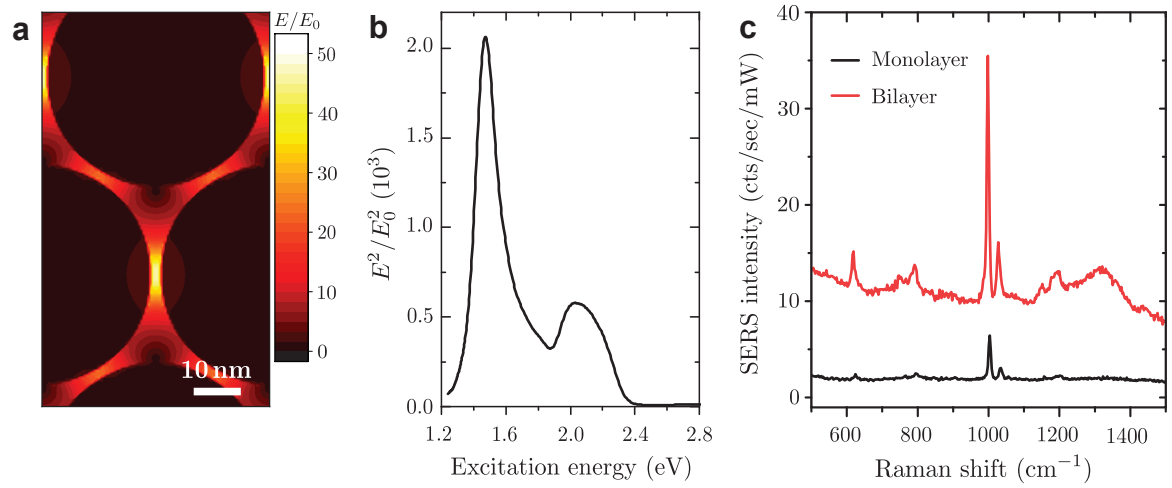

Figure 5.3. Surface-enhanced Raman scattering with a dark interlayer plasmon. (a) Simulated enhancement of the near field amplitude for a bilayer of 46 nm gold nanoparticles with 2 nm gaps illuminated with linearly polarized light and 1.48 eV excitation energy. The plot is a cross section through the upper layer. (b) Excitation-energy dependence of the near field intensity enhancement at the center of a hot spot in (a). (c) SERS spectrum measured on a bilayer (red) and monolayer (black) of 42 nm gold nanoparticles. The bilayer provides additional enhancement because of the excitation of the dark interlayer plasmon. The spectra show the Raman modes of polystyrene molecules that were used as ligands in the synthesis of the nanoparticle layers.

nanoparticle dimer in Fig. 2.5a because the dimer efficiently extracts electromagnetic energy from its environment over the length scale of the light wavelength. The gold nanoparticle layers, on the other hand, possess a large number $10^3/\mu m^2$ of field hot spots which increases the total SERS signal measured in an experiment.

To approach the SERS enhancement from dark interlayer plasmons experimentally, I measured the enhanced Raman spectrum of the polystyrene ligand molecules that surround the gold nanoparticles. Fig. 5.3c shows the SERS spectrum measured on a gold nanoparticle bilayer (red line) for an excitation energy of 1.58 eV close to the resonance of the dark plasmon. The SERS signal is six times larger than for a monolayer (black line), which only provides enhancement via the lightning rod effect. This demonstrates the additional SERS enhancement from the dark interlayer plasmon. Further studies are currently conducted in the Reich group to determine the SERS enhancement per molecule and its dependence on excitation energy and layer number. The gold nanoparticle layers may serve as a SERS substrate for different molecules that can be brought into the interparticle gaps by dropcasting from solution.

A more detailed analysis of the plasmonic SERS enhancement requires theoretical modeling, which was the aim of Project P4. Publication P4 introduced the general theoretical framework of treating SERS as higher-order Raman (HORa) scattering. In a recent work, we used this theoretical framework for studying the dependence of the plasmonic SERS enhancement on excitation energy.[239] I implemented the microscopic theory for a molecule close to a silver nanoparticle by calculating all coupling matrix elements. Fig. 5.4a shows the plasmonic SERS enhancement as a function of excitation energy for three metal-molecule distances. The enhancement profile consists of an incoming plasmonic SERS resonance when the incoming laser light matches the plasmon frequency ($\omega_{\mathrm{L}} = \omega_{\mathrm{pl}}$) and an outgoing resonance when the Raman-scattered light matches the plasmon ($\omega_{\mathrm{L}} - \omega_{\mathrm{vib}} = \omega_{\mathrm{pl}}$); see Sec. 2.2.3 for details. Besides an overall decrease in plasmonic enhancement, an increase in metal-molecule distance strongly changes the excitation energy dependence of the enhancement. When the molecule is placed on the nanoparticle surface its Raman dipole experiences the strongest plasmonic enhancement and the incoming- and outgoing SERS resonances are almost of equal intensity (Fig. 5.4a, top). When the metal-molecule distance is increased to the nanoparticle radius, the enhancement profile consists only of an incoming resonance; the outgoing resonance is entirely missing (Fig. 5.4a, middle). For larger metal-molecule distances the enhancement profile is strongly asymmetric and obtains a Fano line shape (Fig. 5.4a, bottom).

The reason for the asymmetric enhancement profile is interference between the scattering processes that are depicted as Feynman diagrams in Fig. 4.5c. We studied this in detail in Ref. 239 and showed that the Raman amplitudes of the different scattering channels add constructively at the incoming resonance and destructively at the outgoing resonance. The interference can be switched off when only considering the scattering process in Fig. 4.5a. In this case the enhancement profile consists of incoming- and outgoing resonances with equal intensity (Fig. 5.4a, dashed lines).

Signatures of interference between different scattering channels were observed in experiments conducted by Sören Wasserroth in the Reich group.[156] He measured the excitation energy dependence of the SERS signal of graphene deposited on gold nanodimers (same samples that I used in Project P5 to study nanoscale strain and doping). Graphene is an ideal material for this study because the Raman polarizabilities of the G and 2D mode are independent of excitation energy in the absence of plasmonic enhancement. Fig. 5.4b shows the SERS enhancement of the G mode (top) and 2D mode (bottom) as a function of excitation energy. The experimental data are excellently explained by a fit with the plasmonic enhancement factor from the HORa theory of SERS in Eq. (4.2) (solid lines).

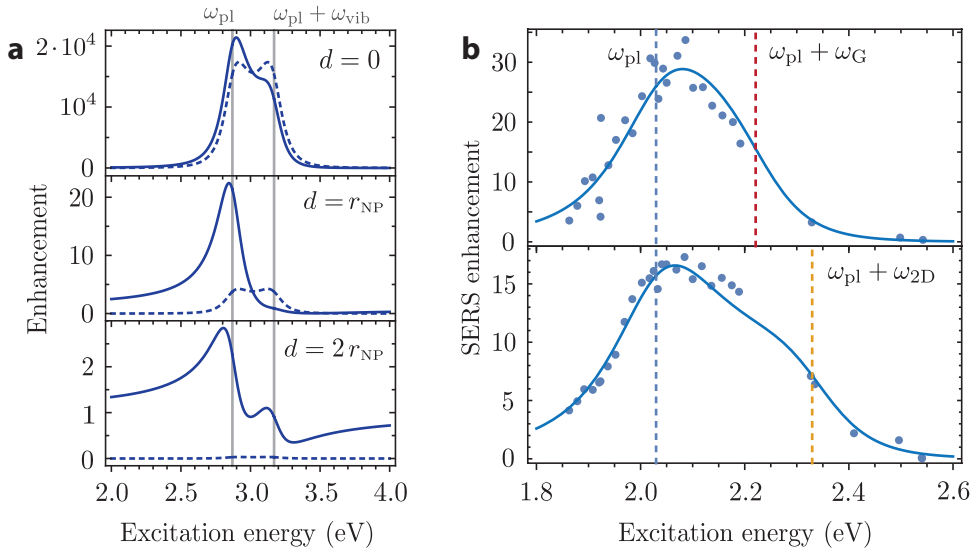

Figure 5.4. Analyzing the excitation energy dependence of the plasmonic SERS enhancement with the HORa theory of SERS. (a) Calculated plasmonic SERS enhancement for a molecule next to a silver nanoparticle as a function of excitation energy for different metal-molecule distances d, given in units of the nanoparticle radius $r_{\mathrm{NP}} = 15.5\,\mathrm{nm}$. The dashed lines are the SERS enhancement when only considering the scattering process in Fig. 4.5a. The energies for which the incoming- and Raman-scattered light matches the plasmon are shown by gray lines. The plasmon energy, spectral width, Raman shift and background dielectric function were set to $\hbar\omega_{\mathrm{pl}} = 2.87\,\mathrm{eV}$, $\hbar\gamma_{\mathrm{pl}} = 108\,\mathrm{meV}$, $\hbar\omega_{\mathrm{vib}} = 300\,\mathrm{meV}$ and $\epsilon_m = 2.31$. The nanoparticle center was placed at the origin, the incident light polarization and molecular Raman dipole along x and the molecule was moved along the x axis. (b) Experimental SERS enhancement of the Raman G (top) and 2D (bottom) mode of graphene as a function of excitation energy from Ref. 156 (data points). The solid lines are a fit with Eq. (4.2) from the HORa theory of SERS. The energies for which the incoming- and Raman-scattered light matches the plasmon are highlighted by dashed lines. Figures adapted from Ref. 239.

The outgoing SERS resonances of the G and 2D mode are weaker that the incoming resonances, which nicely matches the theoretical predictions for a molecule in Fig. 5.4a.

A more detailed and quantitative modeling of the plasmon-enhanced Raman spectrum of graphene requires the development of a HORa theory for SERS in solid-state materials. The microscopic theory for plasmon-enhanced optical absorption in graphene in Project P3 was an important step in this direction. Fig. 5.5a shows a Feynman diagram for a plasmon-enhanced first-order Raman process in a solid state material, such as the G mode of graphene. It consists of five vertices that correspond to photon-plasmon, plasmon-electron, and electron-phonon interaction matrix elements. In Project P3 I derived the general

theoretical framework to calculate these matrix elements (except for electron-phonon interaction). Calculating the plasmon-electron matrix element required considering a periodic lattice of plasmonic nanoparticles because of the infinite lattice sums that appear in graphene's tight-binding wave functions. I obtained an analytic expression for the matrix element by a Fourier expansion of the plasmonic near field. The plasmon-enhanced optical absorption was then calculated as the sum of the transition probabilities associated with each Fourier component, which are given by the absolute square of the respective matrix elements.

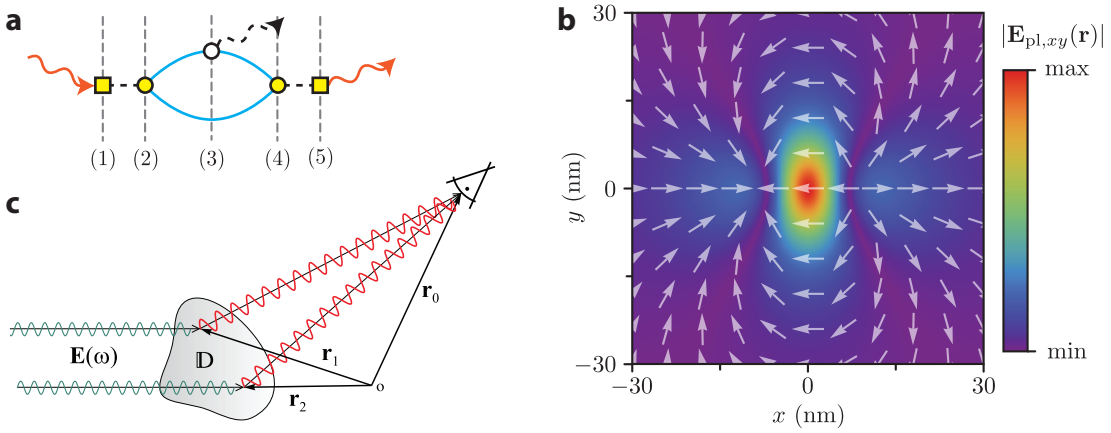

Figure 5.5. Microscopic theory of surface-enhanced Raman scattering in solid state materials. (a) Feynman diagram of a plasmon-enhanced first-order Raman process in a solid state material within the HORa theory of SERS. It consists of five steps: (1) photon-plasmon, (2) plasmon-electron, (3) electron-phonon, (4) electron-plasmon and (5) plasmon-photon interaction. (b) Electric near field amplitude in a graphene sheet blow a plasmonic nanoparticle lattice. The contour plot shows the magnitude and the arrows the polarization direction of the plasmonic near field. Figure from Publication P3 of this thesis. (c) Scheme of two scattering channels that contribute to a spatially coherent Raman process (adapted from Ref. 242). The incoming laser light $\mathbf{E}(\omega)$ (green lines) excites two Raman processes at positions $\mathbf{r}_1$ and $\mathbf{r}_2$. The electric fields of the Raman-scattered light waves (red lines) add coherently at the detector at position $\mathbf{r}_0$.

The steps for calculating plasmon-enhanced Raman scattering are different. As the initial and final electronic states of a Raman process in graphene are identical, the Raman scattering amplitudes that belong to the different Fourier components must be summed before calculating the absolute square. I implemented the microscopic theory for the G mode of graphene, using the electron-phonon matrix element from Ref. 185, and found a plasmonic enhancement much lower than in experiment.[243] The reason were cancellations of Raman scattering processes that occurred at different positions in the graphene lattice.

The microscopic theory lead to the enhancement factor (when neglecting the Raman shift)

$$\mathrm{Enh} = \left| \iint d^2\mathbf{r} \left[\mathbf{E}_{\mathrm{inc}} + \mathbf{E}_{\mathrm{pl}}(\mathbf{r})\right] \right|^4 / E_{\mathrm{inc}}^4, \tag{5.1}$$

where the integral is calculated over all positions in the graphene plane and $\mathbf{E}_{\mathrm{inc}}$ is the incident electric field without plasmonic nanostructure. Fig. 5.5b shows the electric near field $\mathbf{E}_{\mathrm{pl}}(\mathbf{r})$ from a plasmonic nanoparticle lattice in the graphene plane, as calculated in Publication P3 of this thesis. It consists of field components at different positions that have the same magnitude but opposite polarization. The Raman scattering amplitudes associated with these positions canceled when calculating the plasmon-enhanced G mode. This is equivalent to a Raman process where the Raman-scattered light that is emitted from different positions in the graphene lattice adds coherently at the detector (Fig. 5.5c).[242] Lukas Novotny and coworkers suggested that such a spatially coherent Raman process is possible in graphene, but can only take place within a phonon coherence length of $\approx 30\,\mathrm{nm}$.[242,244] A description of plasmon-enhanced Raman scattering in graphene requires an account for this coherence length, which will be subject of future work.

In summary, the projects realized within this thesis set the basis for ongoing and future studies; some of which were already published.[155,156,209,239,241] Dark interlayer plasmons were introduced as a new optical excitation in metallic nanoparticle films with potential applications in photocatalysis and SERS (Publications P1, P2 and Ref. 241). The interaction of plasmonic nanostructures with nanoscale materials and molecules was modelled with microscopic theories (Publications P3 and P4). These provided insight into the microscopic processes underlying plasmonic enhancement and helped to understand the outcome of experiments, such as the plasmon-enhanced Raman spectrum of graphene and of molecules encapsulated inside carbon nanotubes.[155,156] The plasmon-enhanced Raman spectrum of graphene was also used to analyze nanoscale strain and doping induced by a plasmonic nanostructure. A general method was developed for separating the contributions of strain and doping to the Raman frequencies of graphene that is also applicable to other two-dimensional materials (Publication P5).

Appendix

A | Papers as published

A.1. ACS Photonics 5, 3962-3969 (2018) and Supporting Information

For copyright reasons this publication is not included in the online version. It can be found on the publisher website under the link https://doi.org/10.1021/acsphotonics.8b00898.

The complete bibliographic information of this publication is:

Niclas S. Mueller*, Bruno G. M. Vieira*, Florian Schulz, Patryk Kusch, Valerio Oddone, Eduardo B. Barros, Holger Lange, and Stephanie Reich,
Dark Interlayer Plasmons in Colloidal Gold Nanoparticle Bi- and Few-Layers,
ACS Photonics 5, 3962-3969 (2018)
*Shared first authorship with Bruno G. M. Vieira

A.2. Faraday Discussions 214, 159 (2019)

The complete bibliographic information of this publication is:

Niclas S. Mueller, Bruno G. M. Vieira, Dominik Höing, Florian Schulz, Eduardo B. Barros, Holger Lange, and Stephanie Reich,
Direct optical excitation of dark plasmons for hot electron generation,
Faraday Discussions 214, 159 (2019)

A.3. Physical Review B 97, 235417 (2018) and Supporting Information

For copyright reasons this publication is not included in the online version. It can be found on the publisher website under the link https://doi.org/10.1103/PhysRevB.97.235417.

The complete bibliographic information of this publication is:

Niclas S. Mueller and Stephanie Reich,
Microscopic theory of optical absorption in graphene enhanced by lattices of plasmonic nanoparticles,
Physical Review B 97, 235417 (2018)

A.4. Physical Review A 94, 023813 (2016)

The complete bibliographic information of this publication is:

Niclas S. Mueller, Sebastian Heeg, and Stephanie Reich,
Surface-enhanced Raman scattering as a higher-order Raman process,
Physical Review A 94, 023813 (2016)

A.5. 2D Materials 5, 015016 (2018) and Supporting Information

For copyright reasons this publication is not included in the online version. It can be found on the publisher website under the link https://doi.org/10.1088/2053-1583/aa90b3.

The complete bibliographic information of this publication is:

Niclas S. Mueller, Sebastian Heeg, Miriam Peña Alvarez, Patryk Kusch, Sören Wasserroth, Nick Clark, Fredrik Schedin, John Parthenios, Konstantinos Papagelis, Costas Galiotis, Martin Kalbáč, Aravind Vijayaraghavan, Uwe Huebner, Roman Gorbachev, Otakar Frank, and Stephanie Reich,
Evaluating arbitrary strain configurations and doping in graphene with Raman spectroscopy, 2D Materials 5, 015016 (2018)

B | Paper reprint - Frontiers in Chemistry 7, 470 (2019)

For copyright reasons this publication is not included in the online version. It can be found on the publisher website under the link https://doi.org/10.3389/fchem.2019.00470.

The complete bibliographic information of this publication is:

Niclas S. Mueller and Stephanie Reich,
Modeling Surface-Enhanced Spectroscopy With Perturbation Theory,
Frontiers in Chemistry 7, 470 (2019)

C | German abstract

Ziel dieser Arbeit ist es, ein besseres Verständnis von optischen Prozessen zu erlangen, die durch lokalisierte Oberflächenplasmonen gesteuert werden. Dafür habe ich grundlegende Anregungsmechanismen von Plasmonmoden, sowie die Verstärkung von optischer Absorption und Ramanstreuung, mit experimentellen und theoretischen Methoden untersucht.

Ich stelle eine neuartige plasmonische Anregung in geschichteten Filmen von metallischen Nanopartikeln vor. Dieses dunkle Plasmon besteht aus antiparallelen plasmonischen Dipolen in den Nanopartikeln benachbarter Lagen und kann aufgrund von Feldretardierung direkt mit Licht angeregt werden. Ich zeige mit Experimenten und Simulationen, dass diese Anregung eine reduzierte Strahlungsdämpfung aufweist und zu einer ausgeprägten, durchstimmbaren Lichtabsorption im nahinfraroten Spektralbereich führt. Da die Nanopartikelfilme mittels Selbstorganisation von Nanopartikeln hergestellt werden können, eignen sie sich für die großflächige Beschichtung von Oberflächen. Aufgrund der unterdrückten radiativen Dämpfung sind dunkle Plasmonen in Nanopartikelfilmen ein idealer Anregungskanal für heiße Elektronen, mit Anwendungen in der Fotokatalyse.

Mit mikroskopischen Theorien habe ich die Interaktion von plasmonischen Nanostrukturen mit angrenzenden Nanomaterialien untersucht. Ich zeige, dass das plasmonische Nahfeld eines Gitters von Goldnanopartikeln nicht-vertikale optische Übergänge in Graphen anregt. Die Auswahlregeln für diese Übergänge hängen von der Periodizität der plasmonischen Nanostruktur ab. Die mikroskopische Theorie führt zu einem besseren Verständnis der Photostromentstehung in Graphen-basierten optoelektronischen Detektoren. Als Zweites stelle ich ein allgemeines Konzept zur Beschreibung von plasmon-verstärkter Ramanstreuung mit Störungstheorie vor. Die analytischen Ausdrücke aus dieser Theorie eignen sich, um die Abhängigkeit der plasmonischen Verstärkung von der Anregungsenergie zu untersuchen. Mittels einer Implementierung für ein Molekül nahe eines plasmonischen Nanopartikels zeige ich, dass die Verstärkung stark von der Interferenz verschiedener Streuprozesse beeinflusst wird.

Plasmon-verstärkte Ramanstreuung ist ideal, um zu untersuchen, wie Materialeigenschaften von einer angrenzenden plasmonischen Nanostruktur beeinflusst werden. Das zeige ich für Materialverspannungen und Dotierung in Graphen durch eine Gold-Nanostruktur. Ich habe dafür eine allgemeine Methodik entwickelt, mit der die Beiträge von Verspannung und Dotierung zum Ramanspektrum von Graphen voneinander getrennt und quantifiziert werden können. Diese eignet sich zur Auswertung von unbekannten Verspannungs-Konfigurationen in Graphen auf verschiedensten Substraten.

Acknowledgements

I am deeply grateful to all the people who contributed to the projects of this thesis and provided me with all kinds of help and support. For this I want to express my thanks to...

... first and foremost my supervisor, Stephanie Reich, for guiding, motivating and teaching me throughout all the years I worked on this thesis. Her door was always open for me to come around for countless discussions, in which I received valuable input and in which new ideas were born. I learned from her much more than I could ever list, including how to approach scientific projects and see them in a larger scientific context, write publications, present on conferences, set up collaborations, and also pursue my own ideas. I am deeply grateful for working on such exciting topics that matched my personal interests and also for the family-friendly working environment.

... the current and former members of AG Reich for the numerous discussions, conversations and support in the lab, especially Bruno G. M. Vieira, Valerio Oddone, Patryk Kusch, Sebastian Heeg, Sören Wasserroth, Sabrina Jürgensen, Yu Okamura, Oisín Garrity and Gudrun May-Nasseri.

... the group of Holger Lange at the University of Hamburg for the fruitful collaboration on the plasmonic properties of layered gold nanoparticle films. Special thanks go to Florian Schulz, who performed the synthesis of the nanomaterials.

... Sebastian Heeg, Uwe Hübner, Aravind Vijayaraghavan and Roman Gorbachev for providing the hybrid graphene-plasmonic nanostructure samples.

... Otakar Frank and Miriam Peña Alvarez for their valuable input on the evaluation of strain and doping in graphene and the samples for measuring uniaxial strain.

... Valerio Oddone for helping me construct sample holders and various set ups in the student workshop.

... Oisín Garrity for proofreading this thesis.

... Joachim Heberle for being my second supervisor.

... all other people from the scientific community for the valuable discussions and input, especially Ado Jorio and Eduardo B. Barros.

I am grateful to Deutsche Telekom Stiftung for the financial support with a doctoral scholarship that helped me realize this work. Special thanks go to Christiane Frense-Heck, for the organization of several excellent workshops and meetings that provided me with soft skills and brought me in touch with many other young scientists.

Finally, I want to express my deep gratitude to my wife Feiyan for her steady support and motivation, and for taking care of our kids in the many evenings that I spent on this thesis.

Selbstständigkeitserklärung

Hiermit versichere ich, dass ich alle verwendeten Hilfsmittel und Hilfen angegeben und die vorliegende Arbeit auf dieser Grundlage selbstständig verfasst habe. Diese Arbeit ist nicht schon einmal in einem früheren Promotionsverfahren eingereicht worden.

Berlin, den 09. August 2019, Sven Niclas Tebogo Müller

Bibliography

[1] Novotny, L.; Hecht, B. *Principles of Nano-Optics*, 2nd ed.; Cambridge University Press, 2012.

[2] Koenderink, A. F.; Alù, A.; Polman, A. Nanophotonics: Shrinking light-based technology. *Science* **2015**, *348*, 516–521.

[3] Waldrop, M. M. The chips are down for Moore's law. *Nature* **2016**, *530*, 144–147.

[4] Grundmann, M. *Nano-Optoelectronics: Concepts, Physics and Devices*; NanoScience and Technology; Springer Berlin Heidelberg, 2002.

[5] Maier, S. *Plasmonics - Fundamentals and Applications*; Springer, 2007.

[6] Ru, E. C. L.; Etchegoin, P. G. *Principles of Surface-Enhanced Raman Spectroscopy*; Elsevier: Amsterdam, 2009.

[7] Atwater, H. A.; Polman, A. Plasmonics for improved photovoltaic devices. *Nat. Mater.* **2010**, *9*, 205–213.

[8] Schuller, J. A.; Barnard, E. S.; Cai, W.; Jun, Y. C.; White, J. S.; Brongersma, M. L. Plasmonics for extreme light concentration and manipulation. *Nat. Mater.* **2010**, *9*, 193–204.

[9] Gramotnev, D. K.; Bozhevolnyi, S. I. Plasmonics beyond the diffraction limit. *Nat. Photonics* **2010**, *4*, 83–91.

[10] Halas, N. J.; Lal, S.; Chang, W.-S.; Link, S.; Nordlander, P. Plasmons in Strongly Coupled Metallic Nanostructures. *Chem. Rev.* **2011**, *111*, 3913–3961.

[11] Solis, D.; Willingham, B.; Nauert, S. L.; Slaughter, L. S.; Olson, J.; Swanglap, P.; Paul, A.; Chang, W.-S.; Link, S. Electromagnetic Energy Transport in Nanoparticle Chains via Dark Plasmon Modes. *Nano Lett.* **2012**, *12*, 1349–1353.

[12] Liang, Z.; Sun, J.; Jiang, Y.; Jiang, L.; Chen, X. Plasmonic Enhanced Optoelectronic Devices. *Plasmonics* **2014**, *9*, 859–866.

[13] Sönnichsen, C.; Franzl, T.; Wilk, T.; von Plessen, G.; Feldmann, J.; Wilson, O.; Mulvaney, P. Drastic Reduction of Plasmon Damping in Gold Nanorods. *Phys. Rev. Lett.* **2002**, *88*, 077402.

[14] Hartland, G. V. Optical Studies of Dynamics in Noble Metal Nanostructures. *Chem. Rev.* **2011**, *111*, 3858–3887.

[15] Nordlander, P.; Oubre, C.; Prodan, E.; Li, K.; Stockman, M. I. Plasmon Hybridization in Nanoparticle Dimers. *Nano Lett.* **2004**, *4*, 899–903.

[16] Liu, M.; Lee, T.-W.; Gray, S. K.; Guyot-Sionnest, P.; Pelton, M. Excitation of Dark Plasmons in Metal Nanoparticles by a Localized Emitter. *Phys. Rev. Lett.* **2009**, *102*, 107401.

[17] Chu, M.-W.; Myroshnychenko, V.; Chen, C. H.; Deng, J.-P.; Mou, C.-Y.; García de Abajo, F. J. Probing Bright and Dark Surface-Plasmon Modes in Individual and Coupled Noble Metal Nanoparticles Using an Electron Beam. *Nano Lett.* **2009**, *9*, 399–404.

[18] Gallinet, B.; Martin, O. J. F. Refractive Index Sensing with Subradiant Modes: A Framework To Reduce Losses in Plasmonic Nanostructures. *ACS Nano* **2013**, *7*, 6978–6987.

[19] Sancho-Parramon, J.; Bosch, S. Dark Modes and Fano Resonances in Plasmonic Clusters Excited by Cylindrical Vector Beams. *ACS Nano* **2012**, *6*, 8415–8423.

[20] Hartland, G. V.; Besteiro, L. V.; Johns, P.; Govorov, A. O. Whats so Hot about Electrons in Metal Nanoparticles? *ACS Energy Lett.* **2017**, *2*, 1641–1653.

[21] Brongersma, M. L.; Halas, N. J.; Nordlander, P. Plasmon-induced hot carrier science and technology. *Nat. Nanotechnol.* **2015**, *10*, 25.

[22] Zhang, Y.; He, S.; Guo, W.; Hu, Y.; Huang, J.; Mulcahy, J. R.; Wei, W. D. Surface-Plasmon-Driven Hot Electron Photochemistry. *Chem. Rev.* **2018**, *118*, 2927–2954.

[23] Aizpurua, J. et al. Dynamics of hot electron generation in metallic nanostructures: general discussion. *Faraday Discuss.* **2019**, *214*, 123–146.

[24] Grigorenko, A. N.; Polini, M.; Novoselov, K. S. Graphene plasmonics. *Nat. Photonics* **2012**, *6*, 749–758.

[25] Fang, Z.; Wang, Y.; Liu, Z.; Schlather, A.; Ajayan, P. M.; Koppens, F. H. L.; Nordlander, P.; Halas, N. J. Plasmon-Induced Doping of Graphene. *ACS Nano* **2012**, *6*, 10222–10228.

[26] Hosseini, T.; Kouklin, N. A. On plasmon-induced photocurrent and doping of metal-patterned graphene. *Appl. Phys. Lett.* **2014**, *105*, 043104.

[27] Echtermeyer, T. J.; Nene, P. S.; Trushin, M.; Gorbachev, R. V.; Eiden, A. L.; Milana, S.; Sun, Z.; Schliemann, J.; Lidorikis, E.; Novoselov, K. S.; Ferrari, A. C. Photothermoelectric and Photoelectric Contributions to Light Detection in Metal-Graphene-Metal Photodetectors. *Nano Lett.* **2014**, *14*, 3733–3742.

[28] Jago, R.; Wendler, F.; Malic, E. Microscopic understanding of the photoconduction effect in graphene. *Phys. Rev. B* **2017**, *96*, 085431.

[29] Heeg, S.; Fernandez-Garcia, R.; Oikonomou, A.; Schedin, F.; Narula, R.; Maier, S. A.; Vijayaraghavan, A.; Reich, S. Polarized Plasmonic Enhancement by Au Nanostructures Probed through Raman Scattering of Suspended Graphene. *Nano Lett.* **2013**, *13*, 301–308.

[30] Kneipp, K.; Moskovits, M.; Kneipp, H. *Surface-Enhanced Raman Scattering: Physics and Applications*; Topics in Applied Physics; Springer Berlin Heidelberg, 2006.

[31] Sharma, B.; Frontiera, R. R.; Henry, A.-I.; Ringe, E.; Duyne, R. P. V. SERS: Materials, applications, and the future. *Mater. Today* **2012**, *15*, 16 – 25.

[32] Ding, S.-Y.; You, E.-M.; Tian, Z.-Q.; Moskovits, M. Electromagnetic theories of surface-enhanced Raman spectroscopy. *Chem. Soc. Rev.* **2017**, *46*, 4042–4076.

[33] Nie, S.; Emory, S. R. Probing Single Molecules and Single Nanoparticles by Surface-Enhanced Raman Scattering. *Science* **1997**, *275*, 1102–1106.

[34] Kneipp, K.; Wang, Y.; Kneipp, H.; Perelman, L. T.; Itzkan, I.; Dasari, R. R.; Feld, M. S. Single Molecule Detection Using Surface-Enhanced Raman Scattering (SERS). *Phys. Rev. Lett.* **1997**, *78*, 1667–1670.

[35] Fang, Y.; Seong, N.-H.; Dlott, D. D. Measurement of the Distribution of Site Enhancements in Surface-Enhanced Raman Scattering. *Science* **2008**, *321*, 388–392.

[36] Lim, D.-K.; Jeon, K.-S.; Hwang, J.-H.; Kim, H.; Kwon, S.; Suh, Y. D.; Nam, J.-M. Highly uniform and reproducible surface-enhanced Raman scattering from DNA-tailorable nanoparticles with 1-nm interior gap. *Nat. Nanotechnol.* **2011**, *6*, 452.

[37] de Nijs, B.; Benz, F.; Barrow, S. J.; Sigle, D. O.; Chikkaraddy, R.; Palma, A.; Carnegie, C.; Kamp, M.; Sundararaman, R.; Narang, P.; Scherman, O. A.; Baumberg, J. J. Plasmonic tunnel junctions for single-molecule redox chemistry. *Nat. Commun.* **2017**, *8*, 994.

[38] Zayats, A. V.; Smolyaninov, I. I.; Maradudin, A. A. Nano-optics of surface plasmon polaritons. *Phys. Rep.* **2005**, *408*, 131 – 314.

[39] Agrawal, A.; Cho, S. H.; Zandi, O.; Ghosh, S.; Johns, R. W.; Milliron, D. J. Localized Surface Plasmon Resonance in Semiconductor Nanocrystals. *Chem. Rev.* **2018**, *118*, 3121–3207.

[40] Koppens, F. H. L.; Chang, D. E.; García de Abajo, F. J. Graphene Plasmonics: A Platform for Strong Light-Matter Interactions. *Nano Lett.* **2011**, *11*, 3370–3377.

[41] Low, T.; Avouris, P. Graphene Plasmonics for Terahertz to Mid-Infrared Applications. *ACS Nano* **2014**, *8*, 1086–1101.

[42] Krauter, C. M.; Schirmer, J.; Jacob, C. R.; Pernpointner, M.; Dreuw, A. Plasmons in molecules: Microscopic characterization based on orbital transitions and momentum conservation. *J. Chem. Phys.* **2014**, *141*, 104101.

[43] Lauchner, A.; Schlather, A. E.; Manjavacas, A.; Cui, Y.; McClain, M. J.; Stec, G. J.; García de Abajo, F. J.; Nordlander, P.; Halas, N. J. Molecular Plasmonics. *Nano Lett.* **2015**, *15*, 6208–6214.

[44] Stiles, P. L.; Dieringer, J. A.; Shah, N. C.; Van Duyne, R. P. Surface-Enhanced Raman Spectroscopy. *Annu. Rev. Anal. Chem.* **2008**, *1*, 601–626.

[45] Neubrech, F.; Huck, C.; Weber, K.; Pucci, A.; Giessen, H. Surface-Enhanced Infrared Spectroscopy Using Resonant Nanoantennas. *Chem. Rev.* **2017**, *117*, 5110–5145.

[46] Mayer, K. M.; Hafner, J. H. Localized Surface Plasmon Resonance Sensors. *Chem. Rev.* **2011**, *111*, 3828–3857.

[47] Wei, H.; Pan, D.; Zhang, S.; Li, Z.; Li, Q.; Liu, N.; Wang, W.; Xu, H. Plasmon Waveguiding in Nanowires. *Chem. Rev.* **2018**, *118*, 2882–2926.

[48] Wang, D.; Wang, W.; Knudson, M. P.; Schatz, G. C.; Odom, T. W. Structural Engineering in Plasmon Nanolasers. *Chem. Rev.* **2018**, *118*, 2865–2881.

[49] Zhang, R.; Bursi, L.; Cox, J. D.; Cui, Y.; Krauter, C. M.; Alabastri, A.; Manjavacas, A.; Calzolari, A.; Corni, S.; Molinari, E.; Carter, E. A.; García de Abajo, F. J.; Zhang, H.; Nordlander, P. How To Identify Plasmons from the Optical Response of Nanostructures. *ACS Nano* **2017**, *11*, 7321–7335.

[50] Hohenester, U.; Krenn, J. Surface plasmon resonances of single and coupled metallic nanoparticles: A boundary integral method approach. *Phys. Rev. B* **2005**, *72*, 195429.

[51] Nelayah, J.; Kociak, M.; Stephan, O.; Garcia de Abajo, F. J.; Tence, M.; Henrard, L.; Taverna, D.; Pastoriza-Santos, I.; Liz-Marzan, L. M.; Colliex, C. Mapping surface plasmons on a single metallic nanoparticle. *Nat. Phys.* **2007**, *3*, 348–353.

[52] Hohenester, U.; Trügler, A. MNPBEM: A Matlab toolbox for the simulation of plasmonic nanoparticles. *Comput. Phys. Commun.* **2012**, *183*, 370 – 381.

[53] Crut, A.; Maioli, P.; Del Fatti, N.; Vallée, F. Optical absorption and scattering spectroscopies of single nano-objects. *Chem. Soc. Rev.* **2014**, *43*, 3921–3956.

[54] West, P.; Ishii, S.; Naik, G.; Emani, N.; Shalaev, V.; Boltasseva, A. Searching for better plasmonic materials. *Laser Photonics Rev.* **2010**, *4*, 795–808.

[55] Pinchuk, A.; von Plessen, G.; Kreibig, U. Influence of interband electronic transitions on the optical absorption in metallic nanoparticles. *J. Phys. D* **2004**, *37*, 3133–3139.

[56] Barnes, W. L. Particle plasmons: Why shape matters. *Am. J. Phys* **2016**, *84*, 593–601.

[57] Unger, A.; Kreiter, M. Analyzing the Performance of Plasmonic Resonators for Dielectric Sensing. *J. Phys. Chem. C* **2009**, *113*, 12243–12251.

[58] Jain, P. K.; El-Sayed, M. A. Plasmonic coupling in noble metal nanostructures. *Chem. Phys. Lett.* **2010**, *487*, 153 – 164.

[59] Wang, F.; Shen, Y. R. General Properties of Local Plasmons in Metal Nanostructures. *Phys. Rev. Lett.* **2006**, *97*, 206806.

[60] Mohamed, M. B.; Volkov, V.; Link, S.; El-Sayed, M. A. The 'lightning' gold nanorods: fluorescence enhancement of over a million compared to the gold metal. *Chem. Phys. Lett.* **2000**, *317*, 517 – 523.

[61] Deeb, C.; Zhou, X.; Miller, R.; Gray, S. K.; Marguet, S.; Plain, J.; Wiederrecht, G. P.; Bachelot, R. Mapping the Electromagnetic Near-Field Enhancements of Gold Nanocubes. *J. Phys. Chem. C* **2012**, *116*, 24734–24740.

[62] Nehl, C. L.; Liao, H.; Hafner, J. H. Optical Properties of Star-Shaped Gold Nanoparticles. *Nano Lett.* **2006**, *6*, 683–688.

[63] Zhou, N.; López-Puente, V.; Wang, Q.; Polavarapu, L.; Pastoriza-Santos, I.; Xu, Q.-H. Plasmon-enhanced light harvesting: applications in enhanced photocatalysis, photodynamic therapy and photovoltaics. *RSC Adv.* **2015**, *5*, 29076–29097.

[64] Liu, M.; Pelton, M.; Guyot-Sionnest, P. Reduced damping of surface plasmons at low temperatures. *Phys. Rev. B* **2009**, *79*, 035418.

[65] Johnson, P. B.; Christy, R. W. Optical Constants of the Noble Metals. *Phys. Rev. B* **1972**, *6*, 4370–4379.

[66] Yang, H. U.; D'Archangel, J.; Sundheimer, M. L.; Tucker, E.; Boreman, G. D.; Raschke, M. B. Optical dielectric function of silver. *Phys. Rev. B* **2015**, *91*, 235137.

[67] Zhang, H.; Govorov, A. O. Optical Generation of Hot Plasmonic Carriers in Metal Nanocrystals: The Effects of Shape and Field Enhancement. *J. Phys. Chem. C* **2014**, *118*, 7606–7614.

[68] Harutyunyan, H.; Martinson, A. B. F.; Rosenmann, D.; Khorashad, L. K.; Besteiro, L. V.; Govorov, A. O.; Wiederrecht, G. P. Anomalous ultrafast dynamics of hot plasmonic electrons in nanostructures with hot spots. *Nat. Nanotechnol.* **2015**, *10*, 770.

[69] Sousa-Castillo, A.; Comesaña Hermo, M.; Rodíguez-González, B.; Pérez-Lorenzo, M.; Wang, Z.; Kong, X.-T.; Govorov, A. O.; Correa-Duarte, M. A. Boosting Hot Electron-Driven Photocatalysis through Anisotropic Plasmonic Nanoparticles with Hot Spots in Au-TiO2 Nanoarchitectures. *J. Phys. Chem. C* **2016**, *120*, 11690–11699.

[70] Prodan, E.; Radloff, C.; Halas, N. J.; Nordlander, P. A Hybridization Model for the Plasmon Response of Complex Nanostructures. *Science* **2003**, *302*, 419–422.

[71] Jiang, L.; Yin, T.; Dubrovkin, A. M.; Dong, Z.; Chen, Y.; Chen, W.; Yang, J. K. W.; Shen, Z. In-plane coherent control of plasmon resonances for plasmonic switching and encoding. *Light Science Appl.* **2019**, *8*, 21.

[72] Gómez, D. E.; Teo, Z. Q.; Altissimo, M.; Davis, T. J.; Earl, S.; Roberts, A. The Dark Side of Plasmonics. *Nano Lett.* **2013**, *13*, 3722–3728.

[73] Peyskens, F.; Subramanian, A. Z.; Neutens, P.; Dhakal, A.; Dorpe, P. V.; Thomas, N. L.; Baets, R. Bright and dark plasmon resonances of nanoplasmonic antennas evanescently coupled with a silicon nitride waveguide. *Opt. Express* **2015**, *23*, 3088–3101.

[74] Sakai, K.; Nomura, K.; Yamamoto, T.; Sasaki, K. Excitation of Multipole Plasmons by Optical Vortex Beams. *Sci. Rep.* **2015**, *5*.

[75] Kottmann, J. P.; Martin, O. J. F. Retardation-induced plasmon resonances in coupled nanoparticles. *Opt. Lett.* **2001**, *26*, 1096–1098.

[76] Chang, Y.-C.; Wang, S.-M.; Chung, H.-C.; Tseng, C.-B.; Chang, S.-H. Observation of Absorption-Dominated Bonding Dark Plasmon Mode from Metal-Insulator-Metal Nanodisk Arrays Fabricated by Nanospherical-Lens Lithography. *ACS Nano* **2012**, *6*, 3390–3396.

[77] Pakizeh, T.; Abrishamian, M. S.; Granpayeh, N.; Dmitriev, A.; Käll, M. Magnetic-field enhancement in gold nanosandwiches. *Opt. Express* **2006**, *14*, 8240–8246.

[78] Verre, R.; Yang, Z. J.; Shegai, T.; Käll, M. Optical Magnetism and Plasmonic Fano Resonances in Metal-Insulator-Metal Oligomers. *Nano Lett.* **2015**, *15*, 1952–1958.

[79] Panaro, S.; Nazir, A.; Liberale, C.; Das, G.; Wang, H.; De Angelis, F.; Proietti Zaccaria, R.; Di Fabrizio, E.; Toma, A. Dark to Bright Mode Conversion on Dipolar Nanoantennas: A Symmetry-Breaking Approach. *ACS Photonics* **2014**, *1*, 310–314.

[80] Humphrey, A. D.; Meinzer, N.; Starkey, T. A.; Barnes, W. L. Surface Lattice Resonances in Plasmonic Arrays of Asymmetric Disc Dimers. *ACS Photonics* **2016**, *3*, 634–639.

[81] Chuntonov, L.; Haran, G. Trimeric Plasmonic Molecules: The Role of Symmetry. *Nano Lett.* **2011**, *11*, 2440–2445.

[82] Luk'yanchuk, B.; Zheludev, N. I.; Maier, S. A.; Halas, N. J.; Nordlander, P.; Giessen, H.; Chong, C. T. The Fano resonance in plasmonic nanostructures and metamaterials. *Nat. Mater.* **2010**, *9*, 707–715.

[83] Zhu, W.; Crozier, K. B. Quantum mechanical limit to plasmonic enhancement as observed by surface-enhanced Raman scattering. *Nat. Commun.* **2014**, *5*.

[84] Zhu, W.; Banaee, M. G.; Wang, D.; Chu, Y.; Crozier, K. B. Lithographically Fabricated Optical Antennas with Gaps Well Below 10 nm. *Small* **2011**, *7*, 1761–1766.

[85] Hentschel, M.; Saliba, M.; Vogelgesang, R.; Giessen, H.; Alivisatos, A. P.; Liu, N. Transition from Isolated to Collective Modes in Plasmonic Oligomers. *Nano Lett.* **2010**, *10*, 2721–2726.

[86] Fan, J. A.; Wu, C.; Bao, K.; Bao, J.; Bardhan, R.; Halas, N. J.; Manoharan, V. N.; Nordlander, P.; Shvets, G.; Capasso, F. Self-Assembled Plasmonic Nanoparticle Clusters. *Science* **2010**, *328*, 1135–1138.

[87] Lu, X.; Rycenga, M.; Skrabalak, S. E.; Wiley, B.; Xia, Y. Chemical Synthesis of Novel Plasmonic Nanoparticles. *Annu. Rev. Phys. Chem.* **2009**, *60*, 167–192.

[88] Romo-Herrera, J. M.; Alvarez-Puebla, R. A.; Liz-Marzán, L. M. Controlled assembly of plasmonic colloidal nanoparticle clusters. *Nanoscale* **2011**, *3*, 1304–1315.

[89] Schulz, F.; Tober, S.; Lange, H. Size-Dependent Phase Transfer Functionalization of Gold Nanoparticles To Promote Well-Ordered Self-Assembly. *Langmuir* **2017**, *33*, 14437–14444.

[90] Lee, Y.-J.; Schade, N. B.; Sun, L.; Fan, J. A.; Bae, D. R.; Mariscal, M. M.; Lee, G.; Capasso, F.; Sacanna, S.; Manoharan, V. N.; Yi, G.-R. Ultrasmooth, Highly Spherical Monocrystalline Gold Particles for Precision Plasmonics. *ACS Nano* **2013**, *7*, 11064–11070.

[91] Barrow, S. J.; Wei, X.; Baldauf, J. S.; Funston, A. M.; Mulvaney, P. The surface plasmon modes of self-assembled gold nanocrystals. *Nat. Commun.* **2012**, *3*.

[92] Gallinet, B.; Butet, J.; Martin, O. J. F. Numerical methods for nanophotonics: standard problems and future challenges. *Laser Photonics Rev.* **2015**, *9*, 577–603.

[93] Yu, R.; Liz-Marzán, L. M.; García de Abajo, F. J. Universal analytical modeling of plasmonic nanoparticles. *Chem. Soc. Rev.* **2017**, *46*, 6710–6724.

[94] Solís, D. M.; Taboada, J. M.; Obelleiro, F.; Liz-Marzán, L. M.; García de Abajo, F. J. Toward Ultimate Nanoplasmonics Modeling. *ACS Nano* **2014**, *8*, 7559–7570.

[95] Bohren, C.; Huffman, D. R. In *Absorption and Scattering of Light by Small Particles*; Bohren, C., Huffman, D. R., Eds.; Wiley Science Paperback Series, 1998.

[96] Etchegoin, P. G.; Le Ru, E. C.; Meyer, M. An analytic model for the optical properties of gold. *J. Chem. Phys.* **2006**, *125*, 164705.

[97] Kravets, V. G.; Kabashin, A. V.; Barnes, W. L.; Grigorenko, A. N. Plasmonic Surface Lattice Resonances: A Review of Properties and Applications. *Chem. Rev.* **2018**, *118*, 5912–5951.

[98] Kahnert, F. Numerical methods in electromagnetic scattering theory. *J Quant. Spectrosc. Ra.* **2003**, *79-80*, 775 – 824, Electromagnetic and Light Scattering by Non-Spherical Particles.

[99] Taflove, A.; Hagness, S. C. *Computational electrodynamics: the finite-difference time-domain method*, 3rd ed.; Artech House: Norwood, 2005.

[100] Montgomery, J. M.; Lee, T.-W.; Gray, S. K. Theory and modeling of light interactions with metallic nanostructures. *J. Phys. Condens. Matter* **2008**, *20*, 323201.

[101] Jin, J. *The Finite Element Method in Electromagnetics*, 3rd ed.; Wiley-IEEE Press, 2014.

[102] Yurkin, M.; Hoekstra, A. The discrete dipole approximation: An overview and recent developments. *J Quant. Spectrosc. Ra.* **2007**, *106*, 558 – 589, IX Conference on Electromagnetic and Light Scattering by Non-Spherical Particles.

[103] Kern, A. M.; Martin, O. J. F. Surface integral formulation for 3D simulations of plasmonic and high permittivity nanostructures. *J Opt. Soc. Am. A* **2009**, *26*, 732–740.

[104] García de Abajo, F. J.; Howie, A. Retarded field calculation of electron energy loss in inhomogeneous dielectrics. *Phys. Rev. B* **2002**, *65*, 115418.

[105] Busch, K.; König, M.; Niegemann, J. Discontinuous Galerkin methods in nanophotonics. *Laser Photonics Rev.* **2011**, *5*, 773–809.

[106] Kane Yee, Numerical solution of initial boundary value problems involving maxwell's equations in isotropic media. *IEEE T. Antenn. Propag.* **1966**, *14*, 302–307.

[107] Remis, R. F. On the relation between FDTD and Fibonacci polynomials. *J. Comput. Phys.* **2011**, *230*, 1382 – 1386.

[108] Monk, P.; Suli, E. Error estimates for Yee's method on non-uniform grids. *IEEE Trans. Magn* **1994**, *30*, 3200–3203.

[109] Wenhua Yu,; Mittra, R. A conformal finite difference time domain technique for modeling curved dielectric surfaces. *IEEE Microw. Wirel Co.* **2001**, *11*, 25–27.

[110] Finite-difference time-domain method on Wikipedia. https://en.wikipedia.org/wiki/Finite-difference_time-domain_method, Accessed: 2019-05-12.

[111] Anantha, V.; Taflove, A. Efficient modeling of infinite scatterers using a generalized total-field/scattered-field FDTD boundary partially embedded within PML. *IEEE T. Antenn. Propag.* **2002**, *50*, 1337–1349.

[112] Chen, P.; Xu, X.; Zeng, Q.; Yagoub, M. C. E. Total-field scattered-field plane wave sources for FDTD analysis of stratified lossy dispersive media. 2012 IEEE International Symposium on Electromagnetic Compatibility. 2012; pp 498–503.

[113] Berenger, J.-P. A perfectly matched layer for the absorption of electromagnetic waves. *J. Comput. Phys.* **1994**, *114*, 185 – 200.

[114] Chew, W. C.; Weedon, W. H. A 3D perfectly matched medium from modified maxwell's equations with stretched coordinates. *Microw. Opt. Techn. Let.* **1994**, *7*, 599–604.

[115] Kelley, D. F.; Luebbers, R. J. Piecewise linear recursive convolution for dispersive media using FDTD. *IEEE T. Antenn. Propag.* **1996**, *44*, 792–797.

[116] Okoniewski, M.; Mrozowski, M.; Stuchly, M. A. Simple treatment of multi-term dispersion in FDTD. *IEEE Microw. Wirel. Compon. Lett* **1997**, *7*, 121–123.

[117] García de Abajo, F. J.; Howie, A. Relativistic Electron Energy Loss and Electron-Induced Photon Emission in Inhomogeneous Dielectrics. *Phys. Rev. Lett.* **1998**, *80*, 5180–5183.

[118] Waxenegger, J.; Trügler, A.; Hohenester, U. Plasmonics simulations with the MNPBEM toolbox: Consideration of substrates and layer structures. *Comput. Phys. Commun* **2015**, *193*, 138 – 150.

[119] Trügler, A. Optical properties of metallic nanoparticles. dissertation, Department of Physics, Karl-Franzens-Universität Graz, 2011.

[120] Trügler, A.; Tinguely, J.-C.; Jakopic, G.; Hohenester, U.; Krenn, J. R.; Hohenau, A. Near-field and SERS enhancement from rough plasmonic nanoparticles. *Phys. Rev. B* **2014**, *89*, 165409.

[121] Myroshnychenko, V.; Carbó-Argibay, E.; Pastoriza-Santos, I.; Pérez-Juste, J.; Liz-Marzán, L. M.; García de Abajo, F. J. Modeling the Optical Response of Highly Faceted Metal Nanoparticles with a Fully 3D Boundary Element Method. *Adv. Mater.* **2008**, *20*, 4288–4293.

[122] Kern, A. M.; Martin, O. J. F. Excitation and Reemission of Molecules near Realistic Plasmonic Nanostructures. *Nano Lett.* **2011**, *11*, 482–487.

[123] Butet, J.; Thyagarajan, K.; Martin, O. J. F. Ultrasensitive Optical Shape Characterization of Gold Nanoantennas Using Second Harmonic Generation. *Nano Lett.* **2013**, *13*, 1787–1792.

[124] Yu, P. Y.; Cardona, M. *Fundamentals of Semiconductors: Physics and Materials Properties*, 4th ed.; Springer: Berlin, 2010.

[125] Long, D. A. *The Raman Effect*; John Wiley & Sons, Ltd, 2002.

[126] Nakanishi, K.; Solomon, P. *Infrared Absorption Spectroscopy*; Emerson-Adams Press, 1977.

[127] Reich, S.; Thomsen, C.; Maultzsch, J. *Carbon Nanotubes: Basic Concepts and Physical Properties*; Wiley, 2004.

[128] Meyer, S. A.; Ru, E. C. L.; Etchegoin, P. G. Quantifying Resonant Raman Cross Sections with SERS. *J. Phys. Chem. A* **2010**, *114*, 5515–5519.

[129] Gaufrès, E.; Tang, N. Y. W.; Lapointe, F.; Cabana, J.; Nadon, M.-A.; Cottenye, N.; Raymond, F.; Szkopek, T.; Martel, R. Giant Raman scattering from J-aggregated dyes inside carbon nanotubes for multispectral imaging. *Nat. Photonics* **2013**, *8*, 72.

[130] Wei, D.; Chen, S.; Liu, Q. Review of Fluorescence Suppression Techniques in Raman Spectroscopy. *Appl. Spectrosc. Rev.* **2015**, *50*, 387–406.

[131] Dresselhaus, M.; Dresselhaus, G.; Jorio, A. *Group Theory: Application to the Physics of Condensed Matter*; Springer Berlin Heidelberg, 2007.

[132] Placzek, G. *Rayleigh-Streuung und Raman-Effekt*; Handbuch der Radiologie; Akad. Verlag-Ges., 1934.

[133] Loudon, R.; Kurti, N. Theory of the first-order Raman effect in crystals. *P. Roy. Soc. Lond. A Mat.* **1963**, *275*, 218–232.

[134] Martin, R. M.; Falicov, L. M. In *Light Scattering in Solids*; Cardona, M., Ed.; Springer Berlin Heidelberg: Berlin, Heidelberg, 1975; pp 79–145.

[135] Jin, B.-Y.; Silbey, R. Theory of resonance Raman scattering for finite and infinite polyenes. *J. Chem. Phys.* **1995**, *102*, 4251–4260.

[136] Jimenez-Sandoval, S. Micro-Raman spectroscopy: a powerful technique for materials research. *Microelectron. J.* **2000**, *31*, 419 – 427.

[137] McCreery, R. L. CCD Array Detectors for Multichannel Raman Spectroscopy. Charge-transfer Devices in Spectroscopy. 1994; p 227.

[138] Wall, K.; Sanchez, A. Titanium sapphire lasers. *Lincoln Laboratory Journal; (USA)* **1990**, *3*.

[139] Duarte, F. J.; Hillman, L. W.; Liao, P. F.; Kelley, P. *Dye laser principles: with applications*; Quantum Electronics–Principles and Applications; Academic Press: New York, 1990.

[140] Sperling, J.; Hens, K. Made Easy: CW Laser Light Widely Tunable Across the Visible. *Optik & Photonik* **2018**, *13*, 22–24.

[141] Fleischmann, M.; Hendra, P.; McQuillan, A. Raman spectra of pyridine adsorbed at a silver electrode. *Chem. Phys. Lett.* **1974**, *26*, 163 – 166.

[142] Jensen, L.; Aikens, C. M.; Schatz, G. C. Electronic structure methods for studying surface-enhanced Raman scattering. *Chem. Soc. Rev.* **2008**, *37*, 1061–1073.

[143] Morton, S. M.; Silverstein, D. W.; Jensen, L. Theoretical Studies of Plasmonics using Electronic Structure Methods. *Chem. Rev.* **2011**, *111*, 3962–3994.

[144] Lombardi, J. R.; Birke, R. L.; Lu, T.; Xu, J. Charge-transfer theory of surface enhanced Raman spectroscopy: Herzberg-Teller contributions. *J. Chem. Phys.* **1986**, *84*, 4174–4180.

[145] Osawa, M.; Matsuda, N.; Yoshii, K.; Uchida, I. Charge transfer resonance Raman process in surface-enhanced Raman scattering from p-aminothiophenol adsorbed on silver: Herzberg-Teller contribution. *J. Phys. Chem.* **1994**, *98*, 12702–12707.

[146] Morton, S. M.; Jensen, L. Understanding the Molecule-Surface Chemical Coupling in SERS. *JACS* **2009**, *131*, 4090–4098.

[147] Darby, B. L.; Auguié, B.; Meyer, M.; Pantoja, A. E.; Le Ru, E. C. Modified optical absorption of molecules on metallic nanoparticles at sub-monolayer coverage. *Nat. Photonics* **2016**, *10*, 40–45.

[148] Valley, N.; Greeneltch, N.; Van Duyne, R. P.; Schatz, G. C. A Look at the Origin and Magnitude of the Chemical Contribution to the Enhancement Mechanism of Surface-Enhanced Raman Spectroscopy (SERS): Theory and Experiment. *J. Phys. Chem. Lett.* **2013**, *4*, 2599–2604.

[149] Chen, H.; McMahon, J. M.; Ratner, M. A.; Schatz, G. C. Classical Electrodynamics Coupled to Quantum Mechanics for Calculation of Molecular Optical Properties: a RT-TDDFT/FDTD Approach. *J. Phys. Chem. C* **2010**, *114*, 14384–14392.

[150] Carnegie, C.; Griffiths, J.; de Nijs, B.; Readman, C.; Chikkaraddy, R.; Deacon, W. M.; Zhang, Y.; Szabó, I.; Rosta, E.; Aizpurua, J.; Baumberg, J. J. Room-Temperature Optical Picocavities below 1 nm^3 Accessing Single-Atom Geometries. *J. Phys. Chem. Lett.* **2018**, *9*, 7146–7151.

[151] Mueller, N. S.; Heeg, S.; Kusch, P.; Gaufrès, E.; Tang, N. Y.-W.; Hübner, U.; Martel, R.; Vijayaraghavan, A.; Reich, S. Plasmonic enhancement of SERS measured on molecules in carbon nanotubes. *Faraday Discuss.* **2017**, *205*, 85–103.

[152] Wustholz, K. L.; Henry, A.-I.; McMahon, J. M.; Freeman, R. G.; Valley, N.; Piotti, M. E.; Natan, M. J.; Schatz, G. C.; Van Duyne, R. P. Structure-Activity Relationships in Gold Nanoparticle Dimers and Trimers for Surface-Enhanced Raman Spectroscopy. *JACS* **2010**, *132*, 10903–10910.

[153] Benz, F.; Schmidt, M. K.; Dreismann, A.; Chikkaraddy, R.; Zhang, Y.; Demetriadou, A.; Carnegie, C.; Ohadi, H.; de Nijs, B.; Esteban, R.; Aizpurua, J.; Baumberg, J. J. Single-molecule optomechanics in "picocavities". *Science* **2016**, *354*, 726–729.

[154] Heeg, S.; Oikonomou, A.; Fernandez-Garcia, R.; Lehmann, C.; Maier, S. A.; Vijayaraghavan, A.; Reich, S. Plasmon-Enhanced Raman Scattering by Carbon Nanotubes Optically Coupled with Near-Field Cavities. *Nano Lett.* **2014**, *14*, 1762–1768.

[155] Wasserroth, S.; Heeg, S.; Mueller, N. S.; Kusch, P.; Hübner, U.; Gaufrès, E.; Tang, N. Y.-W.; Martel, R.; Vijayaraghavan, A.; Reich, S. Resonant, Plasmonic Raman Enhancement of α-6T Molecules Encapsulated in Carbon Nanotubes. *J. Phys. Chem. C* **2019**, *123*, 10578–10585.

[156] Wasserroth, S.; Bisswanger, T.; Mueller, N. S.; Kusch, P.; Heeg, S.; Clark, N.; Schedin, F.; Gorbachev, R.; Reich, S. Graphene as a local probe to investigate near-field properties of plasmonic nanostructures. *Phys. Rev. B* **2018**, *97*, 155417.

[157] Novoselov, K. S.; Geim, A. K.; Morozov, S. V.; Jiang, D.; Zhang, Y.; Dubonos, S. V.; Grigorieva, I. V.; Firsov, A. A. Electric field effect in atomically thin carbon films. *Science* **2004**, *306*, 666–669.

[158] Torres, L.; Roche, S.; Charlier, J. *Introduction to Graphene-Based Nanomaterials: From Electronic Structure to Quantum Transport*; Introduction to Graphene-based Nanomaterials: From Electronic Structure to Quantum Transport; Cambridge University Press, 2014.

[159] Novoselov, K. S.; Fal'ko, V. I.; Colombo, L.; Gellert, P. R.; Schwab, M. G.; Kim, K. A roadmap for graphene. *Nature* **2012**, *490*, 192.

[160] Novoselov, K. S.; Geim, A. K.; Morozov, S. V.; Jiang, D.; Katsnelson, M. I.; Grigorieva, I. V.; Dubonos, S. V.; Firsov, A. A. Two-dimensional gas of massless Dirac fermions in graphene. *Nature* **2005**, *438*, 197.

[161] Morozov, S. V.; Novoselov, K. S.; Katsnelson, M. I.; Schedin, F.; Elias, D. C.; Jaszczak, J. A.; Geim, A. K. Giant Intrinsic Carrier Mobilities in Graphene and Its Bilayer. *Phys. Rev. Lett.* **2008**, *100*, 016602.

[162] Bolotin, K.; Sikes, K.; Jiang, Z.; Klima, M.; Fudenberg, G.; Hone, J.; Kim, P.; Stormer, H. Ultrahigh electron mobility in suspended graphene. *Solid State Commun.* **2008**, *146*, 351 – 355.

[163] Baringhaus, J.; Ruan, M.; Edler, F.; Tejeda, A.; Sicot, M.; Taleb-Ibrahimi, A.; Li, A.-P.; Jiang, Z.; Conrad, E. H.; Berger, C.; Tegenkamp, C.; de Heer, W. A. Exceptional ballistic transport in epitaxial graphene nanoribbons. *Nature* **2014**, *506*, 349.

[164] Nair, R. R.; Blake, P.; Grigorenko, A. N.; Novoselov, K. S.; Booth, T. J.; Stauber, T.; Peres, N. M. R.; Geim, A. K. Fine structure constant defines visual transparency of graphene. *Science* **2008**, *320*, 1308.

[165] Mak, K. F.; Sfeir, M. Y.; Wu, Y.; Lui, C. H.; Misewich, J. A.; Heinz, T. F. Measurement of the Optical Conductivity of Graphene. *Phys. Rev. Lett.* **2008**, *101*, 196405.

[166] Lee, C. G.; Wei, X. D.; Kysar, J. W.; Hone, J. Measurement of the elastic properties and intrinsic strength of monolayer graphene. *Science* **2008**, *321*, 385–388.

[167] Galiotis, C.; Frank, O.; Koukaras, E. N.; Sfyris, D. Graphene Mechanics: Current Status and Perspectives. *Annu. Rev. Chem. Biomol. Eng.* **2015**, *6*, 121–140.

[168] Nicholl, R. J. T.; Conley, H. J.; Lavrik, N. V.; Vlassiouk, I.; Puzyrev, Y. S.; Sreenivas, V. P.; Pantelides, S. T.; Bolotin, K. I. The effect of intrinsic crumpling on the mechanics of free-standing graphene. *Nat. Commun.* **2015**, *6*, 8789.

[169] Wallace, P. R. The Band Theory of Graphite. *Phys. Rev.* **1947**, *71*, 622–634.

[170] Lherbier, A.; Dubois, S. M.-M.; Declerck, X.; Niquet, Y.-M.; Roche, S.; Charlier, J.-C. Transport properties of graphene containing structural defects. *Phys. Rev. B* **2012**, *86*, 075402.

[171] Reich, S.; Maultzsch, J.; Thomsen, C.; Ordejon, P. Tight-binding description of graphene. *Phys. Rev. B* **2002**, *66*.

[172] Mak, K. F.; da Jornada, F. H.; He, K.; Deslippe, J.; Petrone, N.; Hone, J.; Shan, J.; Louie, S. G.; Heinz, T. F. Tuning Many-Body Interactions in Graphene: The Effects of Doping on Excitons and Carrier Lifetimes. *Phys. Rev. Lett.* **2014**, *112*, 207401.

[173] Bostwick, A.; Ohta, T.; Seyller, T.; Horn, K.; Rotenberg, E. Quasiparticle dynamics in graphene. *Nat. Phys.* **2006**, *3*, 36.

[174] Castro Neto, A. H.; Guinea, F.; Peres, N. M. R.; Novoselov, K. S.; Geim, A. K. The electronic properties of graphene. *Rev. Mod. Phys.* **2009**, *81*, 109–162.

[175] Rycerz, A.; Tworzydlo, J.; Beenakker, C. W. J. Valley filter and valley valve in graphene. *Nat. Phys.* **2007**, *3*, 172.

[176] Schaibley, J. R.; Yu, H.; Clark, G.; Rivera, P.; Ross, J. S.; Seyler, K. L.; Yao, W.; Xu, X. Valleytronics in 2D Mater. *Nat. Rev. Mater.* **2016**, *1*, 16055.

[177] Katsnelson, M. I. *Graphene: Carbon in Two Dimensions*; Cambridge University Press, 2012; pp 161–184.

[178] Binder, R. *Optical properties of graphene*; World Scientific Publishing Co. Pte. Ltd., 2017.

[179] Liu, Y.; Cheng, R.; Liao, L.; Zhou, H.; Bai, J.; Liu, G.; Liu, L.; Huang, Y.; Duan, X. Plasmon resonance enhanced multicolour photodetection by graphene. *Nat. Commun.* **2011**, *2*.

[180] Echtermeyer, T. J.; Britnell, L.; Jasnos, P. K.; Lombardo, A.; Gorbachev, R. V.; Grigorenko, A. N.; Geim, A. K.; Ferrari, A. C.; Novoselov, K. S. Strong plasmonic enhancement of photovoltage in graphene. *Nat. Commun.* **2011**, *2*.

[181] Fang, Z.; Liu, Z.; Wang, Y.; Ajayan, P. M.; Nordlander, P.; Halas, N. J. Graphene-Antenna Sandwich Photodetector. *Nano Lett.* **2012**, *12*, 3808–3813.

[182] Malard, L.; Pimenta, M.; Dresselhaus, G.; Dresselhaus, M. Raman spectroscopy in graphene. *Phys. Rep.* **2009**, *473*, 51 – 87.

[183] Ferrari, A. C.; Basko, D. M. Raman spectroscopy as a versatile tool for studying the properties of graphene. *Nat. Nanotechnol.* **2013**, *8*, 235.

[184] Lazzeri, M.; Attaccalite, C.; Wirtz, L.; Mauri, F. Impact of the electron-electron correlation on phonon dispersion: Failure of LDA and GGA DFT functionals in graphene and graphite. *Phys. Rev. B* **2008**, *78*, 081406.

[185] Venezuela, P.; Lazzeri, M.; Mauri, F. Theory of double-resonant Raman spectra in graphene: Intensity and line shape of defect-induced and two-phonon bands. *Phys. Rev. B* **2011**, *84*, 035433.

[186] Mueller, N. S.; Morfa, A. J.; Abou-Ras, D.; Oddone, V.; Ciuk, T.; Giersig, M. Growing graphene on polycrystalline copper foils by ultra-high vacuum chemical vapor deposition. *Carbon* **2014**, *78*, 347 – 355.

[187] Ferrari, A. C.; Meyer, J. C.; Scardaci, V.; Casiraghi, C.; Lazzeri, M.; Mauri, F.; Piscanec, S.; Jiang, D.; Novoselov, K. S.; Roth, S.; Geim, A. K. Raman Spectrum of Graphene and Graphene Layers. *Phys. Rev. Lett.* **2006**, *97*, 187401.

[188] Tuinstra, F.; L., K. J. Raman Spectrum of Graphite. *J. Chem. Phys.* **1970**, *53*, 1126–1130.

[189] Basko, D. M. Calculation of the Raman G peak intensity in monolayer graphene: role of Ward identities. *New J. Phys.* **2009**, *11*, 095011.

[190] Reichardt, S.; Wirtz, L. Ab initio calculation of the G peak intensity of graphene: Laser-energy and Fermi-energy dependence and importance of quantum interference effects. *Phys. Rev. B* **2017**, *95*, 195422.

[191] Thomsen, C.; Reich, S. Double Resonant Raman Scattering in Graphite. *Phys. Rev. Lett.* **2000**, *85*, 5214–5217.

[192] Narula, R.; Reich, S. Double resonant Raman spectra in graphene and graphite: A two-dimensional explanation of the Raman amplitude. *Phys. Rev. B* **2008**, *78*, 165422.

[193] Cançado, L. G.; Jorio, A.; Ferreira, E. H. M.; Stavale, F.; Achete, C. A.; Capaz, R. B.; Moutinho, M. V. O.; Lombardo, A.; Kulmala, T. S.; Ferrari, A. C. Quantifying Defects in Graphene via Raman Spectroscopy at Different Excitation Energies. *Nano Lett.* **2011**, *11*, 3190–3196.

[194] Eckmann, A.; Felten, A.; Mishchenko, A.; Britnell, L.; Krupke, R.; Novoselov, K. S.; Casiraghi, C. Probing the Nature of Defects in Graphene by Raman Spectroscopy. *Nano Lett.* **2012**, *12*, 3925–3930.

[195] Narula, R.; Reich, S. Probing LO phonons of graphene under tension via the $2D'$ Raman mode. *Phys. Rev. B* **2013**, *87*, 115424.

[196] Das, A.; Pisana, S.; Chakraborty, B.; Piscanec, S.; Saha, S. K.; Waghmare, U. V.; Novoselov, K. S.; Krishnamurthy, H. R.; Geim, A. K.; Ferrari, A. C.; Sood, A. K. Monitoring dopants by Raman scattering in an electrochemically top-gated graphene transistor. *Nat. Nanotechnol.* **2008**, *3*, 210.

[197] Zabel, J.; Nair, R. R.; Ott, A.; Georgiou, T.; Geim, A. K.; Novoselov, K. S.; Casiraghi, C. Raman Spectroscopy of Graphene and Bilayer under Biaxial Strain: Bubbles and Balloons. *Nano Lett.* **2012**, *12*, 617–621.

[198] Mohiuddin, T. M. G.; Lombardo, A.; Nair, R. R.; Bonetti, A.; Savini, G.; Jalil, R.; Bonini, N.; Basko, D. M.; Galiotis, C.; Marzari, N.; Novoselov, K. S.; Geim, A. K.; Ferrari, A. C. Uniaxial strain in graphene by Raman spectroscopy: G peak splitting, Grüneisen parameters, and sample orientation. *Phys. Rev. B* **2009**, *79*, 205433.

[199] Froehlicher, G.; Berciaud, S. Raman spectroscopy of electrochemically gated graphene transistors: Geometrical capacitance, electron-phonon, electron-electron, and electron-defect scattering. *Phys. Rev. B* **2015**, *91*, 205413.

[200] Piscanec, S.; Lazzeri, M.; Mauri, F.; Ferrari, A. C.; Robertson, J. Kohn Anomalies and Electron-Phonon Interactions in Graphite. *Phys. Rev. Lett.* **2004**, *93*, 185503.

[201] Lazzeri, M.; Mauri, F. Nonadiabatic Kohn Anomaly in a Doped Graphene Monolayer. *Phys. Rev. Lett.* **2006**, *97*, 266407.

[202] Pisana, S.; Lazzeri, M.; Casiraghi, C.; Novoselov, K. S.; Geim, A. K.; Ferrari, A. C.; Mauri, F. Breakdown of the adiabatic Born-Oppenheimer approximation in graphene. *Nat. Mater.* **2007**, *6*, 198.

[203] Huang, M.; Yan, H.; Chen, C.; Song, D.; Heinz, T. F.; Hone, J. Phonon softening and crystallographic orientation of strained graphene studied by Raman spectroscopy. *PNAS* **2009**, *106*, 7304–7308.

[204] Reich, S.; Jantoljak, H.; Thomsen, C. Shear strain in carbon nanotubes under hydrostatic pressure. *Phys. Rev. B* **2000**, *61*, R13389–R13392.

[205] Metten, D.; Federspiel, F.; Romeo, M.; Berciaud, S. All-Optical Blister Test of Suspended Graphene Using Micro-Raman Spectroscopy. *Phys. Rev. Applied* **2014**, *2*, 054008.

[206] Mohr, M.; Maultzsch, J.; Thomsen, C. Splitting of the Raman 2D band of graphene subjected to strain. *Phys. Rev. B* **2010**, *82*, 201409.

[207] Frank, O.; Mohr, M.; Maultzsch, J.; Thomsen, C.; Riaz, I.; Jalil, R.; Novoselov, K. S.; Tsoukleri, G.; Parthenios, J.; Papagelis, K.; Kavan, L.; Galiotis, C. Raman 2D-Band Splitting in Graphene: Theory and Experiment. *ACS Nano* **2011**, *5*, 2231–2239.

[208] Lee, J. E.; Ahn, G.; Shim, J.; Lee, Y. S.; Ryu, S. Optical separation of mechanical strain from charge doping in graphene. *Nat. Commun.* **2012**, *3*.

[209] Jorio, A.; Mueller, N. S.; Reich, S. Symmetry-derived selection rules for plasmon-enhanced Raman scattering. *Phys. Rev. B* **2017**, *95*, 155409.

[210] Lau, C. Y.; Duan, H.; Wang, F.; He, C. B.; Low, H. Y.; Yang, J. K. W. Enhanced Ordering in Gold Nanoparticles Self-Assembly through Excess Free Ligands. *Langmuir* **2011**, *27*, 3355–3360.

[211] Hamon, C.; Novikov, S. M.; Scarabelli, L.; Solís, D. M.; Altantzis, T.; Bals, S.; Taboada, J. M.; Obelleiro, F.; Liz-Marzán, L. M. Collective Plasmonic Properties in Few-Layer Gold Nanorod Supercrystals. *ACS Photonics* **2015**, *2*, 1482–1488.

[212] Ye, X.; Zhu, C.; Ercius, P.; Raja, S. N.; He, B.; Jones, M. R.; Hauwiller, M. R.; Liu, Y.; Xu, T.; Alivisatos, A. P. Structural diversity in binary superlattices self-assembled from polymer-grafted nanocrystals. *Nat. Commun.* **2015**, *6*, 10052.

[213] Novo, C.; Gomez, D.; Perez-Juste, J.; Zhang, Z.; Petrova, H.; Reismann, M.; Mulvaney, P.; Hartland, G. V. Contributions from radiation damping and surface scattering to the linewidth of the longitudinal plasmon band of gold nanorods: a single particle study. *Phys. Chem. Chem. Phys.* **2006**, *8*, 3540–3546.

[214] Berciaud, S.; Cognet, L.; Tamarat, P.; Lounis, B. Observation of Intrinsic Size Effects in the Optical Response of Individual Gold Nanoparticles. *Nano Lett.* **2005**, *5*, 515–518.

[215] Minutella, E.; Schulz, F.; Lange, H. Excitation-Dependence of Plasmon-Induced Hot Electrons in Gold Nanoparticles. *J. Phys. Chem. Lett.* **2017**, *8*, 4925–4929.

[216] Moreau, A.; Ciracì, C.; Mock, J. J.; Hill, R. T.; Wang, Q.; Wiley, B. J.; Chilkoti, A.; Smith, D. R. Controlled-reflectance surfaces with film-coupled colloidal nanoantennas. *Nature* **2012**, *492*, 86.

[217] Ng, C.; Cadusch, J. J.; Dligatch, S.; Roberts, A.; Davis, T. J.; Mulvaney, P.; Gómez, D. E. Hot Carrier Extraction with Plasmonic Broadband Absorbers. *ACS Nano* **2016**, *10*, 4704–4711.

[218] Xia, F.; Wang, H.; Xiao, D.; Dubey, M.; Ramasubramaniam, A. Two-dimensional material nanophotonics. *Nat. Photonics* **2014**, *8*, 899.

[219] Zhang, W.; Wang, Q.; Chen, Y.; Wang, Z.; Wee, A. T. S. Van der Waals stacked 2D layered materials for optoelectronics. *2D Mater.* **2016**, *3*, 022001.

[220] Cheng, J.; Wang, C.; Zou, X.; Liao, L. Recent Advances in Optoelectronic Devices Based on 2D Mater. and Their Heterostructures. *Adv. Opt. Mater.* **2019**, *7*, 1800441.

[221] Geim, A. K.; Grigorieva, I. V. Van der Waals heterostructures. *Nature* **2013**, *499*, 419.

[222] Sun, Z.; Martinez, A.; Wang, F. Optical modulators with 2D layered materials. *Nat. Photonics* **2016**, *10*, 227.

[223] Liu, Z.; Lau, S. P.; Yan, F. Functionalized graphene and other two-dimensional materials for photovoltaic devices: device design and processing. *Chem. Soc. Rev.* **2015**, *44*, 5638–5679.

[224] Li, Y.; Li, Z.; Chi, C.; Shan, H.; Zheng, L.; Fang, Z. Plasmonics of 2D Nanomaterials: Properties and Applications. *Adv. Sci.* **2017**, *4*, 1600430.

[225] Grüneis, A.; Saito, R.; Samsonidze, G. G.; Kimura, T.; Pimenta, M. A.; Jorio, A.; Souza Filho, A. G.; Dresselhaus, G.; Dresselhaus, M. S. Inhomogeneous optical absorption around the K point in graphite and carbon nanotubes. *Phys. Rev. B* **2003**, *67*, 165402.

[226] Malic, E.; Winzer, T.; Bobkin, E.; Knorr, A. Microscopic theory of absorption and ultrafast many-particle kinetics in graphene. *Phys. Rev. B* **2011**, *84*, 205406.

[227] Mittendorff, M.; Winzer, T.; Malic, E.; Knorr, A.; Berger, C.; de Heer, W. A.; Schneider, H.; Helm, M.; Winnerl, S. Anisotropy of Excitation and Relaxation of Photogenerated Charge Carriers in Graphene. *Nano Lett.* **2014**, *14*, 1504–1507.

[228] Yan, X.-Q.; Yao, J.; Liu, Z.-B.; Zhao, X.; Chen, X.-D.; Gao, C.; Xin, W.; Chen, Y.; Tian, J.-G. Evolution of anisotropic-to-isotropic photoexcited carrier distribution in graphene. *Phys. Rev. B* **2014**, *90*, 134308.

[229] Li, J.-F.; Li, C.-Y.; Aroca, R. F. Plasmon-enhanced fluorescence spectroscopy. *Chem. Soc. Rev.* **2017**, *46*, 3962–3979.

[230] Moskovits, M. Persistent misconceptions regarding SERS. *Phys. Chem. Chem. Phys.* **2013**, *15*, 5301–5311.

[231] Schmidt, M. K.; Esteban, R.; González-Tudela, A.; Giedke, G.; Aizpurua, J. Quantum Mechanical Description of Raman Scattering from Molecules in Plasmonic Cavities. *ACS Nano* **2016**, *10*, 6291–6298.

[232] Roelli, P.; Galland, C.; Piro, N.; Kippenberg, T. J. Molecular cavity optomechanics as a theory of plasmon-enhanced Raman scattering. *Nat. Nanotechnol.* **2016**, *11*, 164–169.

[233] Kamandar Dezfouli, M.; Hughes, S. Quantum Optics Model of Surface-Enhanced Raman Spectroscopy for Arbitrarily Shaped Plasmonic Resonators. *ACS Photonics* **2017**, *4*, 1245–1256.

[234] Neuman, T.; Esteban, R.; Casanova, D.; García-Vidal, F. J.; Aizpurua, J. Coupling of Molecular Emitters and Plasmonic Cavities beyond the Point-Dipole Approximation. *Nano Lett.* **2018**, *18*, 2358–2364.

[235] Finazzi, M.; Ciccacci, F. Plasmon-photon interaction in metal nanoparticles: Second-quantization perturbative approach. *Phys. Rev. B* **2012**, *86*, 035428.

[236] Davis, T. J.; Gómez, D. E. Colloquium: An algebraic model of localized surface plasmons and their interactions. *Rev. Mod. Phys.* **2017**, *89*, 011003.

[237] Wolff, C.; Busch, K.; Mortensen, N. A. Modal expansions in periodic photonic systems with material loss and dispersion. *Phys. Rev. B* **2018**, *97*, 104203.

[238] Franke, S.; Hughes, S.; Dezfouli, M. K.; Kristensen, P. T.; Busch, K.; Knorr, A.; Richter, M. Quantization of Quasinormal Modes for Open Cavities and Plasmonic Cavity Quantum Electrodynamics. *Phys. Rev. Lett.* **2019**, *122*, 213901.

[239] Mueller, N. S.; Reich, S. Modeling Surface-Enhanced Spectroscopy With Perturbation Theory. *Front. Chem.* **2019**, *7*, 470.

[240] Heeg, S.; Oikonomou, A.; Garcia, R. F.; Maier, S. A.; Vijayaraghavan, A.; Reich, S. Strained graphene as a local probe for plasmon-enhanced Raman scattering by gold nanostructures. *Phys. Status Solidi RRL* **2013**, *7*, 1067–1070.

[241] G. M. Vieira, B.; Mueller, N. S.; Barros, E. B.; Reich, S. Plasmonic Properties of Close-Packed Metallic Nanoparticle Mono- and Bilayers. *J. Phys. Chem. C* **2019**, *123*, 17951–17960.

[242] Cançado, L. G.; Beams, R.; Jorio, A.; Novotny, L. Theory of Spatial Coherence in Near-Field Raman Scattering. *Phys. Rev. X* **2014**, *4*, 031054.

[243] Schedin, F.; Lidorikis, E.; Lombardo, A.; Kravets, V. G.; Geim, A. K.; Grigorenko, A. N.; Novoselov, K. S.; Ferrari, A. C. Surface-Enhanced Raman Spectroscopy of Graphene. *ACS Nano* **2010**, *4*, 5617–5626.

[244] Beams, R.; Cançado, L. G.; Oh, S.-H.; Jorio, A.; Novotny, L. Spatial Coherence in Near-Field Raman Scattering. *Phys. Rev. Lett.* **2014**, *113*, 186101.